THESIS FOR THE DEGREE OF DOCTOR OF PHILOSOPHY IN THERMO AND FLUID DYNAMICS

Pressure Coupled Representative Interactive Linear Eddy Modeling for Internal Combustion Engine simulations

NIDAL DOUBIANI

Department of Mechanics and Maritime Sciences
Division of Transport, Energy and Environment
CHALMERS UNIVERSITY OF TECHNOLOGY

Gothenburg, Sweden 2025

Pressure Coupled Representative Interactive Linear Eddy Modeling for Internal Combustion Engine simulations
NIDAL DOUBIANI
ISBN 978-91-8103-163-8

Doktorsavhandlingar vid Chalmers tekniska högskola
Ny serie nr. 5621
ISSN 0346-718X

Department of Mechanics and Maritime Sciences
Division of Transport, Energy and Environment
Chalmers University of Technology
SE-412 96 Gothenburg
Sweden
Telephone: +46 (0)31-772 1419

Cover:
Illustration of temperature profile for part- and full-load combustion for heavy-duty Volvo engine

Chalmers Reproservice
Gothenburg, Sweden 2025

Abstract

The ongoing battle over the environmental ramifications of internal combustion engines is continuously intensifying. As the automotive industry gradually shifts towards adopting light- and medium-duty electric vehicles, the transition for heavy-duty transport solutions such as trucks and ships remains challenging. This is due to the inherent limitations of battery technology in these specific applications, such as low energy density, low range, insufficient power requirement, and inadequate charging infrastructure. This implies preserving Internal Combustion Engines (ICE) as a valid technology for high-power applications. However, the environmental impact of operating ICEs by burning fossil fuels, such as diesel, is significant. Therefore, enhancing the combustion process within the ICE is essential. The reduction of pollutants emitted by the combustion engine is realized via operating the engine in nonstandard conditions such as Homogeneous Charge Compression Ignition (HCCI) or Premixed Charge Compression Ignition (PCCI), which require in-depth Computational Fluid Dynamics (CFD) simulations investigations. These simulations require specialized combustion modeling techniques capable of accurately representing finite-rate chemistry and mixed-mode combustion.

The Linear Eddy Model (LEM) was utilized in this work to predict the turbulent combustion process. LEM is distinctive in its ability to simulate turbulent combustion on a 1D line in physical space, thereby capturing all scales down to the Kolmogorov length. The LEM advanced three processes: i) Turbulence in 1D physical space via stochastic rearrangement, i.e., Triplet maps. ii) Molecular diffusion and heat conduction via advancing 1D zero-Mach number equations of species mass fractions and energy in physical space. iii) Chemical advancement in each LEM cell. This approach allows for a detailed simulation of unsteady turbulent combustion processes occurring in ICEs on the LEM.

This research led to the development of a novel stand-alone LEM model for engine combustion simulations called Spherical Stand Alone LEM (SSALEM). It is based on coupling the spherical formulation of LEM to precalculated CFD quantities using a pressure constraint. The pressure coupling enabled the direct capturing of heat effects such as the latent heat of evaporation and wall heat losses on the LEM with no modeling, as these effects are an intrinsic part of the enforced CFD pressure trace. SSALEM simulated an engine with a pressure coupling constraint based on a simple slider-crank model, where initial investigations were realized. Later, LEM was coupled to a CFD simulation using the same pressure constraint in the Representative Interactive LEM (RILEM) configuration. However, it was observed that advancing one line was not sufficient to adequately resolve the turbulent scalar statistics. For that, several LEM lines were advanced in parallel with different turbulence rearrangements coupled to one CFD solver, i.e., Multiple RILEM. MRILEM was utilized to simulate the combustion process for a heavy-duty truck engine for part- and full-load scenarios. In this investigation, the progress variable was defined based on O_2, and a novel PDF for the progress variable, namely a piece-wise step function, was utilized. MRILEM demonstrated a strong agreement with experimental data for the pressure trace and heat release both for part- and full-load cases. Afterward, a duct fuel injection was simulated with MRILEM, where the duct was implemented physically on the line(s). In this study, two different turbulence regions were implemented on the

line, to simulate the high mixing rate inside the duct. MRILEM showcased a good correlation with experimental findings and results of other models when comparing results of heat release, lift-off lengths, and ignition delay. In addition, soot was also quantified on the CFD based on mapped LEM mass fractions. Finally, MRILEM simulated another heavy-duty engine case with a low compression ratio, where MRILEM was initialized with the solution of unsteady homogeneous reactors. This investigation analyzed the effect of varying key parameters for the combustion progress: Progress variable definition (O_2 and formation enthalpy h_{298}) and progress variable PDF (Step function and presumed β). This study displays and analyses the configurations that yielded the best matches with experiments. In addition, this work also introduced a tabulated RILEM method and analyzed the effect of advancing a TRILEM compared to conventional MRILEM on the combustion process and the simulation time.

Keywords: Turbulent-Chemistry Interaction, Pressure Coupling, Pollutant Formation, Linear Eddy Model

List of publications

This thesis is based on the work contained in the following publications:

Paper I Doubiani. N., Menon. A., Kerstein. A., Oevermann. M. "Pressure Coupling Of the Spherical Linear Eddy Model to RANS-CFD for Internal-Combustion Engine Simulation" Presented in *MHMT'21: World Congress on Momentum, Heat and Mass Transfer, Lisbon, PT*. DOI: 10.4271/2019-01-1180.

Paper II Doubiani. N., Kerstein. A. R., Oevermann. M. "A pressure-coupled Representative Interactive Linear Eddy Model (RILEM) for engine simulations". Published in *Fuel*, vol. 355, pp. 129423, 2024. Elsevier. DOI: 10.1016/j.fuel.2023.129423.

Paper III Doubiani, N., Oevermann, M., Lucchini, T., Zhou, Q. "Numerical investigation of ducted fuel injection using Multiple Representative Interactive Linear Eddy Model." Published in *International Journal of Engine Research*, 2024. SAGE Publications Sage UK: London, England. DOI: 10.1177/14680874241298046.

Paper IV Doubiani, N., Oevermann, M. "Multiple Representative Interactive Linear Eddy Model: Evaluation of Progress Variable Definitions and Probability Density Functions." Published in *Fuel*, vol. 381, pp. 133445, 2025. Elsevier. DOI: 10.1016/j.fuel.2024.133445.

Acknowledgements

The Ph.D. research conducted in this thesis was carried out in the Energy Conversion and Propulsion Systems (ECaPS) division at Chalmers University of Technology. This work gave me an invaluable opportunity to dive into the complexities of turbulent combustion processes within internal combustion engines, utilizing advanced multiphysics Computational Fluid Dynamics (CFD) tools alongside various programming languages. This experience has been immensely enriching, allowing me to evolve not only as a researcher, but also as an engineer and a programmer. It has been a journey of substantial professional and personal growth, for which I am profoundly grateful.

This thesis owes its realization to the invaluable guidance and support of my supervisor, Prof. Michael Oevermann. Working alongside him has been an honor, and I greatly respect and admire his expertise and dedication. I am deeply grateful to Michael for his trust in me and for granting me the opportunity to embark on this project. His keen interest in my work, enduring patience, and consistent supervision have been instrumental in completing this academic endeavor.

I extend my sincere appreciation to Prof. Andrei Lipatnikov and Prof. Henrik Ström. Their expertise and knowledge were invaluable in guiding me through the technical complexities of my research. Their readiness to provide assistance whenever I encountered challenges contributed to the success of this work. For that, I am grateful.

My sincere thanks are also extended to Alan R. Kerstien for his invaluable support and expertise in LEM (Linear Eddy Model). His profound knowledge and insights have been instrumental in successfully completing this project. His guidance and contributions have significantly enhanced my understanding of complex turbulent combustion concepts, greatly aiding my research completion.

I want to express my profound gratitude to a critical figure in this project, my office mate, Abhilash Menon. The depth of our scientific discussions played a crucial role in leading to the several breakthroughs that shaped this project. Additionally, I am immensely thankful for his continuous support during moments of frustration, consistently offering help and encouragement.

I am grateful to Prof. Ingemar Denbrantt and Prof. Bengt Johansson for welcoming me as a Ph.D. student at the Chalmers Combustion Engine Research Center (CERC). Similarly, my gratitude extends to Prof. Lucien Koopmans and Prof. Jonas Sjöblom for the opportunity they provided me within the ECaPS division.

Lastly, I express my sincere thanks to all my colleagues in the division. Their camaraderie and shared passion for research have made the division into an inspiring academic and professional growth environment. Working alongside such dedicated individuals has been both a privilege and a pleasure.

To my beloved family.

Thank you for believing in me and being my source of strength.

Contents

List of Acronyms

BEV	- Battery Electric Vehicle
CAD	- Crank Angle Degree
CERC	- Chalmers Engine Research Center
CFD	- Computational Fluid Dynamics
CMC	- Conditional Moment Closure
DC	- Direct Current
DFI	- Ducted Fuel Injection
DNS	- Direct Numerical Simulation
DDB	- Droplet Deformation Breakup model
EATS	- Exhaust After Treatment System
EBU	- Eddy Break-Up
ECaPS	- Energy Conversion and Propulsion Systems
EDC	- Eddy Dissipation Concept
FC	- Fuel Cell
FRC	- Finite Rate Chemistry
HCCI	- Homogeneous Charge Compression Ignition
HC	- Hydrocarbons
ICE	- Internal Combustion Engine
IFC	- Infinitely Fast Chemistry
IEM	- Interaction by Exchange with the Mean
KH	- Kelvin-Helmholtz
LEM	- Linear Eddy Model
LES	- Large Eddy Simulation
LMSE	- Linear Mean Square Estimation
MRILEM	- Multiple Representative Interactive Linear Eddy Model
MZWM	- Multi-Zone Well Mixed Model
ODT	- One Dimensional Turbulence
OpenFOAM	- Open Field Operation and Manipulation
PaSR	- Partially Stirred Reactor
PDF	- Probability Density Function
PCCI	- Partially Premixed Compression Ignition
PM	- Particulate Matter
RANS	- Reynolds-Averaged Navier-Stokes
RIF	- Representative Interactive Flamelet
RILEM	- Representative Interactive Linear Eddy Model
RT	- Rayleigh-Taylor
SG-LEM	- Super Grid Linear Eddy Model
SSALEM	- Spherical Stand Alone Linear Eddy Model
SUNDIALS	- SUite of Nonlinear and DIfferential/ALgebraic equation Solvers
TCI	- Turbulence Chemistry Interaction
TPDF	- Transported Probability Density Function
TRILEM	- Tabulated Representative Interactive Linear Eddy Model

URANS	- Unsteady Reynolds-Averaged Navier-Stokes
WSR	- Well Stirred Reactor
mRIF	- Multiple Representative Interactive Flamelets

List of Roman Symbols

$\mathcal{A}$	- autocorrelation function [-]
c	- Combustion progress variable [-]
$\dot{c}$	- Rate of change of combustion progress variable [s^{-1}]
c_{ps}	- Mass specific heat capacity at constant pressure of species s [J/(kg K)]
C	- one-time autocovariance [m^2/s^2]
Da	- Damköhler number [-]
D_s	- Diffusion coefficient of species s [m^2/s]
Δh_s^0	- Standard heat of formation of species s [J/kg]
h	- Specific enthalpy [J/kg]
$\dot{h}_{ev}$	- Enthalpy due to added evaporated fuel [J/kg]
j_s	- Diffusive flux of species s [kg/(m^2s)]
k	- Turbulent kinetic energy [m^2/s^2]
Ka	- Karlovitz number [-]
l_c	- Engine cylinder length scale [m]
Le_s	- Lewis number of species s [-]
l_t	- Integral length scale [m]
p	- Pressure [Pa]
q	- Heat flux [J/m^2]
Q	- Volume ratio [-]
$\mathcal{R}[s]$	- Net production rate of specie s[mol/(m^3s)]
Re	- Reynolds number [-]
R_s	- Individual gas constant of species s [J/(kg K)]
r_{fuel}	- LEM fuel penetration length [m]
Sc_t	- Schmidt number [-]
T	- Temperature [K]
D_t	- Turbulence diffusivity [m^2/s^2]
u	- Velocity Scalar dissipation rate[m/s]
V	- Volume [m^3]
V_{fuel}	- Volume with fuel evaporation [m^3]
v_N	- Spray's velocity [m/s]
We	- Weber number [-]
W_s	- Molecular weight of species s [kg/mol]
$\dot{w}_s$	- Source term of species s [s^{-1}]
Y_s	- Mass fraction of species s [-]
$\dot{Y}_{sev}$	- Source term due to fuel evaporation for species s [s^{-1}]
Z	- Mixture fraction [-]

List of Greek Symbols

α	- Cone angle of LEM line [radians]
α, β	- Coefficients in the β-PDF for mixture fraction [-]
β	- LEM vapor penetration ratio [-]
C_χ	- Model constant for scalar dissipation rate typically 2.0 [-]
C_μ, C_ψ	- Model constants [-]
Δ	- LES filter width or differential operator [m]
Δt, δt	- Time step and half time step in LEM simulations [s]
ε	- Rate of dissipation of turbulent kinetic energy [m^2/s^3]
$\Gamma(t)$	- Gamma function [-]
γ	- Specific heat ratio, c_p/c_v [-]
ρ	- Density [kg/m^3]
$\dot{\rho}_s$	- Source term due to evaporation [$kg/(m^3 s)$]
η	- Kolmogorov length scale [m]
λ	- Eddy event frequency per unit length [1/m]
μ_t	- Turbulent (eddy) viscosity [kg/(m s)]
ν	- Kinematic viscosity [m^2/s]
ϕ	- General turbulent reactive scalar [-]
χ	- Scalar dissipation rate [s^{-1}]
$\tilde{\varepsilon}$	- Turbulent dissipation rate [m^2/s^3]
τ_{ec}	- Time required for one engine cycle [s]

1 Introduction

1.1 Background

It is difficult to deny the current and foreseeable importance of combustion in society due to its numerous applications. Its earliest utilization dates back to approximately 5000 years, serving fundamental purposes such as cooking, heating, pottery making, and metallurgy. Today, combustion continues to play a central role in our lives with about 80% of the total energy supply deriving from the burning of solid, liquid, and gaseous fuels [1]. The evolution of combustion technology led to its integration into several applications, including electricity generation, domestic heating, waste incineration, and transportation of people and merchandise. Historically, these applications were initially realized by burning coal and wood in steam engines, a technology that led to widespread deforestation [2]. Later, the internal combustion engine, powered by fossil fuels, replaced the steam engine, by offering advantages in terms of efficiency and compactness. This made ICE a highly adaptable technology for over 140 years [3]. Despite its efficiency, two main issues have emerged from utilizing ICE: The primary issue is the production of detrimental emissions, predominantly CO_2. The second is the acceleration of the depletion rate of fossil fuel reserves, which can raise concerns regarding global energy security. These issues indicate the need for sustainable and environmentally friendly alternatives, especially if we aim to continue relying on combustion as a feasible technology in the future.

Carbon dioxide CO_2, which is a byproduct of both complete and incomplete combustion, is not directly dangerous to human health. In fact, its presence is vital for maintaining appropriate temperature levels for an optimized functioning of the planet [4]. However, CO_2 concentrations have increased substantially due to fossil fuel combustion, which undeniably contributes to greenhouse effects. This phenomenon traps the heat in the atmosphere, leading to several environmental changes, such as an increase in the global average temperature and rising sea level due to the melting of the arctic ice. In the case of incomplete combustion, which is commonly the case in a real-life combustion application, several undesirable emissions emerge from fossil fuel combustion. These include, e. g., NOx, which contributes to the acidification of ecosystems [5], CO, causing a threat to human health by leading to potential lethal poisoning [6], HC linked to different forms of cancer [7], and PM, causing cardiovascular and respiratory problems [8]. The root of these environmental and health issues is not the internal combustion engine itself but rather the combustion of fossil fuels. Therefore, one of the measures decided upon according to the 2050 Net Zero objective [9] is to prohibit fossil fuel combustion .

Figure 1.1 displays that the transportation sector significantly contributes to global CO_2 emissions. To mitigate this, the upcoming Euro VII emission standards, scheduled for implementation in July 2025, aim to impose strict legislation to this sector by imposing a reduction on NOx emissions by 35% compared to current standards and lowering tailpipe emissions by 13% for light-commercial vehicles. In response to these scheduled regulations, several OEMs have decided to transition to producing exclusively BEVs and FC vehicles.

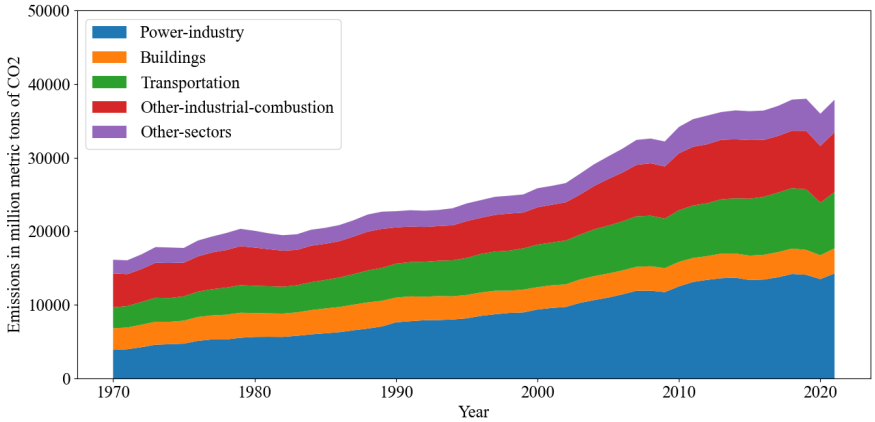

Figure 1.1: *Global carbon dioxide emissions from 1970 to 2021, by sector (in million metric tons of carbon dioxide) [10]*

This shift is motivated by two main reasons. Firstly, by 2035, the prohibition on selling cars equipped with ICEs that cause direct emissions will be applied, except for those operating on renewable fuels [11]. Secondly, because of the complexity and cost of the EATS's that comply with the presented legislation.

Although BEVs and FC are promising technologies that can be used to solve the emissions crisis, this decision can be criticized on the basis that the zero-emission claim is accurate and only valid if the entire life cycle of the fuel is considered, i.e., from well to wheel and not only tank to the wheel. This means that electricity and hydrogen production should not have emitted emissions, which is rarely the case. Furthermore, several vehicles dedicated to mining, construction, or agriculture applications require significant power that the BEVs can only deliver by utilizing large batteries. E.g., A battery of an electrically powered heavy-duty truck weighs about five tons, which is almost five times the weight of a conventional heavy-duty truck ICE. This observation is even more extreme if applied to large marine vessels or commercial aero-transport. The recharging time also presents an issue, where the average recharging time for a BEV is about an hour. On the other hand, the tanking time usually takes a few minutes for the ICE or FC. Some charging stations include level 3 charging, i.e., DC fast charging, which can charge a passenger car to 80% in 15-20min. However, these charging stations have yet to become popular (around 20%). This issue worsens when users cannot afford long charging times, e.g., concrete delivery to construction sites. Furthermore, frequent battery recharging causes long-term problems for the battery capacity since it decreases the range of the vehicle and its performance. Overcoming this requires a battery replacement, which is expensive and unsuitable for the environment. FC vehicles likewise face several challenges, where their production requires rare and expensive metals such as platinum, which is used in the FC catalyst. These rare metals can be even more expensive than

the ones required by BEVs. In addition, the H_2 charging infrastructure still needs to be developed. This issue hinders the development of FC vehicles since it demands significant investments and research to decrease the potential hazards [12]. FC also requires large pressure tanks to store H_2, reducing the fuel's energy density and the available cargo.

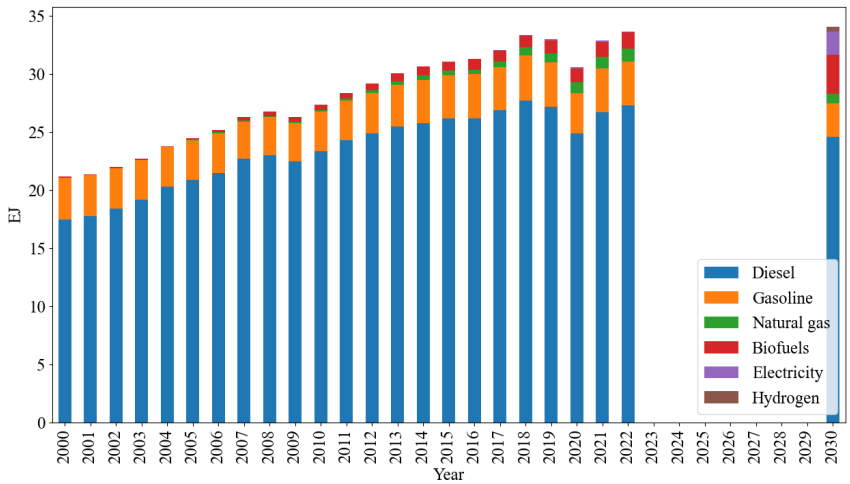

Figure 1.2: *Global final energy demand for trucks and buses by fuel in the Net Zero Scenario, 2000-2030 [13]*

Figure 1.2 indicates that Diesel fuel remains the predominant energy source for trucks and buses even projecting forward to 2030. This trend is largely due to sectors such as mining, construction, and agriculture, which rely heavily on high-power output traditionally delivered by the ICE. Therefore, the idea of completely substituting the ICE technology seems unrealistic for the short term. A more feasible solution would be to diversify energy conversion technologies used in these sectors. This strategy would involve continuing the use of ICE for applications requiring extensive energy demand while minimizing its impact by optimizing and running it with alternative fuels such as Biofuels and Electro fuels. Simultaneously, it is important to support the maturation of other technologies such as BEVs and FC. This shift, where ICE is optimized and used alongside growing sustainable technologies is essential for a realistic transition towards environmentally friendly energy sources that can meet the global demand.

Given the continuous worldwide reliance on ICE in the coming years and likely decades, the optimization of this technology to minimize its impact on the environment is crucial. ICE optimization can be realized with experimental investigations. This type of analysis can be significantly expensive and can only produce limited information about the combustion process and the turbulent flow due to accessibility difficulties, e.g., inside fuel injection nozzles. However, the data generated from experimental investigations is essential since it

is regarded as the "truth" of what is occurring in the ICE. On the other side, improving ICEs is also realized by performing detailed numerical simulations. These numerical tools are more affordable than experiments and can be realized for small lengths and time scales. However, the simulation time with the current hardware can be absurdly long if the full scale of turbulent reacting flows is desired to be resolved for complex geometries. For that, several assumptions are utilized to reduce the computational time. Moreover, model validation is a crucial step; it is accomplished by comparing the numerical data to experimental data or results of Direct Numerical Simulations (DNS). Numerical models offer the possibility of non-intrusive detailed investigations of the different processes in regions where experimental measuring techniques cannot be performed. In addition, geometrical modifications can be performed fast and practically with no additional cost compared to experiments. Therefore, experimental and numerical tools are complementary tools necessary for ICE optimization.

Numerical modeling of turbulent reacting flows is complex since it is a multi-scale problem. It involves turbulence modeling, fluid mechanics, stochastic modeling, thermodynamics, chemical kinetics, heat and mass transfer, and several numerical techniques. Coupling these fields together while maintaining the model's validity and fidelity is another challenge. Turbulence and combustion must be modeled such that their interaction is preserved. The interaction between combustion and turbulence is a two-way process; on one hand, turbulence impacts combustion by changing chemical species' consumption and production rates, leading to, e.g., flame ignition or extinction, incomplete combustion, and pollutants formation. On the other hand, combustion influences the flow by accelerating the flame front, e.g., Flame-generated turbulence, or it can lead to laminarization of the flow due to changes in the viscosity. Several models were developed depending on the combustion mode, regime, and speed of chemistry. The following table by Peters [14] summarizes some common combustion models. This table was first presented in 2001, it is therefore presented in an updated format according to the current state of combustion models.

The work realized in this thesis was accomplished by utilizing the Linear Eddy Model for combustion closure. LEM is capable of simulating non-premixed, premixed, and partially premixed combustion modes. In addition, simulating the combustion process in internal combustion engines requires a detailed description of pollutant formation. This requires a combustion model that advances finite-rate chemistry with detailed chemical mechanisms. LEM was introduced by Kerstein initially as a scalar mixing model for non-reactive flows [24, 32, 33] and was extended to simulate reactive mixtures [25, 34–36]. Building on this foundation, LEM was employed to assess molecular diffusion effects by varying Reynolds and Schmidt numbers [37]. LEM was also employed to examine the impact of varying the turbulent length scale distribution on developing a single-point PDF for homogeneous, isentropic stationary turbulence [38]. LEM displayed reasonable results when compared to DNS when putting less emphasis on small turbulent structures. LEM was also utilized to predict the PDFs of reactive scalars for non-premixed methane and hydrogen jet flames [39], where it was compared to experimental results and yielded good agreement. In meteorological studies, LEM was applied for mixing dry and moist air to predict temperature changes because of droplet evaporation and condensation [40, 41]. Concerning

	Premixed Combustion	Non-premixed Combustion
IFC	Bray-Moss-Libby [15] Coherent Flame Model [16] Eddy Break up Model [17, 18]	Conserved Scalar Equilibrium Model [19] Eddy Dissipation Model [20]
FRC	Perfectly / Partially Stirred Reactor [21, 22]	
	Transported PDF Model [23]	
	Linear Eddy Model [24, 25]	
	Tabulated Flamelet Progress Variable Model (Z,c) [26]	
	Flamelet Generated Manifold [27]	
	Flamelet-G Equation Model [28]	Representative Interactive Flamelet [29, 30] Conditional Moment Closure Model [31]

Table 1.1: Classification of turbulent combustion models by combustion mode and chemistry speed [14].

specific reactive scenarios, LEM was utilized to simulate the auto-ignition process of H_2 under thermal stratification for HCCI combustion [42]. In this study, LEM simulated H_2 combustion by including differential diffusion effects via varied Lewis numbers for each species. LEM results were compared qualitatively and quantitatively against 2D DNS simulations, where it successfully predicted heat release rates and evaluated the importance of reaction and diffusion terms.

In a more advanced application, LEM was utilized as a subgrid model for simulating H_2 diffusion combustion in LES context [43]. LEM was initially utilized to provide only mixing information, where it successfully managed to qualitatively predict PDFs of mixture fraction field on the CFD compared to experimental work performed in [44]. Later, NO and OH concentrations were predicted by advancing a reactive LEM in each LES cell with a chemical mechanism of 9 species. Convection between different LEMs was realized via a splicing algorithm, which takes a set of LEM cells from the end of the line and attaches them to the beginning of another depending on the estimated fluxes. The splicing methodology was extended to unstructured grids in [45], where it was shown that the prediction of passive scalars and velocity fields is correctly achieved using the new splicing algorithm. The new splicing technique was tested for a non-premixed syngas flame and a stabilized premixed bluff body flame [46]. The mapping strategy was also modified from directly acquiring species from the LEM lines in each LES cell to a reaction rate mapping with advancing transport equations of species and enthalpy on the CFD side. Although LES-LEM successfully simulates non-premixed and premixed flames, it

remains a computationally expensive model. A recent SG-LEM model was developed in [47] based on direct mapping of species mass fractions to reduce the computational cost. It features the utilization of single LEM lines to advance diffusion, turbulence, and chemistry inside each cluster of LES cells called "super-grid". SG-LEM was applied for a premixed case in [48], where it showed promising results when assessed against DNS results by comparing temperature fields, primary and radical species, and species reaction rates. The computational time was also dramatically reduced (40 hours for SG-LEM and 969 hours for LES-LEM).

Shifting to a RANS context, LEM was utilized in a coupled format to provide subgrid combustion closure, where one LEM line was utilized to represent the entire CFD domain. In [49], it was coupled to the URANS code KIVA 3D to simulate an engine in HCCI conditions. Different fuel and temperature profiles were prescribed on the LEM line. This study utilized a 2-step, 6-species chemical mechanism for n-heptane with one LEM, and it concluded that adding LEM to the CFD simulation to represent mixing, diffusion, and combustion improved the combustion prediction when comparing the pressure traces with a multi-zone KIVA-3D code [50]. LEM was extended to LEM3D in [51]. It was first utilized as a post-processing tool for RANS N_2-diluted H_2 jet flame in a co-flow of hot products from lean H_2-air reaction [52]. Using LEM3D, flame structure, species distribution, and flame lift-off length were evaluated. Later, LEM3D was extended to be coupled to a RANS simulation [53]. The investigated case and the extracted results were similar to what was realized in [52], only this time LEM3D provided feedback to the RANS simulation. The RILEM work was initiated in a previous project [54]. It is based on a RANS approach coupled with the LEM that provides combustion closure, essentially a RANS-1D DNS model. The idea behind RILEM is to decrease the computational time of LES-LEM further without sacrificing the ability to simulate finite-rate chemistry and mixed-mode combustion. RILEM does not utilize reaction rate closure; instead, it employs a similar approach as RIF, which utilizes advancing passive and reactive scalars to extract a presumed PDF for each computational cell. The model was applied to internal combustion engine simulations focusing on the combustion process and its interaction with resolved turbulence. It was first developed for a constant volume case [55] and then compared against RIF in [56]. Later, RILEM was applied for the Sandia spray B combustion engine case in [57, 58] based on a mixture fraction formulation and a volume constraint for the CFD-LEM coupling. It was after that extended to include a progress variable approach for a heavy-duty case in [59].

1.2 Research questions and objectives

This work involves continuity of the RILEM model development by targeting the following research questions:

- **How could we implement a pressure coupling constraint between LEM and CFD? What are the modifications that should be introduced to the LEM line?** The RILEM model was initially formulated based on a volume coupling constraint, where the LEM matched the volume of the CFD domain, and the heat

effects were directly modeled on the LEM line. Replacing the coupling constraint with pressure grants the possibility of avoiding the supplementary modeling of heat effects on the LEM line since they are contained in the averaged pressure from the CFD. This adaptation requires a geometrical manipulation of the LEM line chosen in its spherical geometry specifically for this task.

- **How can we improve the statistical fidelity of RILEM? How can we avoid missing data points in the LEM solution originating from chemistry advancement and scalar conditioning tradeoff**? What are the effects of advancing multiple LEM lines with different turbulence statistics instead of utilizing a unique line? The previous version of RILEM was based on advancing a single LEM line. Fast chemistry advancement prevents the solver from conditioning scalars on the entire space of the progress variable, which causes empty slots in the solution table. Multiple LEM lines with different eddy statistics are advanced in parallel to complete the solution. A novel PDF is presented, defined on the integrity of the progress variable space and based on the Favre-mean of the progress variable only combined with a PDF scaling technique.

- **Can RILEM be extended to cases with vastly different turbulence levels in the domain, e.g. Ducted Fuel Injection, and how? How robust is the RILEM model in capturing unsteady combustion effects, such as ignition delay and lift-off length?** Previous RILEM simulations that are based on two independent variables were realized only for standard engine applications with homogeneous isotropic turbulence, which implies a uniform distribution of the turbulent eddies on the LEM line. A DFI involves different turbulence regions in the CFD domain, i.e., different turbulence in the CFD domain.

- **What would be a good definition and PDF for the combustion progress variable c for the applications here? How does changing the definition of the combustion progress variable, i.e., O_2 vs. h_{298} impact the solution? How would a β-PDF based on an algebraic model for the combustion progress variable variance perform for a RILEM simulation compared to a step function? How would a tabulated RILEM perform against MRILEM?** As mentioned in the second research question, RILEM utilized multiple LEM lines to improve statistical fidelity. However, it is possible to further improve the initialized solution table by advancing homogeneous reactors for each mixture fraction bin and constructing a solution in the mixture fraction and combustion progress variable space. Moreover, two definitions and PDFs of the combustion progress variable were investigated, i.e. O_2 and h_{298}, and step and β-PDF, respectively. In addition to this, a tabulated version of RILEM is introduced and its results are compared to Multiple RILEM.

1.3 Thesis outline

This thesis is structured in the following chapters:

- **Current chapter**: Describes a general background for the work with its objectives and research questions.
- **Chapter 2**: Presents a brief overview of turbulent combustion modeling.
- **Chapter 3**: Presents the RILEM combustion model.
- **Chapter 4**: Displays a summary of the main findings.
- **Chapter 5**: Finishes with a conclusion and an outlook on future work.

2 Turbulent Combustion

Combustion occurs in various technical applications, manifesting itself in different modes and regimes. In industrial contexts such as ICE, gas turbines or rocket engines, combustion typically operates in a turbulent regime. This implies a co-existence of turbulence and combustion and that their interactions influence the flame propagation and pollutant formation. Consequently, accurate numerical modeling is essential. However, it represents a challenging task as it would explained in later sections.

2.1 Combustion

Combustion refers to an oxidation process through which chemical bond energy is transformed into thermal energy via exothermic chemical reactions. This process typically involves a reaction between a fuel and an oxidizer, often oxygen O_2. While the direct form of energy released from combustion is thermal, it can be harnessed and converted to other forms of energy, such as mechanical work and electricity. A one-step simplified chemical reaction for combustion can be written in the following form:

$$\mathrm{F} + \nu_{\mathrm{O_2}}\mathrm{O_2} \rightarrow \nu_{\mathrm{CO_2}}\mathrm{CO_2} + \nu_{\mathrm{H_2O}}\mathrm{H_2O}, \tag{2.1}$$

where F denotes the reacting fuel and ν_s the stochiometric coefficient of each of the species $s \in \{\mathrm{O_2}, \mathrm{H_2O}, \mathrm{CO_2}\}$. This chemical reaction equation, however, does not take place in reality. Instead, several intermediate chemical reactions occur, leading to a net reduction of reactants and the formation of products. To accurately represent the combustion process, utilizing a complex mechanism involving several intermediate species is essential. The formation and consumption of species depend on their chemical time scales, which makes tracking intermediate species with short time scales challenging. The set of chemical equations governing the combustion process with $r = 1, \ldots, n_r$ can be written in the following form:

$$\sum_{s=1}^{n_s} \nu'_{s,r}\mathrm{A}_s \rightleftharpoons \sum_{s=1}^{n_s} \nu''_{s,r}\mathrm{A}_s \tag{2.2}$$

where $\nu'_{s,r}$ and $\nu''_{s,r}$ denote the forward and reversible stoichiometric coefficients of species A_s in reaction r, respectively. The terms $\mathcal{R}'_r$ and $\mathcal{R}''_r$ represent the speed at which chemical reactions r occur. They are determined using the following formula:

$$\mathcal{R}'_r = k'_r \prod_{s=1}^{n_s} [\mathrm{A}_s]^{\nu'_{s,r}} \quad , \quad \mathcal{R}''_r = -k''_r \prod_{s=1}^{n_s} [\mathrm{A}_s]^{\nu''_{s,r}}, \tag{2.3}$$

where k'_r and $-k''_r$ represent the rate coefficient of the forward and backward reaction r, respectively. An approximation to their value can be calculated using Arrhenius's law:

$$k'_r = A' \exp\left(-\frac{E'_r}{RT}\right) \tag{2.4}$$

where A' is the pre-exponential coefficient, E'_r is the activation energy for reactant r and R is the universal gas constant. $[\mathrm{A}_s]$ describes the concentration of species A_s, which is calculated as the following:

$$[\mathrm{A}_s] = \rho \frac{Y_s}{W_s}, \tag{2.5}$$

where ρ is density, Y_s the mass fraction of species A_s, and W_s the molecular weight of species A_s.

The chemical source term $\dot{\omega}_s$ for species s, which accounts for the net formation (or consumption) rate of species s considering all n_r reactions it participated in can be written as the following:

$$\dot{\omega}_s = W_s \sum_{r=1}^{n} (\nu''_{s,r} - \nu'_{s,r})(\mathcal{R}' - \mathcal{R}''). \tag{2.6}$$

The $\dot{\omega}_s$ term is also the source term apparent in the species transport equation (2.31), as will be described later in this thesis.

Three main modes dominate combustion application in ICE:

- Non-premixed combustion - Diffusion combustion: The fuel and the oxidizer are injected separately into the domain. Turbulence and molecular diffusion mix the fuel and the oxidizer to the molecular level, creating combustible mixtures under proper conditions. In the case of compression ignition engines, which primarily operate under non-premixed combustion, these mixtures are auto-ignitable. This mode is called diffusion combustion because diffusion is the rate-controlling process.
- Premixed combustion: The fuel and the oxidizer are mixed to a certain level that can be quantified with the equivalence ratio ϕ. Premixed combustion leads to better combustion, emitting fewer undesirable emissions. However, it is considered dangerous since the flame is difficult to control compared to non-premixed combustion. Premixed combustion is typically used in Spark Ignition Engines.
- Partially premixed - Mixed mode combustion: In this mode, either the fuel or the oxidizer is injected into a mixture already in a premixed state, leading to either an increase or decrease of the global equivalence ratio. This mode is commonly employed in Partially Premixed Compression Ignition Engines.

If turbulence is added to the system, different time scales of chemistry and turbulence exist, which makes the simulation an even more complex exercise.

2.2 Turbulence

Turbulence is regarded as one of the most heavily researched topics in engineering due to its critical role in almost all engineering applications involving fluid motion. It is

generated in ICE via high pressure fuel injection, which generates shear vorticies causing the fuel and the oxidizer to mix down to the molecular level. Turbulence also helps in reducing emissions. Considerable efforts have been made to develop numerical models that accurately represent turbulent motions. However, these models utilize different assumptions depending on the complexity of the task and the available resources. The Reynolds number Re introduced by Reynolds [60] represents the ratio of the inertial to viscous forces. It provides a (problem dependent) measure for the state of the flow whether it is laminar, transitional, or turbulent and is defined as

$$\mathrm{Re} = \frac{\rho U L}{\mu}, \tag{2.7}$$

where U denotes the characteristic velocity, L the characteristic length, μ the dynamic viscosity and ρ the density.
Turbulence modeling's complexity emerges from the presence of several time and length scales that require a detailed description. Although turbulence is often described as chaotic and unpredictable, it is possible to spot patterns in the turbulent motions. This was described by Richardson [61], in his concept of energy cascade, which states that the largest turbulent motions break down into small eddies, and these small eddies continue to break down further into even smaller eddies until they are dissipated into heat because of viscosity.

The turbulent length scale l_t represents the largest eddy size and is proportional to the geometry of the domain. It is calculated based on the autocorrelation function $\mathcal{A}$:

$$l_t = \int_0^\infty \mathcal{A}(r)\, dr, \tag{2.8}$$

where $\mathcal{A}(r)$ is the autocorrelation function defined as:

$$\mathcal{A}(r) = \frac{\mathcal{C}(r)}{\mathcal{C}(0)} = \frac{\langle u'(x)u'(x+r)\rangle}{\langle u'(x)^2\rangle}. \tag{2.9}$$

Here, $\mathcal{C}(r)$ is the two-point, one-time autocovariance function defined as:

$$\mathcal{C}(r) = \langle u'(x)u'(x+r)\rangle, \tag{2.10}$$

where the $\langle\cdot\rangle$ operator represents ensemble averaging and u' is the velocity fluctuation. For highly turbulent flows, it is often assumed that turbulence is isotropic and homogeneous, allowing us to neglect the dependency on the position x. This implies that the autocorrelation function $\mathcal{A}$ depends only on the distance r between two points.

The same strategy also allows the calculation of the integral time scale τ_t, which represents a characteristic time for the largest eddy to turn over. It can be calculated by utilizing the autocorrelation function of time $\mathcal{A}(\tau)$ and assuming stationary stochastic turbulence:

$$\tau_t = \int_0^\infty \mathcal{A}(\tau)\, d\tau. \tag{2.11}$$

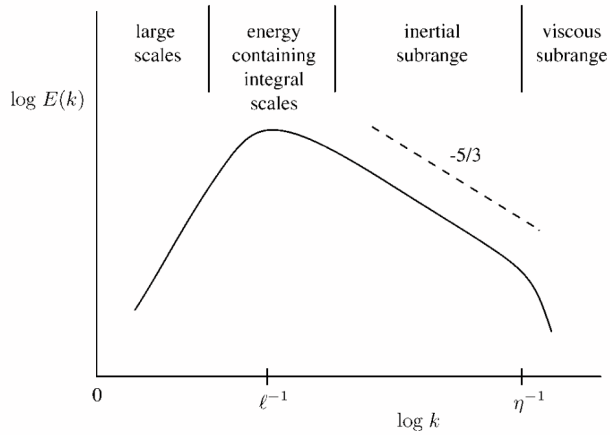

Figure 2.1: *Representation of the energy spectrum as a function of the wave number k [14]*

The rate at which the eddies break down is known as the dissipation rate ε, which is characterized by:

$$\varepsilon = \frac{\mathrm{d}k}{\mathrm{d}t}, \tag{2.12}$$

Figure 2.4 shows the energy spectrum as a function of wave number. In this figure, the inertial subrange is depicted, representing the region where the effects of viscosity could be neglected and where inertial forces contribute to the transfer of energy from larger to smaller eddies at the dissipation rate, which is known as the *inertial subrange*, limited between the integral and the dissipative ranges. These scales play a crucial role in predicting the impact of turbulence on the flow field.

The Kolmogorov length scale η represents the smallest scale of the turbulent eddies where dissipation of turbulent kinetic energy into heat due to viscous forces [62] takes place. Andrei Kolmogorov stated the following three hypotheses for turbulence:

- **Hypothesis 1**: The small turbulent scales (viscous subrange) are statistically isentropic for large Reynolds numbers.
- **Hypothesis 2**: The form of the small-scale turbulent motions (viscous subrange) is universal and uniquely governed by ε and ν. This allowed formulating Kolmogorov's length η, time, τ_η, and velocity v_η:

$$\eta = \left(\frac{\nu^3}{\varepsilon}\right)^{1/4} \quad , \quad \tau_\eta = \left(\frac{\nu}{\varepsilon}\right)^{1/2} \quad , \quad v_\eta = (\nu\varepsilon)^{1/4}. \tag{2.13}$$

- **Hypothesis 3**: For sufficiently high Reynolds number, in any flow field, the statistics of the turbulent motions in the inertial subrange have a universal form that is independent of ν and described uniquely by ε.

2.3 Turbulence-Chemistry Interaction

Combining the two processes of combustion and turbulence adds an additional layer of complexity. Turbulence directly influences combustion via, e.g., the (turbulent) distributions and mixing of reactive scalars. This causes several combustion effects such as flame-lift-off, flame-quenching, and even extinction in extreme cases. Similarly, combustion influences turbulence by either increasing or decreasing it. This is realized via changes in density and kinematic viscosity due to heat release. It is, therefore, essential to include the effects of these interactions in the physical models and numerical methods for simulating turbulent combustion. The interaction between turbulence and combustion is typically characterized by comparing turbulent and chemical scales. This comparison characterizes the different combustion regimes. The combustion regimes are different depending on the combustion mode, i.e. premixed or non-premixed.

2.3.1 Premixed combustion regimes

The dynamics of premixed combustion involve interactions between the flame front, characterized by its thickness (δ) and laminar flame speed (s_L), and turbulent eddies. These eddies are described by their velocity turnover and length scale, which vary depending on their position within the inertial subrange. Specifically, at the integral scale, these scales are represented by l_t and u', where u' is the root mean square velocity, and for the Kolmogorov scale, the scales are denoted by η_k and u_k, where u_k referring to the Kolmogorov eddy turnover velocity.

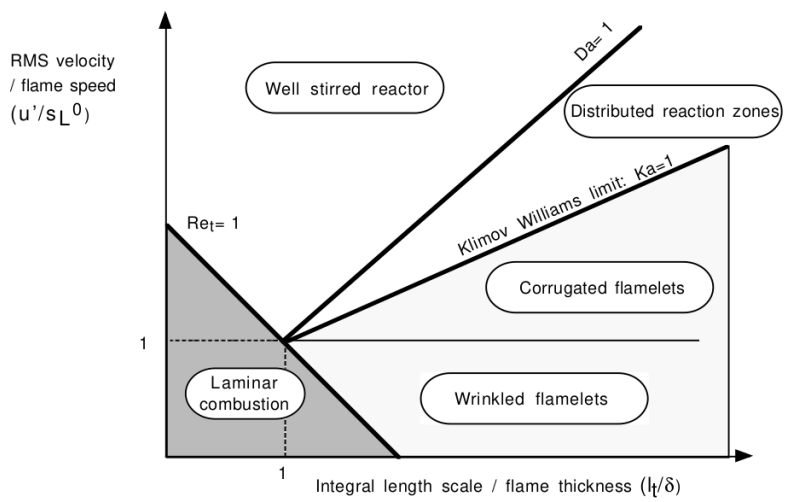

Figure 2.2: *log-log- graph representing the different regimes in turbulent premixed combustion [19]*

A general Damköhler Da(r) number represents the ratio between the turbulent time scale for an eddy of size r and a chemical time scale τ_c:

$$\mathrm{Da}(r) = \frac{\tau_m(r)}{\tau_c} \tag{2.14}$$

Depending on the specific value of r the interaction between the turbulence and chemistry process varies.

Two dimensionless numbers are introduced to describe the interactions in premixed combustion. The Damköhler number Da is used for integral scales and it represents the ratio of the integral time scale τ_t, which is the time scale for an eddy of size l_t, to the chemical time scale τ_c. The Damköhler number is defined as:

$$\mathrm{Da} = \frac{\tau_t}{\tau_c}, \tag{2.15}$$

Additionally, the Karlovitz number Ka quantifies the relationship at the Kolmogorov scale, defined as the ratio of the chemical time scale τ_c to the time scale of Kolmogorov eddies τ_η, where τ_η is the time scale for eddies of size η. The Karlovitz number is expressed as:

$$\mathrm{Ka} = \frac{\tau_c}{\tau_\eta}. \tag{2.16}$$

The Ka number can also be expressed in a way that links the time and length scales according to [19]

$$\mathrm{Ka} = \left(\frac{\delta}{\eta}\right)^2 \tag{2.17}$$

Different scenarios emerge based on the comparison of the integral, chemical, and Kolmogorov time scales.

At low Damköhler numbers Da < 1 i.e. ($\tau_t < \tau_c$), the chemical time scale exceeds the time scale associated with the largest turbulent scales, i.e. the integral length scale l_t. In this scenario, the mixing process dominates the system's behavior. This regime is referred to as the **Perfectly Stirred Reactor (PSR)** regime.

For Da > 1 & Ka > 1, i.e. ($\tau_t < \tau_c < \tau_\eta$), the chemical time scale is shorter than the integral time scale. This means that the flame's inner structure remains unaffected by the larger turbulent motions, which instead contribute to wrinkling of the flame front. However, since the Kolmogorov time scale is smaller than the chemical time scale, the small eddies do influence the flame structure, potentially causing flame stretching. If this stretching exceeds the critical level for flame stability, the flame may experience quenching. This specific condition characterizes the **Thickened Flame** regime.

Finally, for Ka < 1, i.e. ($\tau_c < \tau_\eta$) the chemical scale is faster than all the turbulent scale and the flame is thinner than the smallest turbulent eddies, i.e., eddies of size η according to (2.17). This situation is referred to as the **Flamelet** regime. Within this regime, two distinct scenarios emerge based on the comparison between the laminar flame speed s_L and the surrounding root mean square (RMS) velocity u':

- If $u' < s_L$, the RMS velocity is slower than the flame's propagation speed. In this case, the flame is mainly influenced by chemical reactions, and the flow only causes wrinkles on the flame front. This behavior characterizes the **Wrinkled Flamelets** scenario.

- When $u' > s_L$, the RMS velocity's influence on the thin flame exceeds that of the chemical reactions. The dynamics of the flow lead to bending the flame, resulting in the formation of pockets of burnt and unburnt gases. This scenario is referred to as the **Corrugated Flamelet** regime.

2.3.2 Non-Premixed combustion regimes

The description of turbulent combustion regimes on non-premixed flames is more difficult and is still an open question, as there are no intrinsic predefined time and length scales as in premixed flames. However several attempts have been made to define combustion regimes for diffusion flames [14, 63–65]. Peters [14] introduced a combustion diagram that describes the combustion regimes for diffusion flames. He proposed several scales to construct a combustion regime diagram for diffusion flames. First, he introduced a diffusion thickness l_D, which can be calculated based on the strain rate a, which has units of the inverse of time, and the stoichiometric diffusion coefficient D_{st}:

$$l_D = \sqrt{\frac{D_{st}}{a}} \tag{2.18}$$

He then introduces a flame thickness in mixture fraction space defined by the following:

$$(\Delta Z)_F = |\nabla Z|_{st}\, l_D \tag{2.19}$$

Here, $(\Delta Z)_F$ includes the convective layer, the diffusive layer, and the reaction layer in mixture fraction space.

Another important variable to characterize combustion regimes in non-premixed combustion is the fluctuation of the mixture fraction Z, particularly the fluctuations of Z_{st}. These fluctuations are characterized by the root mean square (RMS) of the mixture fraction variance $\widetilde{Z''^2}$:

$$Z'_{st} = (\widetilde{Z''^2})^{\frac{1}{2}}_{st} \tag{2.20}$$

Two additional key parameters used to describe the regimes are based on the scalar dissipation rate, namely the extinction scalar dissipation rate χ_q and the stoichiometric scalar dissipation rate $\widetilde{\chi}_{st}$.
From these four parameters, the combustion diagram is constructed:

- For $Z'_{st}/(\Delta Z)_F > 1$, which corresponds to large Z'_{st} fluctuations. Two regions are formed, one lean and one rich. In this scenario, the fluctuations are so large that even the diffusive layers of these regions do not overlap, leading to the formation of two separated flamelets.

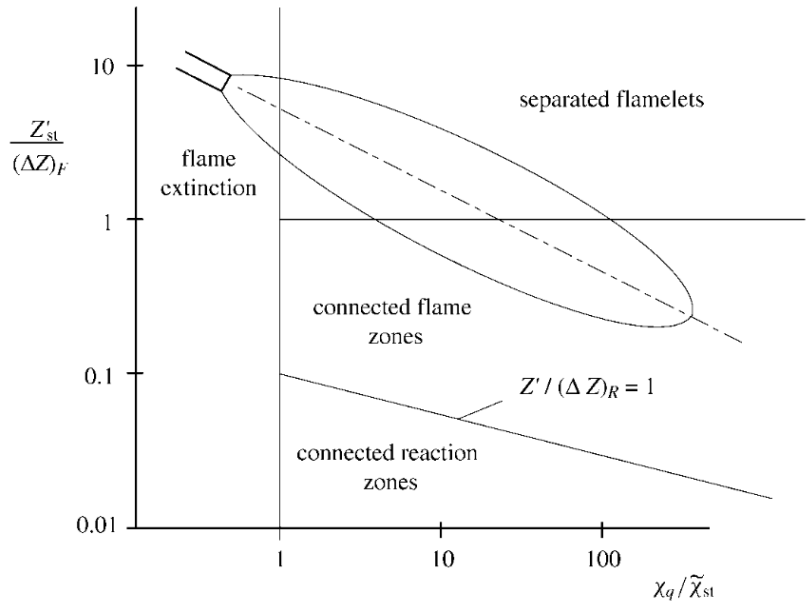

Figure 2.3: *Log-log graph representing the different regimes in turbulent non-premixed combustion [14]*

- For $Z''_{st}/(\Delta Z)_F < 1$, corresponding to small Z''_{st} fluctuations. The two layers merge into one. However, only the diffusive layers of the rich and lean regions are connected, implying that mixing down to the molecular level is still required.
- For $Z''_{st}/(\Delta Z)_F \ll 1$, this corresponds to negligible Z''_{st} fluctuations. In this situation, the reaction zones of the two regions are merged and connected, implying perfect mixing. This condition is identified by the line $\frac{Z''_{st}}{(\Delta Z)_R} = 1$.
- For $\chi_q/\widetilde{\chi}_{st} < 1$: This region corresponds to flame extinction since the extinction scalar dissipation rate is smaller than the stoichiometric one. It is in this region that unsteady effects such as flame lift-off occur.
- For $\chi_q/\widetilde{\chi}_{st} > 1$: Here, the extinction scalar dissipation rate is larger than the stoichiometric scalar dissipation rate, allowing sustained reactions to occur.

Peters also outlined the criteria for the flamelet regime, which is defined by:

$$\frac{(\Delta Z)_R}{|\nabla Z_{st}|} < \eta \tag{2.21}$$

This criterion implies that the reaction zone thickness should be smaller than the Kolmogorov eddy length, ensuring that the flame is thin enough to avoid extinction caused by small turbulent eddies.

2.4 Reacting Gas Phase Governing Equations

A reacting gas mixture is a cluster of multiple species undergoing chemical reactions that release heat through chemical equations. The gas mixture can be described by a set of primitive variables, where ns denotes the number of species in the mixture:

- Partial density ρ_k and total density ρ:

$$\rho = \frac{m}{V} \quad \rightarrow \quad \rho = \sum_{k=1}^{ns} \rho_k = \sum_{k=1}^{ns} \frac{m_k}{V}, \tag{2.22}$$

  where m_k and m denote the partial and total mass, and V the volume occupied by the mixture.

- The mixture velocity field $\mathbf{u}$ is defined as the mass-averaged velocity of the mixture:

$$\mathbf{u} = \frac{1}{\rho} \sum_{k=1}^{ns} \rho_k \mathbf{u}_k, \tag{2.23}$$

  where $\mathbf{u}_k$ is the velocity of species k.

- Species mass fractions Y_k or mole fractions X_k:

$$Y_k = \frac{m_k}{m}\,, \quad X_k = \frac{n_k}{n} \quad \rightarrow \quad \sum_{k=1}^{ns} Y_k = 1 \quad , \quad \sum_{k=1}^{ns} X_k = 1. \tag{2.24}$$

- Energy of the species (partial enthalpy h_k or partial internal energy e_k) and mixture energy (temperature T, enthalpy h, internal energy e):

$$h = \sum_{k=1}^{ns} h_k Y_k\,, \quad e = \sum_{k=1}^{ns} e_k Y_k, \tag{2.25}$$

  where h and e are mass-specific quantities with units of J/kg.

- The pressure p of the mixture can be expressed as the sum of the partial pressures p_k of the individual species:

$$p = \sum_{k=1}^{ns} p_k. \tag{2.26}$$

  The description of the system is completed with an equation of state, such as the ideal gas law:

$$p = \rho T \sum_{s} R_s Y_s, \tag{2.27}$$

The progress of these variables in time and space is described by balance equations expressed as the following:

$$\underbrace{\frac{\partial \rho \Phi}{\partial t}}_{\text{Transient term}} + \underbrace{\nabla \cdot [\rho \mathbf{u} \Phi]}_{\text{Convective term}} = \underbrace{\nabla \cdot [\mathrm{D}_\Phi \nabla \Phi]}_{\text{Diffusive term}} + \underbrace{S_\Phi}_{\text{Source/sink term}}, \tag{2.28}$$

where D_Φ denotes the diffusion coefficient for the scalar Φ.

Applying equation (2.28) to the primitive variables, namely density, velocity, species, and energy, yields the following equations:

$$\frac{\partial \rho}{\partial t} + \nabla \cdot [\rho \mathbf{u}] = \dot{\rho}_s, \tag{2.29}$$

$$\frac{\partial \rho \mathbf{u}}{\partial t} + \nabla \cdot [\rho \mathbf{u}\mathbf{u}] = -\nabla p + \nabla \cdot \boldsymbol{\tau} + \mathbf{F} \tag{2.30}$$

$$\frac{\partial \rho Y_s}{\partial t} + \nabla \cdot [\rho \mathbf{u} Y_s] = \nabla \cdot [\rho D_s \nabla Y_s] + \dot{w}_s, \tag{2.31}$$

$$\frac{\partial \rho h}{\partial t} + \nabla \cdot [\rho \mathbf{u} h] = \frac{\mathrm{d}p}{\mathrm{d}t} - \nabla \mathbf{j} + \dot{q}_{ev}, \tag{2.32}$$

where $\dot{\rho}_s$ denotes the source term due to evaporation, τ the stress tensor. $\mathbf{F}$ represents all the external forces that can be applied externally on the fluid. Y_s represents species mass fractions, and $\dot{w}_s$ is the mass source term due to chemical reactions. h represents the total enthalpy, $\mathbf{j}$ the heat flux vector, $\dot{q}_{ev}$ the total enthalpy source term due to droplet evaporation provided by the spray model.

These equations are expressed for low-Mach number flows, implying that viscous heating can be neglected. For non-reactive cases, i.e. the reaction rates are zero, the species mass fractions stay constant, their progress in space and time is only due to convection and molecular diffusion. However, in reactive cases, where the species distribution constructs the flame structure, it is necessary to track the development of all species in the mechanism. The large number of equations and the multiple stiff chemical source term integration present an initial difficulty for reacting flow modeling.

2.5 Turbulence modeling

Several methods are available for solving the flow equations. These equations take different forms depending on the approach utilized. The most commonly used are Direct Numerical Simulation (DNS), Large Eddy Simulation (LES), and Reynolds Averaged Navier-Stokes (RANS). Each offers a solution to the described equations, but they vary significantly in terms of accuracy and computational cost.

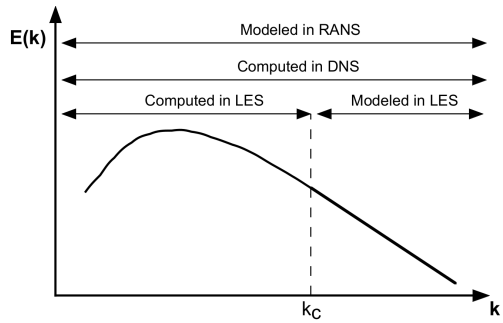

Figure 2.4: *Representation of the different turbulence models on the energy spectrum. k_c is the LES cut-off length [19]*

Direct Numerical Simulation (DNS)

The Direct Numerical Simulation (DNS) resolves all temporal and physical scales, implying no use of modeling for the flow, however, chemistry almost always relies on modeling. The cost of DNS simulations increases with the turbulence level and the size and complexity of the simulated case. The current set of hardware is unable handle medium to high Reynolds number DNS simulations in reasonable simulation times. It requires time frames in the order of decades, which is unrealistic for industrial applications. Model validation investigations use the results generated from detailed DNS to develop simpler models that attempt to solve similar problems to reduce the simulation times.

Large-Eddy Simulation (LES)

LES applies a spatial filter to the Navier-Stokes equations, separating the larger, directly resolved scales from the smaller, sub-grid scales that are computationally expensive to resolve directly. LES resolves structures down to the filter width level whereas the minor scales are modeled. This can be mathematically described as

$$\psi = \hat{\psi} + \psi', \tag{2.33}$$

where $\hat{\psi}$ refers to the filter resolved quantity and ψ' represents the unresolved part. LES models that do not incorporate combustion subgrid closure present uncertainties in applications where small turbulent scales can significantly affect chemistry and flow field. This can lead to inaccuracies in predicting critical phenomena such as ignition and extinction.

Reynolds-Averaged Navier-Stokes (RANS)

Simulating complex geometries with large Reynolds numbers often requires approximating the turbulent structures. This approximation is achieved by modeling various scales and applying averaging methods to the governing equations. Each quantity is decomposed into a mean $\bar{\psi}$ and a fluctuating ψ' component:

$$\psi = \bar{\psi} + \psi'. \tag{2.34}$$

The Reynolds Averaged Navier-Stokes (RANS) turbulence model [66] boils down to performing a time or ensemble averaging on the governing equations. For non-constant-density flows, a density-weighted averaging is applied, known as Favre averaging:

$$\psi = \tilde{\psi} + \psi''. \tag{2.35}$$

The averaging of $\rho\psi$ leads to:

$$\rho\psi = \overline{\rho\psi} + (\rho\psi)', \tag{2.36}$$

with

$$\tilde{\psi} = \frac{\overline{\rho\psi}}{\bar{\rho}} \quad , \quad \psi'' = \frac{(\rho\psi)'}{\bar{\rho}} \quad \text{and} \quad \overline{\rho\psi''} = 0. \tag{2.37}$$

All the quantities in the governing equations are Favre-averaged except for density, pressure, and diffusive fluxes. This averaging conveys that only the integral length scale is resolved, whereas all the other structures in the inertial and viscous subrange are modeled. The work realized in this thesis utilizes a RANS turbulence model. RANS is substantially cheaper than LES. However, it omits a large degree of information due to modeling of all structures below the integral scale. The low resolution of RANS is addressed by the additional model presented in chapter 3, i.e., the Linear Eddy Model.

The governing equations take the following forms after applying the Favre averaging.

$$\frac{\partial\bar{\rho}}{\partial t} + \nabla\cdot[\bar{\rho}\tilde{\mathbf{u}}] = \bar{\dot{\rho}}_s, \tag{2.38}$$

$$\frac{\partial\bar{\rho}\tilde{\mathbf{u}}}{\partial t} + \nabla\cdot[\bar{\rho}\tilde{\mathbf{u}}\tilde{\mathbf{u}}] = -\nabla\bar{p} + \nabla\cdot[\bar{\boldsymbol{\tau}} - \bar{\rho}\widetilde{u_i''u_j''}] + \tilde{\mathbf{F}}, \tag{2.39}$$

$$\frac{\partial\bar{\rho}\tilde{h}}{\partial t} + \nabla\cdot[\bar{\rho}\tilde{\mathbf{u}}\tilde{h}] = \frac{d\bar{p}}{dt} - \nabla\cdot[\bar{\rho}\widetilde{u_i''h''} + \bar{\mathbf{j}}] + \bar{\dot{q}}_{ev}, \tag{2.40}$$

$$\frac{\partial\bar{\rho}\tilde{Y}_s}{\partial t} + \nabla(\bar{\rho}\tilde{\mathbf{u}}\tilde{Y}_s) = \nabla\cdot\left[\bar{\rho}D_s\nabla\tilde{Y}_s - \bar{\rho}\widetilde{u_i''Y_s''}\right] + \bar{\dot{w}}_s, \tag{2.41}$$

where $\widetilde{u_i''u_j''}$ denotes the Reynolds stress term and $\widetilde{u_i''h''}$ and $\widetilde{u_i''Y_s''}$ represent the enthalpy and species turbulent fluxes, respectively.

By using the Boussinesq assumption for the turbulent eddy viscosity [67], the term $\widetilde{u_i''u_j''}$ is linked to the mean velocity gradient in the flow using the turbulent viscosity, also knows as the Reynolds or residual stresses:

$$\bar{\rho}\widetilde{u_i''u_j''} = \frac{2}{3}\bar{\rho}\tilde{k}\delta_{ij} - \mu_t\left(\nabla\tilde{\mathbf{u}} + (\nabla\tilde{\mathbf{u}})^T - \frac{2}{3}\delta_{ij}\nabla\cdot\tilde{\mathbf{u}}\right), \tag{2.42}$$

where δ_{ij} is the Kronecker delta. Turbulence closure within RANS revolves around determining the turbulence viscosity, denoted by μ_t. Classical turbulent models that are

utilized for non-reactive flows are also employed in reactive cases, such as zero-equation Prandtl mixing length model [68], Prandtl-Kolmogorov one equation model, or a two-equations model. This work utilizes the $k-\varepsilon$ two-equation model [69], where the eddy viscosity is modeled as the following:

$$\mu_t = \bar{\rho} C_\mu \frac{\tilde{k}^2}{\tilde{\varepsilon}} \quad , C_\mu = 0.09. \tag{2.43}$$

The turbulent kinetic energy k and the turbulent dissipation rate ε are calculated using the classical $k-\varepsilon$ model by Launder and Spalding [70], that advances the transport equations for these two terms in its variable density form:

$$\frac{\partial(\bar{\rho}\tilde{k})}{\partial t} + \nabla \cdot [\bar{\rho}\tilde{\mathbf{u}}\tilde{k}] = \nabla \cdot [(\mu + \frac{\mu_t}{\sigma_k})\nabla \tilde{k}] + P_k - \bar{\rho}\tilde{\varepsilon}, \tag{2.44}$$

$$\frac{\partial(\bar{\rho}\tilde{\varepsilon})}{\partial t} + \nabla \cdot [\bar{\rho}\tilde{\mathbf{u}}\tilde{\varepsilon}] = \nabla \cdot [(\mu + \frac{\mu_t}{\sigma_\varepsilon})\nabla \tilde{\varepsilon}] + C_{\varepsilon 1}\frac{\tilde{\varepsilon}}{\tilde{k}}P_k - C_{\varepsilon 2}\bar{\rho}\frac{\tilde{\varepsilon}^2}{\tilde{k}}, \tag{2.45}$$

where the model constants are the following:

$$C_\mu = 0.09; \quad \sigma_k = 1.0; \quad \sigma_\varepsilon = 1.3; \quad C_{\varepsilon 1} = 1.44; \quad C_{\varepsilon 2} = 1.92 \tag{2.46}$$

and the source term P_k is provided as:

$$P_k = -\bar{\rho}\widetilde{u_i'' u_j''}\frac{\partial \tilde{u}_i}{\partial x_j}. \tag{2.47}$$

The terms $\widetilde{u_i'' h''}$ and $\widetilde{u_i'' Y_s''}$ are evaluated based on a classical gradient flux assumption:

$$\bar{\rho}\widetilde{u_i'' h''} = -\frac{\mu_t}{Sc_t}\nabla \tilde{h}, \tag{2.48}$$

$$\bar{\rho}\widetilde{u_i'' Y_s''} = -\frac{\mu_t}{Sc_t}\nabla \tilde{Y_s}. \tag{2.49}$$

These approximations provide closing for equations (2.39), (2.40) and (2.40).

2.6 Combustion Modeling

Simulating turbulent combustion with CFD provides a grid on which transport equations are discretized in time and space. In combustion simulations, assessing species mass fractions distribution in the CFD domain is essential for accurately predicting combustion. This is naturally realized by advancing transport equations of species mass fractions described in equation (2.31) with a reaction rates closure provided from a selected combustion model. Other techniques involve replacing the transport equations of all individual species with other representative equations such as mixture fraction and/or progress variable to reduce the computational cost, e.g. in the case of using large chemical mechanisms. The attempt to create a unique combustion model that captures all physical aspects for all relevant scales has always been the ultimate goal for combustion model

developers; it remains, however a difficult modeling problem due to the presence of different modes and regimes. The practical solution often was to develop numerical models dedicated to specific applications by employing particular assumptions to simplify the problem. However, the often made assumptions of infinitely fast or fast chemistry do not always realistically describe the combustion process.

2.6.1 Burke-Schumann & Bray-Moss-Libby Models

Burke and Schumann for diffusion flames [71] and Bray-Moss-Libby for premixed flames [15] suggested solutions valid for infinitely fast irreversible chemistry, where the chemical time scales are shorter than all other time scales, i.e. combustion is reaction-controlled only with Da >> 1. This implies that the equilibrium state is instantly reached, and that turbulence has no influence on chemistry. However, a complex chemical reaction mechanism features a very broad range of time scales with reversible reactions, conveying that chemistry can interact with the flow. As a result, in a real flame the thermodynamic equilibrium state is not reached and the difference to the equilibrium state can be vast. In addition, the formation and destruction rates are different between each species, which implies the existence of different chemical time scales, e.g., CO oxidation is faster than CO_2, while NOx formation is significantly slower. In conclusion, incorporating finite-rate chemistry and reversible reactions is essential for modeling realistic combustion processes and predicting pollutant formation.

2.6.2 Eddy Break Up & Eddy Dissipation Models

Spalding introduced the Eddy Break-Up Model (EBU) [17, 18] as an attempt to provide chemical closure in mixing dominated premixed combustion scenarios. The central hypothesis behind the EBU model states that in scenarios where mixing is the rate-determining process, the turbulent cascade controls the chemical reactions. The EBU suggests replacing the chemical time scales with the turbulent ones $\tau = \frac{k}{\varepsilon}$, which corresponds to applying the fast chemistry assumption. Spalding's formulation of the turbulent mean reaction rate $\overline{w}_p$ was based on a characteristic turbulent mixing time, the variance of the temperature fluctuation and EBU constant C_{EBU}.

$$\overline{w}_p = C_{EBU}\bar{\rho}\frac{\sqrt{\widetilde{T''^2}}}{\tau_{EBU}}, \tag{2.50}$$

where $\tau_{EBU} = k/\varepsilon$. Magnussen and Hjerteger proposed a modification of the EBU, titled the Eddy Dissipation model/concept EDC [20], where $\bar{w_p}$ was expressed based on the mean mass fraction of the product rather than the variance and with different model constants. Both EBU and EDC neglect the effect of chemical kinetics caused by treating only the fast chemistry limit.

2.6.3 Well & Partially Stirred Reactor Models

The Well Stirred Reactor (WSR) is a simplistic approach used for combustion closure. It implies advancing transport equations of all species in the mechanism, with source terms

calculated based on resolved mean values. Although this approach is prevalent in ICE simulations [21], it completely neglects the effects of turbulence chemistry interactions discussed in section 2.3. This limit can be problematic, especially in scenarios where these interactions are important, e.g. pollutant formation, ignition and extinction. The chemical source terms are calculated as the following:

$$\dot{\omega}_s = \frac{\rho(\widetilde{Y_{s,1}} - \widetilde{Y_{s,0}})}{\Delta t}, \tag{2.51}$$

$$\dot{q} = \sum_{i=1}^{ns} \frac{\rho \Delta h^0_{f,i} (\widetilde{Y_{s,1}} - \widetilde{Y_{s,0}})}{\Delta t}, \tag{2.52}$$

where $Y_{i,0}$ and $Y_{i,1}$ are the mass fraction of species s before and after integration, respectively. $\Delta h^0_{f,i}$ denotes the chemical enthalpy at the reference temperature of the i-th species. Chomiak [22] introduced an extension of the WSR model named Partially Stirred Reactor (PaSR). The PaSR concept is based on dedicating one region of the computational cells to chemical reactions and another to the mixing process as an attempt to capture the TCI. It was used to provide combustion closure for an ICE simulation in several publications such as [72].

2.6.4 Flamelet Model

A more sophisticated model that includes TCI is the flamelet model proposed first by [73] for non-premixed combustion and which is used to simulate finite rate chemistry. A *flamelet*, as previously mentioned in section 2.3, is a thin reactive zone embedded in a non-reactive flow. The turbulent flame in flamelet modeling can be broken down into several stretched laminar flamelets. The flamelet equations were first derived for diffusive flames, where a passive non-reactive scalar, i.e., mixture fraction Z, is utilized to describe the fuel distribution in the domain. The following flamelet equations were derived by applying a variable change on the transport equation of a reactive scalar from (x_1, x_2, x_3, t) to (Z, y_2, y_3, t), where y_2 and y_3 are spatial variables that describe a plane tangential to the stoichiometric mixture fraction iso-surface:

$$\rho \frac{\partial \psi_i}{\partial t} = \frac{\rho}{Le_i} \frac{\chi}{2} \frac{\partial^2 \psi_i}{\partial Z^2} + \dot{\omega}_i, \tag{2.53}$$

where $\dot{\omega}_i$ denotes the source term of the reactive scalar ψ_i and Le_i the Lewis number (D_i/D_{mix}), where D_i is the diffusion coefficient of species i and D_{mix} is the mixture diffusion coefficient. $\chi = 2D\left(\partial Z/\partial x_1\right)^2$, i.e., the scalar dissipation rate, has the unit of the inverse of time and describes the diffusive process of the scalar ψ_i in mixture fraction space. The flamelet model is conceptually applicable only in the flamelet regime, where gradients can be neglected in y_2 and y_3 compared to gradients perpendicular to the $Z = Z_{st}$ iso-surface. However, it has also been often successfully applied outside the flamelet regime. Some of the models that utilize the flamelet concept in non-premixed combustion are the Representative Interactive Flamelet (RIF) [29], the multiple RIF (mRIF) [30, 74] and the Eulerian Particle Flamelet model [75]. These flamelet approaches

are used in conjunction with a presumed β-PDF, whose shape is determined by the mean and variance of the conserved scalar Z. The flamelet concept can also be used for modeling premixed combustion by utilizing a level-set G equation and a variance G equation combined with a presumed PDF technique.

2.6.5 Conditional Moment Closure Model

Bilger [76] and Klimenko [31] independently suggested a new combustion model named Conditional Moment Closure (CMC). CMC is based on the concept that diffusion of turbulent scalars can be modeled more accurately in mixture fraction space rather than physical space. CMC exploits the correlation in the reactive scalar and mixture fraction space fluctuations to condition the reactive scalars in mixture fraction space. They are advanced as transport equations of conditioned reactive scalars $\langle \rho \phi_k | Z \rangle$, where specific terms, such as conditioned velocity and conditioned scalar dissipation rate, are closed by simple models. CMC was also inspected for premixed cases where the conditioning was realized on the progress variable. CMC managed to deliver good closure for the source term of the progress variable; however, it lacks the spatial and temporal description of the probability density function of the progress variable, a topic largely discussed in the combustion community. Hence, this model was deemed to uniquely predict the finite rate chemistry process for non-premixed combustion cases. Moreover, the first-order CMC equations closely resemble the laminar flamelet equations but include additional unclosed terms, namely the conditional velocity, which comes from the convective term, and the conditionally averaged scalar dissipation

2.6.6 Transported PDF Model

The transported PDF (T-PDF) model was introduced by Pope [23] as a transport equation in time and space of a joint PDF function that describes the hydrodynamic and/or thermodynamic state of the reactive mixture. PDF models typically provide exact closure for the problematic chemical reaction term in turbulent combustion. The single-point statistics assumption that the T-PDF is mostly based on makes the T-PDF a robust combustion model able to predict different combustion modes. However, the transport equation introduced by Pope does not directly account for the scalar gradient of the joint PDF, implying no direct description of molecular mixing time which is particularly important for flame structures. Additional mixing models are introduced to solve this issue: The Interaction by Exchange with the Mean (IEM) utilizes the Linear Mean Square Estimation (LMSE) by [77], which suggests the relaxation of the scalar values to the mean. IEM was shown to work well for non-reactive flows; however, scale separation was assumed between turbulence and chemistry in the case of reactive flows. Curl [78] proposed the C-D mixing model, where mixing is assumed to happen in pairs between two particles, where the result of mixing is the mean of the particles before mixing. This model presented the issue of the inaccurate prediction of the relaxation of the initial PDFs. This problem was solved by [79], where the degree of mixing was a uniformly distributed random variable. Mapping Closure is an additional mixing model for the T-PDF introduced by [80], where they suggested mapping the scalar field to a Gaussian

reference space. This model has solved two problems: the non-locality in reactive scalar space and the inability to predict the relaxation of a particular PDF to a Gaussian.

2.7 The Linear Eddy Model

The LEM development aims to acquire a regime and mode-independent model that provides an affordable full resolution of all spatial and temporal scales, including the minor scale effects in combustion. Compared to standard modeling approaches, which usually rely on modeling/simplifying physical processes (e.g. via a gradient diffusion assumption), LEM modeling is based on domain reduction, i.e. mixing and combustion is represented as a fully unsteady process on a one-dimensinal domain resolving all scales in space and time as in a DNS. This dimensional reduction requires a particular approach to represent certain physical phenomena, namely turbulent advection. It also implies time-advancement of unsteady reactive 1D zero Mach number equations complemented with a stochastic process for turbulent eddy representation along a one-dimensional line representing the simulated domain's statistical state. The advancement of LEM is composed of diffusion of reactive scalars, chemical reactions, and turbulent advection. The LEM 1D zero Mach number equations have the following form in a planar reference:

$$\rho \frac{\mathrm{d}\phi}{\mathrm{d}t} = \frac{\partial}{\partial x}\left(\rho D_\phi \frac{\partial \phi}{\partial x}\right) + \dot{w}_\phi, \tag{2.54}$$

where ϕ denotes a reactive scalar, ρ the density, D_ϕ and $\dot{w}_\phi$ are the diffusion coefficient and the source term of the scalar ϕ, respectively. The thermal equation of state of the mixture of ideal gases is typically assumed in LEM:

$$p = \rho T \sum_s R_s Y_s, \tag{2.55}$$

where R_s conveys the individual gas constant of species s.

Turbulence is simulated in LEM by executing independent eddy events. The simulation of the turbulent vortices on the line is performed by the triplet mapping process, which models the impact of the turbulent 3D vortices on the scalar profiles implemented on the one-dimensional line as described in Figure 2.5. Triplet maps ensures continuity of profils and conservation of mass and energy. The triplet mapping process is based on three steps:

1. Compression of the eddy interval by a factor of three,
2. Creation of three identical copies of the compressed segment,
3. Inverting the middle segment and reconnecting the three lines.

The set of equations of species and energy in the form of (2.54) are solved using a second-order accurate scheme employing a central discretization of the diffusion terms. The temperature in the LEM cells is calculated using the calorific equation of state (3.32). The transport, thermodynamic parameters and the chemistry are assessed using

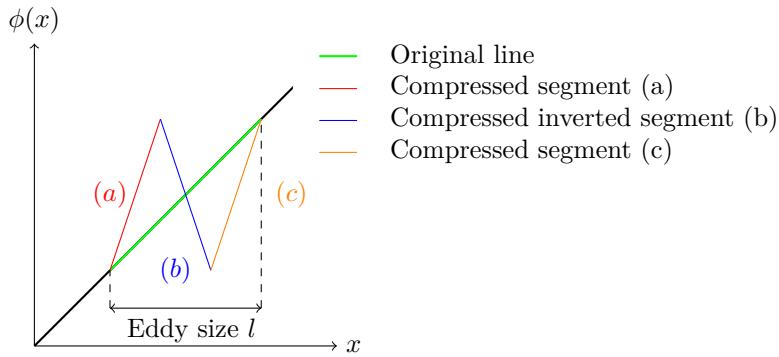

Figure 2.5: *Representation of a triplet map in a planar LEM*

the CANTERA package [81], where the stiff chemical source term is integrated using SUNDIALS' implicit BDF method [82].

The shear eddies simulated in LEM reside within the inertial subrange, defined by scales ranging between the integral length scale and the Kolmogorov length scale. The CFD provides the turbulence parameters $\tilde{k}$ and $\tilde{\varepsilon}$ that determine the LEM parameters, namely, the turbulence diffusivity D_t, the integral length scale l_t, the Kolmogorov length scale η and the average time between the eddies. Originally, only the shear eddies were simulated on the LEM; however, large eddies must be simulated in the context of moving volume (piston) due to the large-scale motions such as tumble or swirl. These large movements significantly enhance the mixture in a real engine; ignoring them in a LEM simulation leads to notable discrepancies between the LEM and CFD.

2.7.1 Eddies selection and sampling

The distribution defined in equation (2.56) and described in length in [24], determines the size distribution of eddies that exist between the integral and the Kolmogorov length scale.

$$f(l) = \frac{5}{3} \frac{l^{-8/3}}{\eta^{-5/3} - l_t^{-5/3}}, \tag{2.56}$$

where l indicates the size of the eddies, l_t is the integral length scale and η is the Kolmogorov length scale. The integral length scale l_t is calculated on LEM as the following:

$$l_t = \frac{D_t}{u'}, \tag{2.57}$$

with D_t denotes the turbulent diffusivity:

$$D_t = \frac{C_\mu}{Sc_t} \frac{\tilde{k}^2}{\tilde{\varepsilon}}, \tag{2.58}$$

and u' is the velocity fluctuations defined as:

$$u' = \sqrt{\frac{2\tilde{k}}{3}}. \tag{2.59}$$

η on LEM is calculated based on the inertial scaling law described in [24] with

$$\eta = N_\eta l_t Re_t^{-3/4}, \tag{2.60}$$

where Re_t is the turbulent Reynolds number:

$$Re_t = \frac{u' l_t}{\nu}. \tag{2.61}$$

The values assigned to the model constants $C_\lambda = 15$, $C_\mu = 0.09$ and $N_\eta = 10.76$ are based on literature values [83]. The eddy event frequency per unit length is determined using the above-defined quantities, and is described as the following:

$$\lambda = \frac{54}{5} \frac{\nu Re_t}{C_\lambda l_t^3} \frac{(l_t/\eta)^{5/3} - 1}{1 - (\eta/l_t)^{4/3}}. \tag{2.62}$$

The eddy event time on the LEM domain is determined based on a sampling under a Poisson process assumption with mean eddy occurrence time:

$$\Delta\tau_{eddy} = (\lambda L)^{-1}, \tag{2.63}$$

where L characterizes the length of the LEM domain. Finally, the eddy location is specified based on the left edge of the eddy, and it is sampled uniformly on the LEM domain.

2.8 Spray Modeling

The detailed modeling of the spray break-up and mixture formation is essential for an accurate prediction of the combustion process, namely ignition and pollutants formation.

2.8.1 Break-up Regimes of Liquid Jets (primary break-up)

The break-up of a liquid jet is dominated by the properties of the liquid jet and the surrounding gaseous phase and their relative velocity. Reitz and Bracco [84] identified four break-up regimes:

- **Rayleigh regime:** The combination of liquid phase inertia and surface tension forces initiate the growth of liquid jet oscillations in the axis-symmetric direction. This leads to the jet break-up and the formation of liquid droplets with sizes greater than the nozzle diameter.
- **First wind-induced regime:** The velocity increase causes the break-up length and the average droplet size to decrease to a size equivalent to the nozzle diameter.

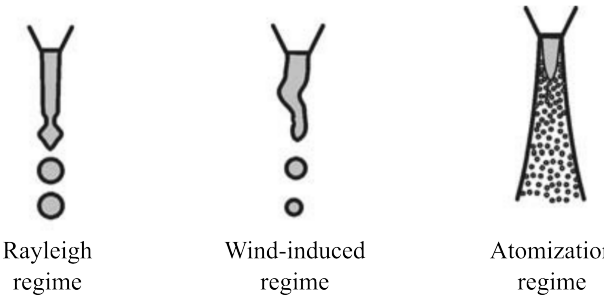

Figure 2.6: *Representation of jet break up regimes [85]*

- **Second wind-induced regime:** The velocity increase causes the flow to become turbulent around the nozzle. The droplet diameter becomes smaller than the nozzle diameter, and the break-up length decreases. i.e., the break-up occurs closer to the nozzle.
- **Atomization regime:** Atomization occurs when the intact surface length reaches zero, where droplet sizes are much smaller than the nozzle diameter. The atomization regime is the relevant regime for engine sprays.

The Weber number, which provides a ratio between fluid inertia and viscous forces, is utilized to identify the liquid jet's break-up regime. It is defined as:

$$W_e = \frac{\rho_l U^2 D}{\sigma}, \tag{2.64}$$

where ρ_l denotes the density of the liquid phase, D the nozzle diameter, U the velocity of the jet, and σ the surface tension at the liquid gas interface.
In engines, sprays are injected into the cylinder with pressures up to 200 MPa and velocities up to 500 m/s in diesel engines. The liquid jet penetrates the combustion chamber and immediately goes primary and secondary break-up forming a spray of conical shape with very fine droplets. Droplet velocities are highest along the spray axis; they decrease at the surrounding of the spray due to interactions with the surrounding gas. In the dense spray region, a high chance of collision and coalescence exists, which impacts the droplets by changing their velocities and diameters. In this study, however, we rely on the simply blob model for primary break-up.

***The Blob-Model*:** The blob method suggested by Reitz and Diwakar [86] is considered the most popular method for describing the initial conditions of a diesel spray next to the nozzle hole. It states that the droplet break-up and atomization of a dense spray near the nozzle are two indistinguishable processes. In this case, instead of simulating the complex fluid dynamic structures of the fuel inside the nozzle, an injection of a uniform spherical droplet called *blob* right after the nozzle hole is realized. This blob has a diameter equal to the nozzle hole exit and will be exposed to interaction with the gaseous phase via secondary aerodynamic-induced break-up. The blob method is widely used in case no

detailed information about the size distribution of droplets at the exit of the nozzle is available from complex simulations or experimental measurements. Other models, such as Kuensberg's [87] model, suggested an advanced blob method that considers the cavitation inside the nozzle by reducing the blob diameter.

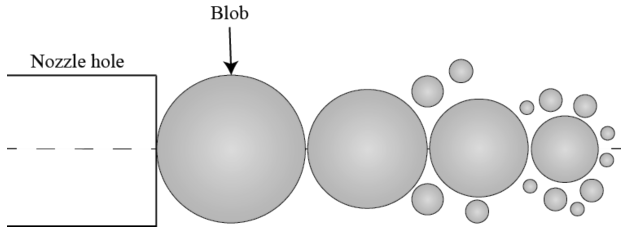

Figure 2.7: *Representation of the blob injection method*

2.8.1.1 Secondary Break up

The secondary break-up describes the disintegration of an existing droplet generated by the primary break-up into smaller droplets. This deterioration is due to aerodynamic forces created due to the relative velocity between the liquid and gas phases.

2.8.2 Break-up Regimes of Liquid Droplets (secondary break-up)

Droplet break-up occurs because of aerodynamic forces (friction and pressure) created due to the relative velocity between the liquid and gaseous phases. The aerodynamic forces create instabilities on the droplet's surface through waves. These waves lead to the disintegration of the droplet once a specific wave frequency threshold is reached. The surface tension forces oppose the surface instability to maintain the droplet from dissolving. This is reflected in the droplet Weber number. This regime can be described using the following models:

***Kelvin-Helmholtz (KH)*:** This mode can be used to describe both jet break-up and secondary droplet break-up. It is based on the Kelvin-Helmholtz Instability (KHI) analysis [89, 90]. Due to aerodynamic forces generated by the relative velocity between the liquid and the surrounding gas, the surface of the jet becomes covered with sinusoidal waves, which cause axisymmetric fluctuations in pressure as well as axial and radial velocity components in both the liquid and the gas. The KH model suggests an equation that accounts for the dispersion relation, which relates the growth rate of a perturbation to its wavelength. The numerical analysis of this equation yields a solution where the growth rate of perturbations reaches a maximum, leading to the detachment of ligaments or droplets from the jet, resulting in primary or secondary break-up, respectively. The resulting ligament or droplet is then added to the computational domain with a size proportional to the wavelength of the parent structure. However, the KH model forms strong Bimodal distributions of the spray, which is unrealistic for high-pressure injections. The KH model is usually combined with the following RT model.

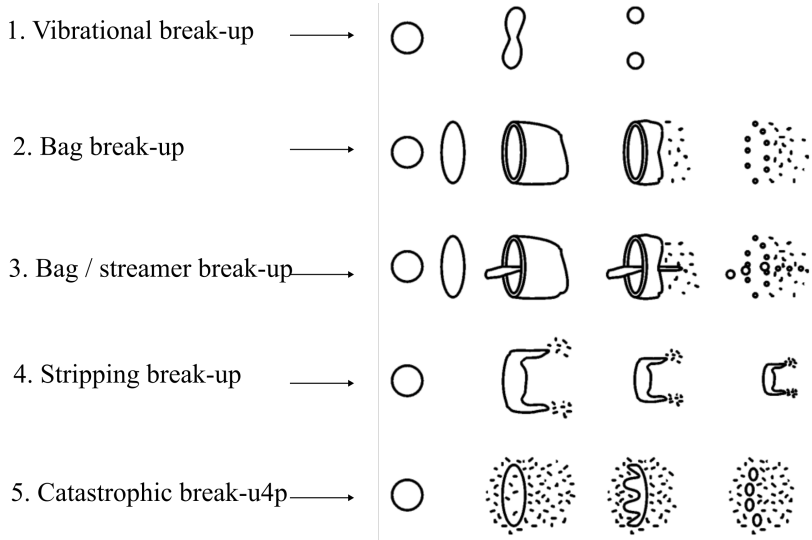

Figure 2.8: *Representation of liquid droplet break up regimes [88]*

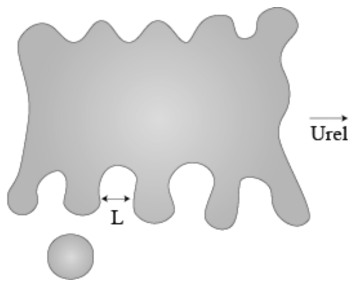

Figure 2.9: *Representation of KH break up regime*

***Rayleigh Taylor RT*:** This model investigates the instability between two fluids with different densities in case of acceleration or deceleration [91]. The interface is stable if the acceleration is oriented into the fluid with higher density and vice versa for instability. The break-up mechanism behind this model makes the droplet completely disintegrate into several child droplets, which diameter is proportional to the wavelength of the parent droplet. The droplet is allowed to break up only if the wavelength is smaller than its diameter and the break-up time is reached, which is proportional to the wavelength. This mechanism accurately describes the catastrophic break-up mode known in the literature. This mechanism is valid near the nozzle; however, further downstream, a stripping process is more relevant. Therefore, the RT break-up mechanism is usually combined with the KH break-up model, as explained next.

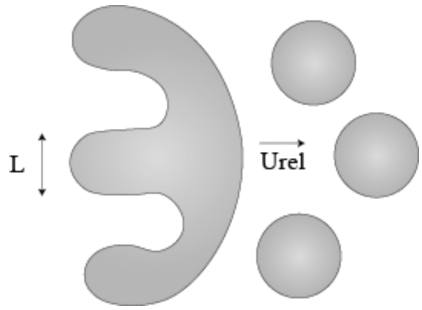

Figure 2.10: *Representation of RT break up regime*

2.8.2.1 Combined Models

***Blob-KH/RT Model*:** Different breakup regimes usually exist in engine sprays. Therefore, one breakup model is usually insufficient to describe the atomization process and mixture formation inside the cylinder. Here, primary breakup is represented by the blob model, where droplets are injected with a diameter equal to the nozzle's existing hole diameter (if no cavitation is considered). Two secondary breakup models are used concurrently, namely the KH and the RT model. The two models grow unstable waves because of the relative velocity simultaneously. If one of the two models predicts a breakup event in the corresponding time step for (example, KH), tiny droplets will be created, and the diameter of the parent droplet will be reduced. Otherwise, if RT predicts a breakup event, the whole droplet will disintegrate into several child droplets with a diameter proportionate to the parent droplet wavelength. This method prevents the generation of the bimodal functions that appear if the KH model is employed alone. Typically, the KH model is used in the dense core region of the spray; the RT model is applied after a certain breakup length, where both models coexist. However, experimental observations by Hwang et al.[92] have stated that the shape of the droplets after the breakup length is not perfectly spherical as the RT model describes but is slightly flattened by the aerodynamic forces. Other combined models, such as the blob-KH/DDB model, are designed to explain this phenomenon, where the Droplet Deformation Breakup model is used instead of the RT model, and no transitory region exists between the KH and DDB model around the breakup length.

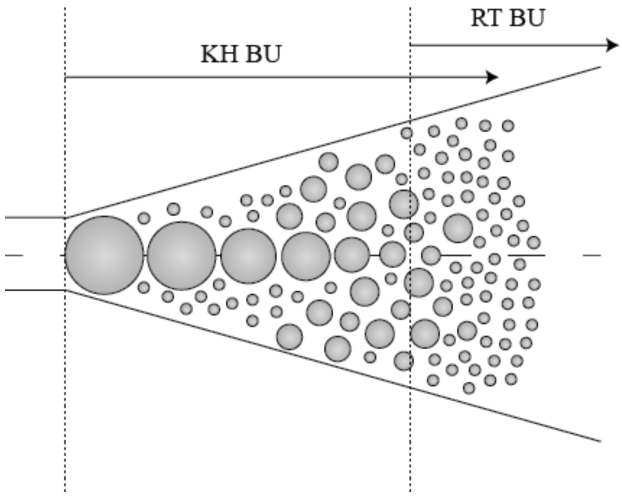

Figure 2.11: *Representation of KH-RT break up model*

3 RILEM

The LEM has historically been used as a combustion closure model for large eddy simulations [43, 45, 93]. In case of RILEM, which stands for Representative Interactive Linear Eddy Model, it incorporates a RANS-CFD simulation coupled with the Linear Eddy Model. RILEM aims to solve RANS equations for combustion engine simulations, which is relatively cheap compared to other approaches. The combustion closure is realized via LEM, where turbulence is resolved down to dissipative scales. This allows a better prediction of turbulence chemistry interactions, which enhances the prediction of flame structure and pollutant formations. However, to accurately predict the combustion process, LEM was required to be first, representative, which entails experiencing the same process that the CFD witnessed, and second, interactive, implying a back-and-forth feedback communication with the CFD.

3.0.1 LEM time advancement

The LEM framework incorporates three concurrent processes; Turbulent advection, molecular diffusion/heat conduction, and chemistry advancement. Diffusion and chemistry are implemented using a Strang operator splitting as presented in Figure 3.1.

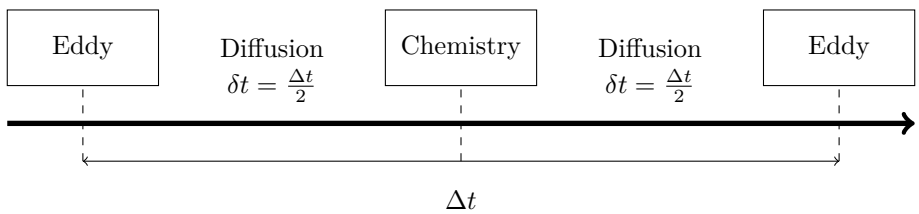

Figure 3.1: *Representation of the diffusion-chemistry process in LEM*

The time step Δt is defined as the duration between two consecutive eddy events in the original ODT code. The Strang operator splitting divides Δt into two halves $\delta t = \frac{\Delta t_{LEM}}{2}$ on which the diffusion is advanced implicitly. The stiff chemical source term is integrated over the entire Δt time step in between the diffusion steps using CVODE from Sundials [82]. Eddy events on the other hand are implemented instantaneously.

In the original ODT code used here, the LEM process is implemented in a way that the LEM time step is decomposed into several Δt based on the sampled eddy occurrence times, which is decided based on the number of eddy events sampled in the corresponding time-step, this process is described in Figure 3.2. Although that approach is considered the statistically most consistent implementation, the successive interruption and re-start of the CVODE chemistry solver substantially slows down the simulation.

The overall simulation time was substantially reduced by employing two different strategies. The initial approach was to decompose the LEM line into several parts where chemistry is

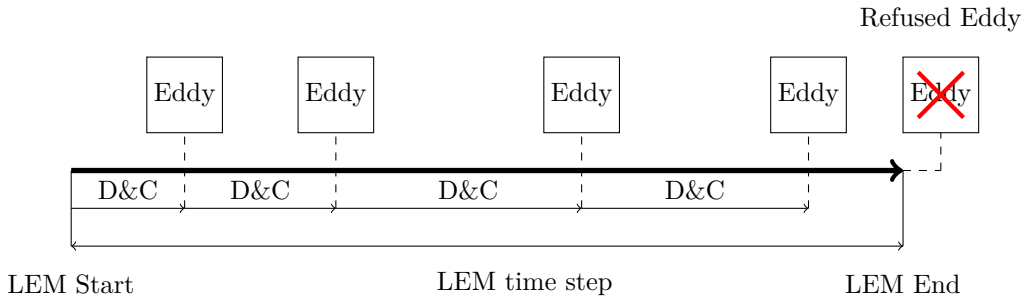

Figure 3.2: *Traditional LEM advancement framework*

solved in parallel. This method utilizes OpenMP multithreading, where several chemistry solvers are initialized simultaneously, and each solver integrates the chemical source terms for a dedicated section of the line. The second strategy was to cluster the eddies planned to be sampled on the corresponding LEM time step and implement them by sampling order at the start of the time step, as depicted in Figure 3.3. The Strang Operator Strategy is correspondingly applied in this approach with $\delta t = \frac{\Delta t_{LEM}}{2}$, where the diffusion is advanced on δt and chemistry is integrated over Δt_{LEM}. The eddy clustering approach was introduced for a specific strategy where multiple LEM lines are advanced in parallel.

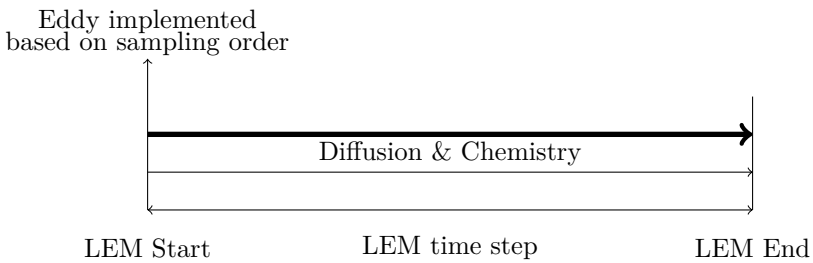

Figure 3.3: *Eddy Clustering Framework*

It will be shown later in the thesis that multiple LEM lines are required to acquire a reasonable simulation output. It is essential to note that eddy clustering is susceptible to the selected time step. The LEM implements numerous eddies for significant time steps and advances diffusion and chemistry over the extended time step. Setting a large time step corresponds to clustering several eddies before advancing diffusion and chemistry, which impacts the turbulent chemistry interaction effects. Therefore, choosing a reasonable time step is crucial for the eddy clustering approach.

3.1 Spherical Linear Eddy Model

3.1.1 Spherical Triplet Maps

The direct fuel injection with a typical injector for diesel engines leads to a conical spray shape. The original LEM code contains three different LEM geometries: planar, cylindrical, and spherical. Using the classical planar LEM geometry, which features a series of cubical cells, is not suitable for capturing conical spray development. For that, a spherical implementation of the line with a characteristic length equal to the combustion chamber bore is utilized to accurately represent the conical shape of the spray [58, 59]. The spherical LEM representation was functional in other ways for the RILEM model; this will be explained later in this chapter. Using the spherical LEM geometry required specific modifications, namely, on the level of the LEM transport equations and triplet maps. The spherical LEM requires solving the 1D zero Mach number equations in a spherical reference system with changes in radial direction only as follows:

$$\rho \frac{\mathrm{d}Y_s}{\mathrm{d}t} = -\frac{1}{r^2}\frac{\mathrm{d}}{\mathrm{d}r}\left(r^2 j_s\right) + M_s \dot{w}_s + \rho \dot{Y}_{s,ev}, \tag{3.1}$$

$$\rho \frac{\mathrm{d}h}{\mathrm{d}t} = -\frac{1}{r^2}\frac{\mathrm{d}}{\mathrm{d}r}\left(r^2\left[q + \sum_s j_s h_s\right]\right) + \frac{\mathrm{d}p}{\mathrm{d}t} + \rho \dot{h}_{ev}, \tag{3.2}$$

where ρ denotes density, Y_s, M_s, and $\dot{w}_s$ the mass fraction, the molecular weight, and the source term due to chemical reactions of species s, respectively. $\dot{Y}_{s,ev}$ is the source term due to fuel evaporation. h describes enthalpy, q the heat flux, h_s the enthalpy of species s, p the pressure, and $\dot{h}_{ev}$ the enthalpy due to the added evaporated fuel.

The spherical representation of LEM represented in figure 3.6 required an adaption of the triplet mapping process. In addition, both molecular diffusion and heat conduction occur across a spherical boundary, which requires a spherical adaptation to the fluxes. Implementing a triplet map on a spherical LEM can occur in three scenarios, depending on the eddy position on the line. We name A the left boundary and $B = A + L$ the right boundary of the eddy, respectively, and L is the eddy size.

1. Both A and B land on the left cone of the line

2. A land on the left cone and B lands on the right cone.

3. Both A and B land on the right cone of the line

The LEM implementation suggests a different rearrangement for each scenario. The mathematical derivation has been discussed at length in [55]. The following figure represents the different implementations for each scenario.

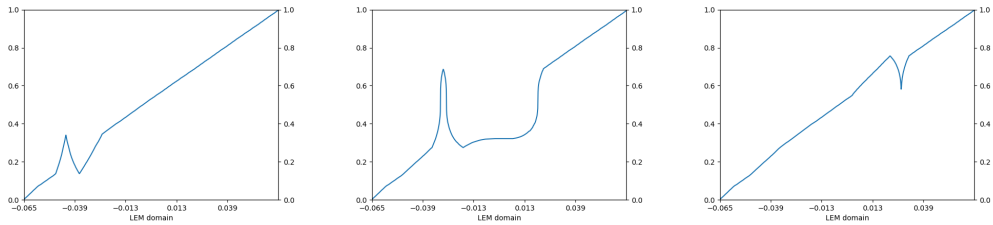

Figure 3.4: *Representation of spherical triplet maps per scenario: 1: To the left. 2: The middle. 3: To the right*

3.1.2 Pressure Coupling

The LEM line contains several cells that communicate with each other via molecular diffusion and heat conduction. A uniform pressure for all LEM cells is enforced to reflect the low Mach number assumption leading to a spatially homogeneous pressure. The LEM pressure is maintained equal to the average CFD pressure. However, fuel injection, diffusion, and combustion are local processes that lead to a change in the local composition and, thus, the pressure of the cells, which violates the constant pressure condition. In addition, the length of the LEM line is required to be equal to the characteristic length of the CFD domain to maintain the representative aspect between CFD and LEM. These two constraints were met by employing the spherical formulation of the LEM combined with the split operator strategy explained in the next paragraph.

Split Operator Strategy

Combustion on the LEM is implemented as a constant volume process in each cell, where the pressure is permitted to change locally and later adjusted to the prescribed CFD pressure. Similarly, the fuel injection process is also implemented as a constant volume process, where the new local densities are calculated based on the injected fuel mass in the cells. The choice of implementing these processes in constant volume leads to a change in the pressure of each cell, violating the constant pressure constraint of the LEM. Moreover, the pressure on the LEM should equal the CFD pressure. The split operator strategy was utilized to overcome these issues. It features three processes: First, the implementation of these processes under constant volume assumption allows the pressure in each cell to change. Second, an isentropic process that modifies the cell's volumes to expand/compress to reach a target pressure, i.e. the CFD pressure is realized based on the following:

$$V_2 = V_1 \left(\frac{p_1}{p_{CFD}} \right)^{1/\gamma}, \tag{3.3}$$

where p_{CFD} denotes the target CFD pressure. All LEM cell volumes will change to match the CFD pressure in this operation. It is important to note that the isentropic expansion/contraction is realized under the constraint of a constant cone angle leading to a (substantial) change of the length of the LEM line. This violates the representative

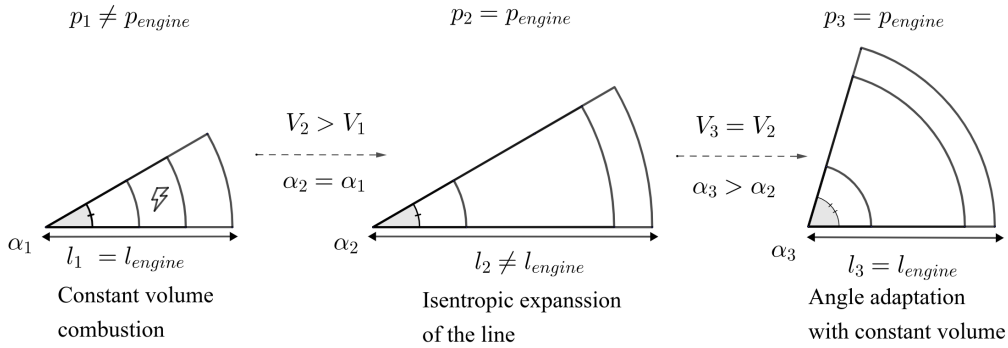

Figure 3.5: *Split Operator Strategy*

aspect of the model where the LEM line characterizes the cylinder bore here. The third step of the Split Operator Strategy utilizes the spherical formulation of LEM to resolve this issue. A new cone angle α of the line is calculated based on the condition that the LEM length matches the characteristic CFD length, as the following formula shows:

$$\alpha = \arccos\left(1 - \frac{12V_{LEM}}{\pi D^3}\right), \tag{3.4}$$

where D represents the combustion chamber's bore and the LEM length, and V_{LEM} denotes the total volume of the LEM line. This step ensures the conservation of the LEM's volume while matching the characteristic length and maintaining the constant CFD pressure on the LEM line. Finally, the LEM cell boundaries are recalculated based on the new cone angle. The isentropic process to adjust the pressure in each cell will result in a volume of the LEM domain which deviates from the volume of the CFD domain. Any large deviation might indicate that the LEM is not representative anymore for the combustion process. However, during the simulations presented in this thesis no significant deviations were noticed.

3.1.3 Fuel Mapping Strategy

The fuel injection is simulated as a 3D process on the CFD side using a Lagrangian spray model. LEM receives fuel only in the gas phase, which requires a specific strategy to correctly map the fuel on the LEM line. The first possible solution is to design an independent spray model on the LEM side. Although this solution is possible, it was not adopted for complexity reasons. Instead, the following quantities are provided from the CFD spray model to determine the fuel mapping on the LEM: Evaporated fuel mass, vapor deposition length, and the volume (fraction) of cells that experience evaporation. The choice of the second alternative is motivated by its simple implementation and the sustained consistency between LEM and CFD compared to the first approach. The fuel mapping strategy is based on two main quantities:

- **The LEM fuel penetration length**: It determines the number of LEM cells to which the fuel will be mapped.
- **The evaporated fuel mass**: It specifies the amount of fuel mass on the CFD that will be injected into the LEM domain.

The injector is defined as the center point of the two LEM cones. Due to the line's orientation along the spray axis, the total amount of fuel received by the LEM will be distributed between the two cones. The LEM vapor penetration length is calculated by matching the volume ratio of the cells with evaporation and the total volume of the combustion chamber on the LEM with the ratio evaluated on the CFD domain.

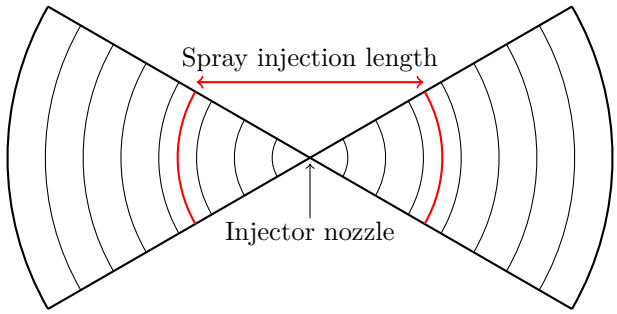

Figure 3.6: *Representation of the spray on the spherical double-coned LEM*

We calculate the LEM vapor penetration ratio on the CFD side as:

$$\beta = \frac{V_{ev}^{LEM}}{V^{LEM}} = \frac{V_{ev}^{CFD}}{V^{CFD}} \tag{3.5}$$

The volume with fuel evaporation can be calculated using β on the LEM side as:

$$V_{ev}^{LEM} = \beta V_{fuel}^{LEM} \tag{3.6}$$

Based on the spherical geometry of the LEM domain, the corresponding radius of fuel, which is the LEM fuel penetration length, can be calculated as:

$$r_{fuel} = \left(\frac{3V_{fuel}}{2\pi(1-\cos\alpha)} \right)^{1/3}. \tag{3.7}$$

Fuel vapor is added to all cells on the LEM domain with a radius lower or equal to r_{fuel}. The second step is determining the fuel mass that each LEM cell receives. The volume of the LEM cell is the defining factor in determining the mass of each cell:

$$m_{ev,i}^{LEM} = m_{ev}^{CFD} \frac{V_{ev,i}^{LEM}}{\sum V_{ev,i}^{LEM}}. \tag{3.8}$$

The described method does not guarantee that the fuel vapor mass remains under the saturation level in each cell. However, this limit did not cause any issues in the simulations.

The allocated mass in each cell is calculated, followed by merging the existing and newly introduced quantities in each cell marked as a fuel receiver. Merging applies to temperature, mass fractions, and densities using a constant volume process. Equation (3.9) applies to ϕ where $\phi_i = \{Y_{i,s}, T_i\}$, ϕ^{old} denotes the scalars before adding the fuel vapor and ϕ^{add} the scalar to add:

$$\phi_i^{new} = \frac{\phi_i^{old} m_i^{old} + \phi_i^{add} m_i^{add}}{m_i^{old} + m_i^{add}}, \tag{3.9}$$

and for the density ρ:

$$\rho_i^{new} = \rho_i^{old} + \rho_i^{add} \frac{V_i^{add}}{V_i^{old}}. \tag{3.10}$$

The addition of vapor fuel to the LEM cells under a constant volume assumption leads to undesirable changes in the local pressure of the cells where the injection occurred. The Split Operator Strategy is utilized to enforce a uniform pressure on the LEM that matches the CFD target pressure.

3.1.4 Large scale mixing

The modeling of large-scale 3D motions, such as tumble and swirl in engines, within a one-dimensional domain is essential. These large scale motions are not represented by the eddy-sampling described above. Failing to account explicitly for these motions might lead to unphysical fuel-air mixing representation on the LEM domain which is essential for, e.g., ignition. In the case of continuous fuel injection, the fuel accumulates and the mixture fraction increases solely in the center of the domain. Such concentration can significantly reduce the chances of creating ignitable stoichiometric regions, thereby hindering fuel ignition. Therefore, when including the large-scale motions, several ignitable pockets with lower mixture fraction values are created. In addition, the distribution of the fuel regions increases the impact of the small eddies and diffusion to create ignitable regions. It is then essential to retain the large-scale motions in the LEM simulation. The large-scale movements are described by three quantities (eddy size, length, and occurrence time) similar to the small eddies. Modeling these three quantities is different for the large-scale motions since they are generated by other physics, namely, the movement of the piston and the incoming airflow from the inlet port. The length of the large-scale motions has been selected to equal half of the combustion chamber's bore; this length ensures the fuel distribution to different parts of the chamber, corresponding to the two sides of the LEM line. The time scale of these motions is determined based on the following scaling:

$$\tau_{le} = \theta \frac{v_N}{l_c}, \tag{3.11}$$

where θ refers to a mixing time constant that describes the effects of the combustion chamber geometry on the large-motion events times, which was fixed to unity. v_N refers to the spray's velocity influencing the large-scale motion, and l_c is the engine cylinder length scale. The number of large-scale movements occurring on one engine cycle is calculated at the start of the simulation by:

$$N_{le} = \frac{\tau_{ec}}{\tau_{le}}, \tag{3.12}$$

where τ_{ec} characterizes the time required for one engine cycle. The occurrence times are independently sampled based on a uniform distribution of occurrence time during one engine cycle. Finally, the position of the large eddies is sampled uniformly across the LEM line.

3.1.5 Mapping variables

An often used strategy to speed up combustion simulations involves advancing transport equations for representative independent variables, rather than for each major and intermediate species. This approach is similar to the one used in RIF simulations [30, 74, 94], which employ the mixture fraction, the scalar dissipation rate χ and the progress variable. In RILEM, while Z and c remains in use, χ is not used as a conditionning parameter. It is rather a result of the resolved turbulence on the LEM line.

3.1.5.1 Mixture Fraction Z

The mixture fraction Z is a fundamental concept in non-premixed and partially premixed combustion modeling. It quantifies the extent of mixing between the fuel and oxidizer streams, providing a measure of the local composition of the mixture. Z is evaluated differently in CFD and LEM. In CFD, it is solved as a transport equation for the mean mixture fraction $\tilde{Z}$ and its variance $\widetilde{Z''^2}$. On the LEM side, it is evaluated based on the Bilger formulation [95], a robust method for calculating mixture fractions in combustion systems. The Bilger mixture fraction is computed as follows:

$$Z = \frac{\zeta - \zeta_o}{\zeta_F - \zeta_o}, \tag{3.13}$$

where ζ represents a conserved scalar, specifically the mass fraction derived from the elemental mass fractions of carbon (C), hydrogen (H), and oxygen (O) present in the system. The formulation assumes that these elements are conserved during the reaction process. ζ_o and ζ_F represent the conserved scalar values in the oxidizer and fuel, respectively. These values are used to normalize ζ such that Z ranges from 0 to 1, where $Z = 0$ corresponds to pure oxidizer and $Z = 1$ corresponds to pure fuel.

$$\zeta = \sum_{k=1}^{n_{el}} \gamma_k \xi_k = \gamma_C \xi_C + \gamma_H \xi_H + \gamma_O \xi_O + \gamma_N \xi_N, \tag{3.14}$$

where n_{el} denotes the number of elements, γ_k are the weighting coefficients, and ξ_k are the elemental mass fractions of element k. The weighting coefficients γ_k are selected to ensure that ζ remains a conserved scalar during the combustion process. This means that ζ is affected only by the mixing of the fuel and oxidizer streams and not by chemical reactions. The selection of these coefficients is based on the stoichiometry of the fuel and oxidizer and can significantly influence the calculated mixture fraction. This approach is particularly advantageous for LEM, as it allows for the quantification of Z in each LEM cell based on the solution of the advanced 1D zero Mach number equations for species.

3.1.5.2 Combustion progress variable c

The combustion progress variable c is a reactive scalar that describes the chemical state of the gas mixture. As outlined in [14], c is defined by the following equation:

$$c = \frac{\psi - \psi_u}{\psi_b - \psi_u}, \tag{3.15}$$

where ψ denotes the reactive scalar (or combination of reactive scalars) utilized in the definition of the progress variable, ψ_u and ψ_b are the unburnt and the burnt values of the reactive scalar ψ, respectively. ψ_u and ψ_b are utilized to normalize ψ, resulting in $c = 0$ corresponding to an unburnt mixture and $c = 1$ indicating a burnt mixture. The source term of the combustion progress variable $\dot{c}$ reflects the rate at which the progress variable c develops. In LEM, $\dot{c}$ provides the chemical/combustion closure for the CFD. It is defined based on the following equation:

$$\dot{c} = \frac{1}{(\psi_b - \psi_u)} \frac{\mathrm{d}\psi}{\mathrm{d}t}, \tag{3.16}$$

where the rate of change of ψ, $\frac{\mathrm{d}\psi}{\mathrm{d}t}$, is given by

$$\frac{\mathrm{d}\psi}{\mathrm{d}t} = \frac{W_\psi \mathcal{R}[\psi]}{\rho}, \tag{3.17}$$

and $\mathcal{R}[\psi]$ denotes the net production rate of ψ and W_ψ the molecular weight of species ψ. Both c and $\dot{c}$ can be evaluated in each LEM cell after advancing the 1d zero Mach number equations of species.

3.2 SSALEM

A Spherical Stand-Alone LEM (SSALEM) was developed for debugging purposes and extensive parameter investigations. SSALEM was also used as a testing platform before proceeding to the CFD-LEM coupling. In a pre-processing step, a reacting CFD simulation was run using the Well Stirred Reactor model (WSR) to extract driving parameters for the SSALEM. A standard 1D slider-crank model has been used to calculate the combustion chamber volume as a function of the engine speed. The SSALEM framework is represented in Figure 3.7. In SSALEM, the coupling between the CFD and LEM is unidirectional, with influence being exclusively from CFD to LEM. This setup lacks the reciprocal feedback of LEM to CFD. In this framework, ignition on the LEM was triggered by the enforced pressure trace extracted from the WSR simulation. Illustrative examples of the SSALEM simulation are showcased in the result chapter. However, to fully benefit from the LEM capabilities, in particular LEM's combustion closure, it is required to have a two-way coupling between LEM and CFD. Such an approach would create a feedback loop from LEM to CFD that will influence the CFD parameters, such as the rate of evaporation of the fuel and the turbulence level due to the increase in temperature.

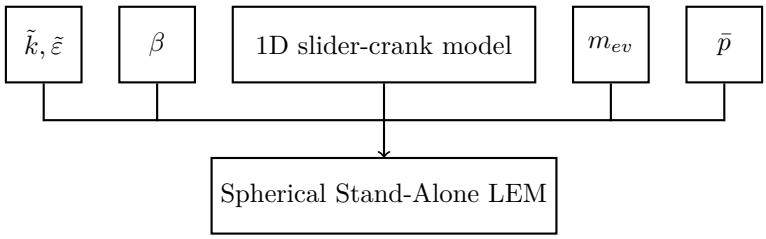

Figure 3.7: *Spherical Stand-Alone LEM framework*

3.3 RILEM

The implementation of the CFD in 3D and the LEM in 1D makes the coupling between the two sides a complex task. The LEM provides a distribution of the reactive scalars in 1D physical space after solving the 1D zero Mach number equations. These reactive scalars need to be communicated with the 3D CFD domain in a meaningful way. For that, RILEM adopts a similar coupling concept to the RIF approach [29, 30, 74]. The RILEM coupling scheme between CFD and LEM is represented in Figure 3.8. After applying Reynolds averaging on equation (2.28) for Z and c. Mixture fraction is represented by two equations, namely the mixture fraction mean $\tilde{Z}$ (3.18) and the mixture fraction variance $\widetilde{Z''^2}$ (3.19), meanwhile the development of the progress variable c is described uniquely with the transport equation of the mean $\tilde{c}$.

$$\frac{\partial \bar{\rho}\tilde{Z}}{\partial t} + \nabla \cdot [\bar{\rho}\tilde{\mathbf{u}}\tilde{Z}] = \nabla \cdot [\frac{\mu_t}{Sc_t}\nabla \tilde{Z}] + \widetilde{\dot{\rho}_s}, \tag{3.18}$$

$$\frac{\partial \bar{\rho}\widetilde{Z''^2}}{\partial t} + \nabla \cdot [\bar{\rho}\tilde{\mathbf{u}}\widetilde{Z''^2}] = \nabla \cdot [\frac{\mu}{Sc_t}\nabla \widetilde{Z''^2}] + \frac{2\mu_t}{Sc_t}(\nabla \tilde{Z})^2 - \bar{\rho}\tilde{\chi}, \tag{3.19}$$

where

$$\tilde{\chi} = C_\chi \frac{\varepsilon}{k}\widetilde{Z''^2}, \tag{3.20}$$

and $C_\chi = 2.0$.

$$\frac{\partial \bar{\rho}\tilde{c}}{\partial t} + \nabla \cdot [\bar{\rho}\tilde{\mathbf{u}}\tilde{c}] = \nabla \cdot [\frac{\mu_t}{Sc_t}\nabla \tilde{c}] + \bar{\rho}\tilde{\dot{c}}, \tag{3.21}$$

where $\dot{c}$ represents the progress variable source term previously discussed in subsection 3.1.5.2.

First, equations (3.18), (3.19) and (3.21) are advanced togather with (2.38), (2.39) and (2.40) togather on the CFD side. Second, the LEM solution is mapped from physical space to the CFD. This is realized by first conditioning the reactive scalars ϕ to Z and c. The chosen resolution was 200 equally sized bins in the Z direction and 100 bins in c, where a *bin* refers to a specific interval in a Z or c space. The result of this mapping is a matrix of reactive scalars Z, c space referred to as *solution table*.

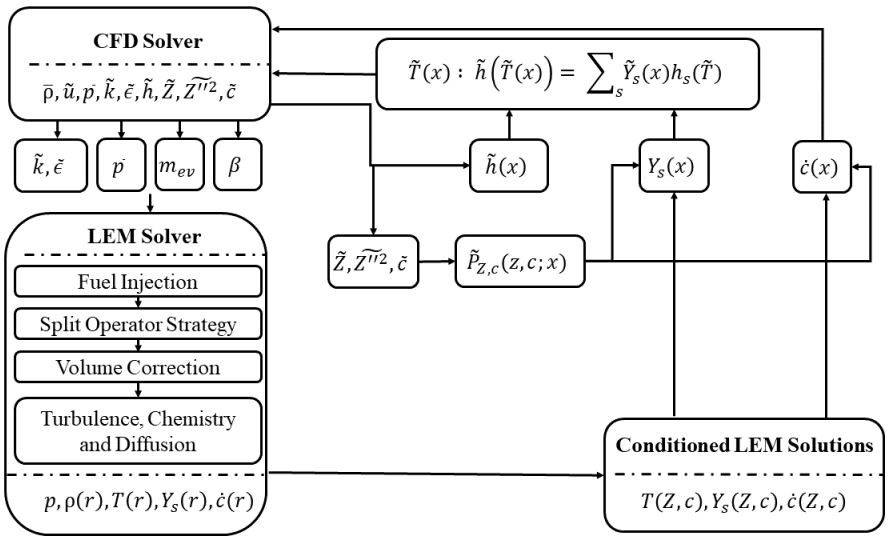

Figure 3.8: *RILEM configuration*

The next step is integrating the reactive scalars in each CFD cell using a joint Probability Density Function (PDF) for Z and c, which is constructed based on $\tilde{Z}$, $\widetilde{Z''^2}$ and $\tilde{c}$ as described in the following:

$$\widetilde{\phi_k} = \int_0^1 \int_0^1 \widetilde{P}_{Z,c}(Z_k, c_k) \phi^{LEM}(Z, c) dZ dc. \tag{3.22}$$

Statistical independence is assumed between Z and c, simplifying the problem by decomposing the joint PDFs to two independent PDFs:

$$P_{Z,c}(Z, c) = P_Z(Z; \widetilde{Z}, \widetilde{Z''^2}) P_c(c; \widetilde{c}). \tag{3.23}$$

3.3.0.1 Mixture fraction PDF

The solution of transport equations for mean and variance of the mixture fraction provides in each CFD cell two values defining the presumed β-PDF for Z:

$$P_Z(Z; \widetilde{Z}, \widetilde{Z''^2}) = \frac{\Gamma(\gamma)}{\Gamma(\alpha)\Gamma(\beta)} Z^{\alpha-1}(1-Z)^{\beta-1}, \tag{3.24}$$

where Γ is the usual gamma function defined as:

$$\Gamma(t) = \int_0^\infty t^{x-1} e^{-t} dt, \tag{3.25}$$

and α, β and γ are three coefficients defined as:

$$\gamma = \frac{\tilde{Z}(1-\tilde{Z})}{\widetilde{Z''^2}}, \qquad \alpha = \gamma \tilde{Z}, \qquad \beta = \gamma(1-\tilde{Z}). \tag{3.26}$$

The following figure displays different shapes of the β function depending on the mean and the variance:

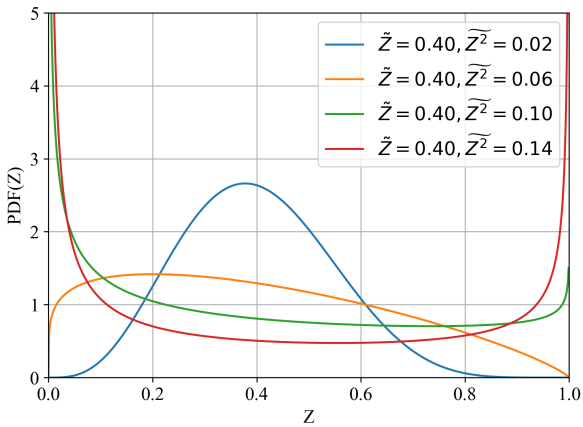

Figure 3.9: *β Function distribution*

3.3.0.2 Combustion progress variable PDF

Different PDFs for the combustion progress variable c were tested in this work. Initially, due to the lack of a predictive transport equation for the combustion progress variable variance $\widetilde{c''^2}$, a PDF defined based uniquely on the mean $\tilde{c}$ was utilized. This PDF is referred to as the *step function* and it is first used in this work. It is represented in Figure 3.10 with different values of $\tilde{c}$ and is defined as follows:

$$P_c(c;\tilde{c}) = \begin{cases} \frac{1-\tilde{c}}{\tilde{c}} & 0 \leq c \leq \tilde{c} \\ \frac{\tilde{c}}{1-\tilde{c}} & \tilde{c} \leq c \leq 1 \end{cases} \tag{3.27}$$

A β-PDF can likewise be used for the combustion progress variable. For that, a definition for $\widetilde{c''^2}$ is required. An algebraic formulation for $\widetilde{c''^2}$ is utilized based on Pierce and Moin [96], which was developed in an LES context. The variance was calculated in [96] based on the LES filter width as

$$\bar{\rho}\,\widetilde{c''^2} = C_\psi\,\bar{\rho}\,\Delta^2\,|\nabla\tilde{c}|^2\,, \tag{3.28}$$

where C_ψ denotes a constant chosen as $\frac{1}{12}$ and Δ the filter width. Since the current setup use a RANS framework, the filter width Δ is replaced with the integral length scale l_t, which is calculated via

$$l_t = \sqrt{\frac{3}{2}}\frac{c_\mu}{Sc_t}\frac{\tilde{k}^{3/2}}{\tilde{\varepsilon}}. \tag{3.29}$$

where the turbulent Schmidt number Sc_t is equal to 0.7.

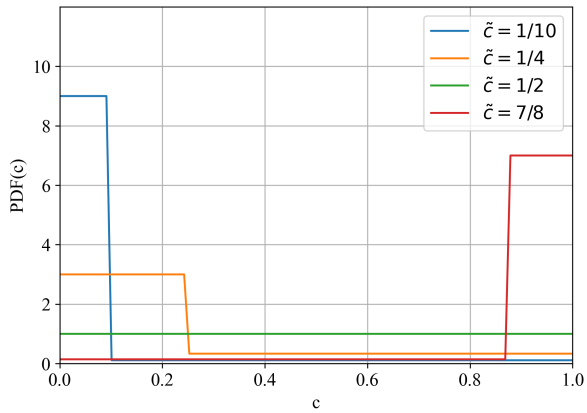

Figure 3.10: *Step Function distribution*

The algebraic equation for $\widetilde{c''^2}$ will instead be based on :

$$\bar{\rho}\widetilde{c''^2} = C_c \bar{\rho} l_t^2 |\nabla \tilde{c}|^2. \tag{3.30}$$

3.3.1 Thermal equation of state (Temperature evaluation)

The calculation of the mean temperature $\tilde{T}$ in each CFD cell can be calculated in two distinct ways: The first involves conditioning of the LEM temperature distribution T_{LEM} on Z, c space, and integrating it in each CFD cell using PDFs with equation (3.22). This temperature is named $\tilde{T}_{map}$. The second methodology utilized the caloric equation of state

$$\tilde{h}_k(\tilde{T}) = \sum_{s=1}^{N} \tilde{Y}_{s,k}(t) h_s(\tilde{T}), \tag{3.31}$$

with

$$h_s(T) = \Delta h_s^0 + \int_{T^0}^{T} c_{p,s}(T) dT, \tag{3.32}$$

to iterate a temperature. Here, h_s denotes the mass-specific enthalpy values of the species s, Δh_s^0 the standard heat of formation, and $c_{p,s}$ the mass specific heat capacity at constant pressure. We name this temperature $\tilde{T}_{it}$. Mean values for the mass fractions are obtained again via conditioned mass fraction values from the LEM integrated to provide mean values according to (3.22). If volume coupling is utilized, the second approach is preferred. This is due to the presence of source terms in the energy equation, which account for heat effects such as the latent heat of evaporation or wall heat losses. These effects are modeled in the LEM with an enthalpy defect, necessitating the use of the energy equation solution for better consideration of these effects on the CFD temperature. However, in the case of pressure coupling, the heat effects are an intrinsic part of the pressure trace communicated to the LEM at each time step. Consequently, the combustion process within the LEM

inherently accounts for the heat loss effect with no additional modeling. This implies that both strategies, i.e., $\tilde{T}_{map}$ and $\tilde{T}_{it}$, yield comparable results in the context of pressure coupling.

3.4 MRILEM

LEM solves the 1D zero Mach number equations for species mass and enthalpy in physical space and time. Conditioning the LEM solution to Z and c from a single LEM line in most cases does not fill the complete Z, c space of the solution table which causes erroneous PDF integration. For a statistically stationary problem, advancing the LEM for a long time can solve the problem, but for unsteady combustion processes in engines other approaches needs to be employed. The suggested solution to the problem here is to advance multiple LEMs, each representing a single realization of a turbulent flow. This is simply realized by changing the initial random number seed leading to a different eddy sequence on each LEM. Each LEM line builds a solution table corresponding to the eddy sequence of that line. The data from all tables is used to generate a global representative table that the CFD will utilize to calculate the mean values of the reactive scalars. This approach is called MRILEM and is sketched in Figure 3.11. The averaging

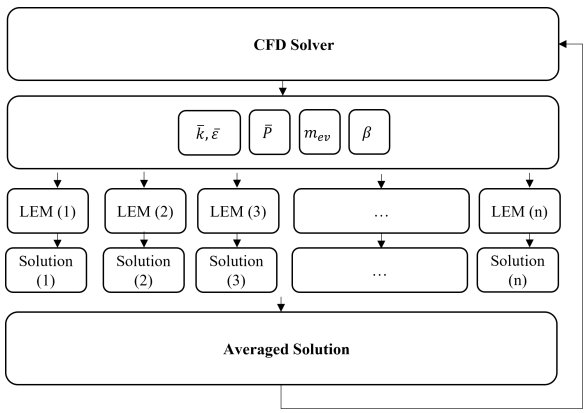

Figure 3.11: *Multiple RILEMs configuration*

process between the tables for Z, c bins which are filled by more than one LEM line is done via simple ensemble averaging:

$$\phi_{ij} = \frac{\sum_{k=1}^{n_{ij}} \phi_{ij}^{k}}{n_{ij}}, \tag{3.33}$$

where n_{ij} denotes the total number of hits for bin (Z_i, c_j) in the solution table with $i \in [1, n_Z]$, $j \in [1, n_c]$, and n_Z and n_c denote the number of bins in Z space and c space, respectively.

A series of simulations have been done using the MRILEM approach with 16 LEMs. The findings showed that the utilization of 16 lines appears to sufficiently fill the solution table. In principle, increasing the number of LEMs should improve the overall statistical fidelity of the approach and should guarantee an always completely filled table. However, for reasons of computation cost we suggest the following add-on to mRILEM which has proven to handle remaining holes in the solution table in a reasonable way:

1. Built the solution table from a computationally feasible number of LEM lines,
2. Scaling the $P_Z(Z)$ and $P_c(c)$ of the turbulent scalars,
3. Persistence of the LEM solution.

The motivation behind this method is to avoid integrating over empty Z and c bins with no solution, which requires a scaling of the PDF to ensure the normalizing condition on the available Z, c space.

3.4.1 PDF scaling

Calculating a mean value of a turbulent scalar conditioned on Z and c spaces is done by utilizing the following formula that assumes statistical independence of Z and c:

$$\widetilde{\phi} = \int_0^1 \int_0^1 \widetilde{P}_Z(Z; \widetilde{Z}_k, \widetilde{Z}_k^2) \widetilde{P}_c(c; \widetilde{c}_k) \phi^{\mathrm{LEM}}(Z, c)\, dZ\, dc \tag{3.34}$$

However, the holes in the solution tables of ϕ represent discontinuities in the distribution of the turbulent scalar in Z and c spaces, implying that utilizing an integral formulation as depicted in (3.34) to express the mean value calculation is incorrect . Equation (3.34) will instead be expressed as a discrete sum as described in the following:

$$\widetilde{\phi}_k = \sum_{i \in N(z)} \sum_{j \in N(c)} \widetilde{P}_Z(Z_i; \widetilde{Z_k}, \widetilde{Z}_k^{"2}) \widetilde{P}_c(c_j; \widetilde{c_k}) \phi^{LEM}(Z_i, c_j) \Delta Z \Delta c, \tag{3.35}$$

where $N(z)$ and $N(c)$ correspond to the set of solutions found in the corresponding solution space. $\widetilde{Z_k}, \widetilde{Z}_k^{"2}$, and $\widetilde{c_k}$ represent respectively the mean of the mixture fraction, the variance of the mixture fraction and the mean of the progress variable in a CFD cell k.

Scaling the PDFs is essentially utilizing the following formula:

$$\widetilde{\phi} = \sum_{i \in N(Z)} \sum_{j \in N(c)} \widetilde{P^*}_Z(Z_i; \widetilde{Z}_k, \widetilde{Z}_k^2) \widetilde{P^*}_c(c_j; \widetilde{c}_k) \phi^{\mathrm{LEM}}(Z_i, c_j) \Delta Z \Delta c, \tag{3.36}$$

where $\widetilde{P^*}_Z$ and $\widetilde{P^*}_c$ are the scaled PDFs expressed as the following:

$$\widetilde{P^*}_Z(Z_i) = \frac{\widetilde{P}_Z(Z_i)}{\sum_{i \in N(Z)} \widetilde{P}_Z(Z_i)}, \quad \widetilde{P^*}_c(c_j) = \frac{\widetilde{P}_c(c_j)}{\sum_{j \in N(c)} \widetilde{P}_c(c_j)} \tag{3.37}$$

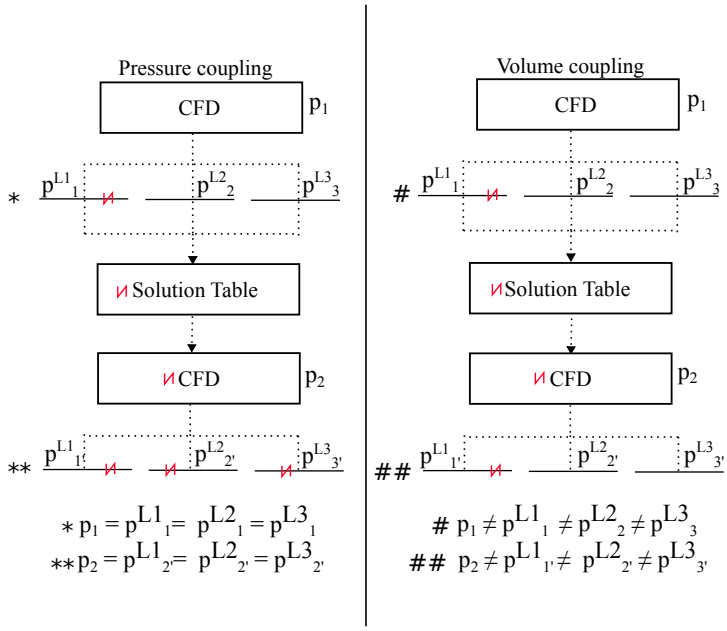

Figure 3.12: *Representation of the pressure coupling effect on the LEM lines*

3.4.2 Persistence of the LEM solution

The persistence approach implies maintaining the encountered values of the reactive scalar ϕ of previous time steps. If a new result is found, the old value gets overwritten by the new one. The persistence approach aids with minimizing the effect of the scaling method, namely bringing $\sum_{j\in N(c)} \widetilde{P}_c(c_j)$ and $\sum_{j\in N(Z)} \widetilde{P}_Z(Z_i)$ closer to unity, especially at the start of the simulation where the solution tables are still empty.

3.4.3 Pressure coupling effect on solution population

The pressure coupling not only intrinsically transmits the CFD heat effects via the pressure trace to the LEM without additional modeling, but also introduces a feature that facilitates intercommunication among the LEM lines in a physically reasonable way. Figure 3.12 illustrates three LEM lines (L_1, L_2, and L_3) advancing in parallel under both pressure-coupled and volume-coupled scenarios

In the case of employing pressure coupling, combustion in one or multiple cells within a line (marked by the red symbol on L_1) causes combustion information to be transmitted to the solution table and integrated into the CFD cells. This integration increases the pressure trace due to the presence of combusted mass fractions in the solution table. Consequently, the increased pressure trace is communicated to all advanced LEM lines via CFD-LEM pressure coupling, accelerating the combustion process in the other LEM lines, L_2 and L_3, which initially did not experience combustion.

In the volume-coupled scenario, a sequence of events similar to the pressure-coupled case occurs, involving combustion on L_1, conditioning of combusted mass fractions, integration of mass species, and a resultant pressure increase in the CFD due to mapping of combusted species. However, this combusted information is barely communicated to the other LEM lines, i.e., L_2 and L_3, in the subsequent time step. This limited communication occurs because the CFD volume does not convey information about the chemical state of the chamber. Consequently, combustion tends to persist primarily in L_1, where it initially occurred. While combustion might eventually occur in other lines due to the formation of stoichiometric pockets, it does not result from increased pressure in L_1 due to CFD-enforced pressure changes.

Additionally, one could argue that communication exists between the LEM lines in both the pressure- and volume-coupling scenarios, driven by the vapor mass generated and transferred from the CFD to the LEM. Mapping a combusted solution into the CFD results in a temperature increase, which in turn generates more vapor mass. While this indicates that volume coupling also facilitates intercommunication between the lines, it does not constitute a thermochemical interconnection that would accelerate the formation of combustible LEM cells.

4 Results

4.1 Paper I: Application of SSALEM on a part-load heavy-duty engine

A single-cylinder metal research engine with a 15.8:1 compression ratio corresponding to a Volvo 13L six-cylinder heavy-duty truck engine was selected to test the pressure-coupled SSALEM. This case has previously been investigated in [59] for both part- and full-loads.

4.1.1 Boundary conditions

Table 4.1 summarizes the operating conditions for the part- and full-load case. In this paper, however, only the part load case was selected.

	Part-Load	**Full-Load**
Initial pressure (bar)	1.69	4.25
Initial temperature (K)	395	404
Composition (% mass)		
O_2	16.5	18.9
N_2	75.3	75.8
CO_2	5.97	3.91
H_2O	2.26	1.48
Injected mass (mg)	13	47
Start of injection	3.1° bTDC	4.7° bTDC
End of injection	3.3° aTDC	16.7° aTDC

Table 4.1: Operating conditions for part-load and full-load cases

Based on the SSALEM framework represented in section 3.7, the input parameters that advance the SSALEM were generated from a reacting WSR simulation.

4.1.2 Summary of the results

Figures 4.1 represent temperature state and species mass fractions on the LEM line in physical space. The illustration of the LEM line in physical space was possible by plotting the center positions of the LEM cell. These Figures also represent the small and large-scale eddies on the line. At CAD = 358, combustion appears to start immediately, as indicated by an increase in temperature and Y_{CO} within the middle of the LEM domain. By CAD = 360, Y_{CO} begins to decline as the temperature peaks, indicating near-complete combustion. Additionally, this stage marks the appearance of another flame on the left side, which is

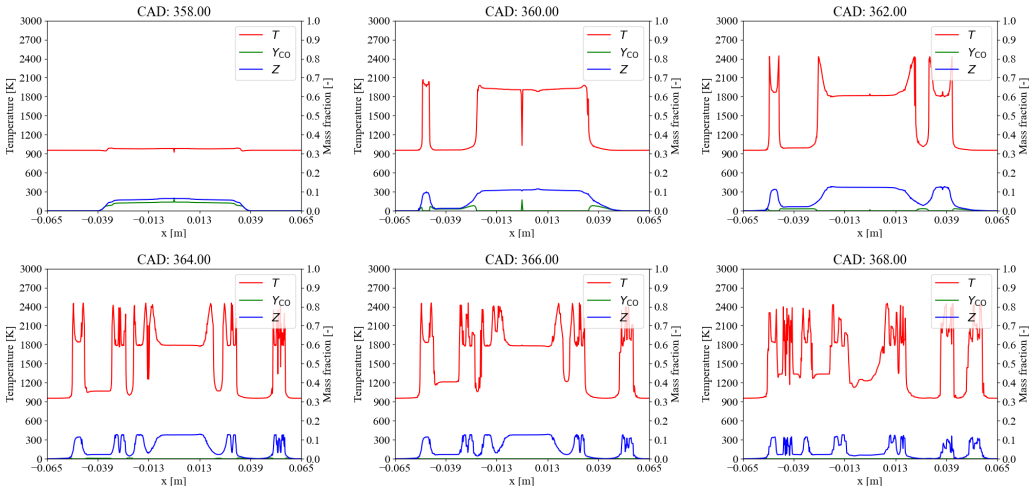

Figure 4.1: *Development of fuel injection, turbulence, and combustion process of SSALEM over time*

a manifestation of a large eddy event that affects the scalar distribution along the line. By CAD = 362, the line has experienced another large eddy event. Furthermore, the high-temperature region starts to exhibit a U-shape, implying higher temperatures at the extremities of the composition, which align with stoichiometric conditions. At later stages of the simulation, CO oxidation is complete, and the domain continues to experience both large and small eddy events interacting with the composition, steering the mixture towards a more homogeneous state.

4.2 Paper II: MRILEM for a part- and full-load heavy-duty engine

In this investigation, the pressure-coupled RILEM was applied to both the part and full-load Volvo heavy-duty engine case by advancing multiple lines in parallel with different eddy placements.

4.2.1 Computational domain and boundary conditions

The operating conditions of this case were presented in the previous section in table 4.1, and the computational domain of the CFD domain is displayed in Figure 4.2.

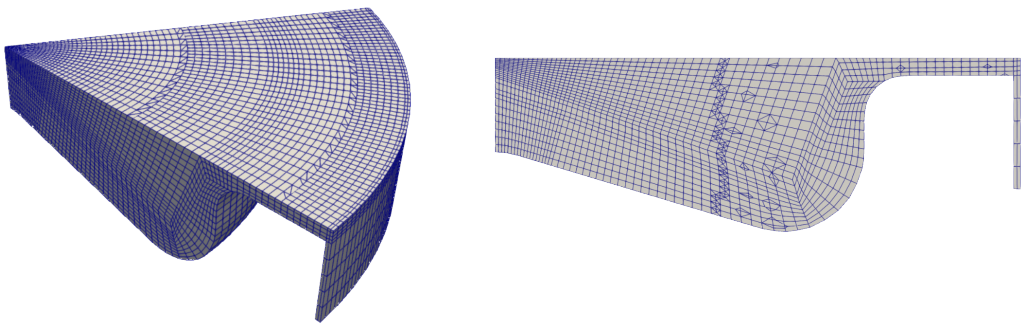

Figure 4.2: *Representation of the computational domain. Sector mesh (left) and slice in (y) direction (right)*

4.2.2 Summary of the results

Advancing RILEM required utilizing LEM in a representative way. This requires simulating the process happening on the CFD, i.e., fuel injection, molecular diffusion, heat conduction, and turbulent advection, also on the LEM line. These effects are advanced on the LEM line at each time step based on input parameters from the CFD, as described in Figure 3.8. Unlike SSALEM, RILEM introduces a feedback mechanism from LEM to CFD. In this setup, the turbulent reactive scalars, conditioned by the LEM, directly influence the CFD solution through the mapped species and consequently affect the pressure trace. This, again, affects how the combustion occurs on the LEM via the pressure coupling scheme and the amount of vapor generated on the CFD, creating a cyclic interaction between CFD and LEM. This step was realized in previous investigations utilizing only one pressure-coupled LEM to the CFD. In scenarios where the PDFs were not scaled, the pressure trace was underestimated, as it did not accurately represent the combustion process when compared to experiments. This discrepancy arose due to an incomplete solution in the Z and c space, where only a few bins were filled. However, scaling the PDFs and utilizing one LEM line led to a dramatic overestimation of the solution was dramatically over-estimated. The observed discrepancies are also due to inconsistencies

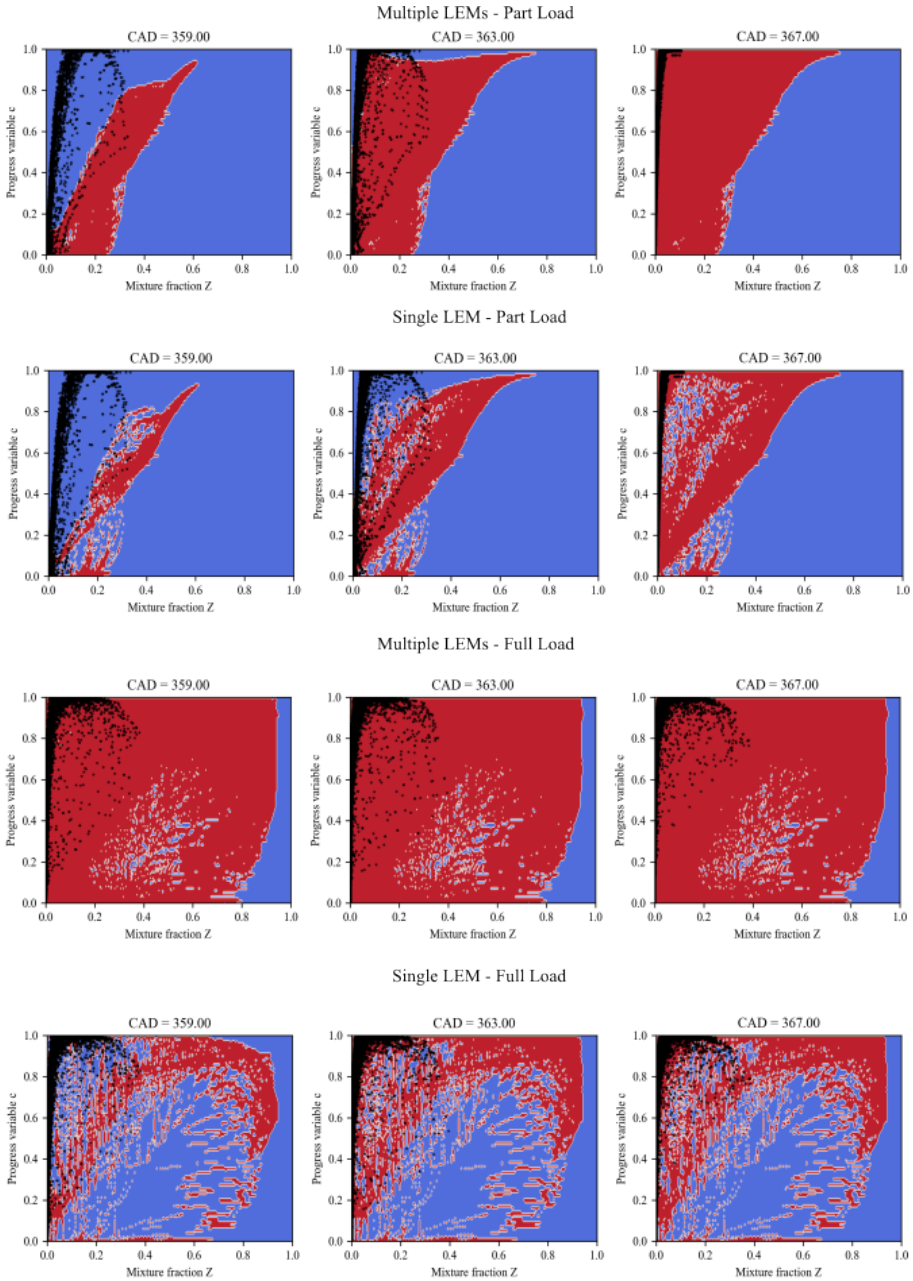

Figure 4.3: *Representation of CFD statistics $(\tilde{Z}, \tilde{c})$ depicted in black dots, and the LEM discovered solutions by advancing multiple LEM lines (above) and a single LEM line (below) portrayed by the red dots in (Z, c)-space, at CAD = 359.00 (left), 363.00 (center), 367.00 (right)*

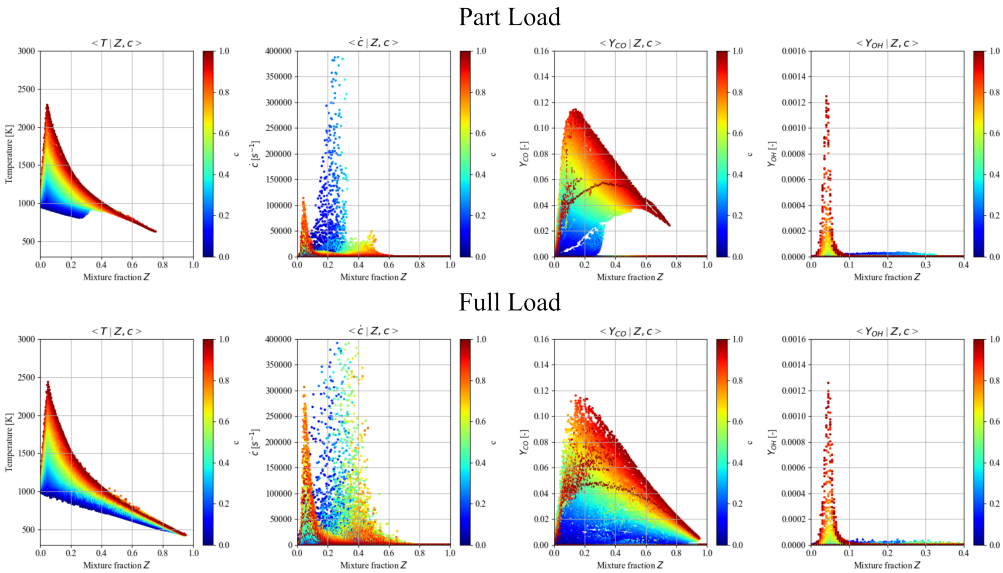

Figure 4.4: *LEM statistics of Temperature,* $\dot{c}$*,* CO*, and* OH *conditioned on mixture fraction* Z *and progress variable* c

between the LEM solution and the CFD, as only one "discovered" scenario from the LEM advancement is highlighted. The solution that provided the best results was advancing multiple LEM lines as described in chapter 3, scaling the PDFs, and maintaining the LEM solution history so that the LEM solution is filled as much as possible. The PDF scaling required a PDF for c that stretches over the entire space, rather than a Dirac function. For that the step function described in Figure 3.10 was utilized. This strategy yielded better statistics for both the part- and full-load cases, as depicted in Figure 4.3.

The black dots in Figure 4.3 describe the $\tilde{Z}$ and $\tilde{c}$ values extracted from the CFD solution at a given CAD value. A mismatch could be noticed between the black dots (CFD statistics) and the red dots (LEM solution) at the initial stages of the part-load case for high c values. Three reasons were suggested to explain this effect: i) Mismatch in fuel-air mixing between CFD and LEM. ii) The development of $\tilde{c}$ on CFD is primarily dependent on the mapping of $\dot{c}$ from the LEM to the CFD, suggesting that LEM possesses combustion information ahead of the CFD, particularly during the initial stages of combustion. iii) Difference in the CFD and LEM PDF shapes at early combustion stages for the part-load case.

As described in chapter 3, the CFD utilizes the LEM statistics displayed in Figure 4.4, in combination with the presumed β-PDF for Z and a step function for c to integrate the species mass fractions and $\dot{c}$ in every computational cell. Combining the CFD mapped species and the solution of the enthalpy transport equation, the temperature field is iterated using equations (3.32) in each CFD cell depicted by Figure 4.5. The mapping of species from LEM and temperature iteration also gives the possibility of calculating the

average pressure on the CFD domain and the heat release produced at each time step. These quantities have been compared to experiments, results obtained with an MZWM model, and results from a previous volume-coupled RILEM simulation and are depicted in Figures 4.6 and 4.7.

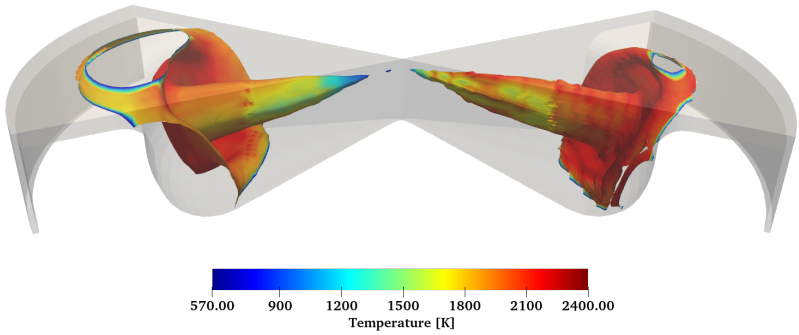

Figure 4.5: *Representation of the CFD temperature profile for part-load (left) and full-load (right) at CAD = 363.00*

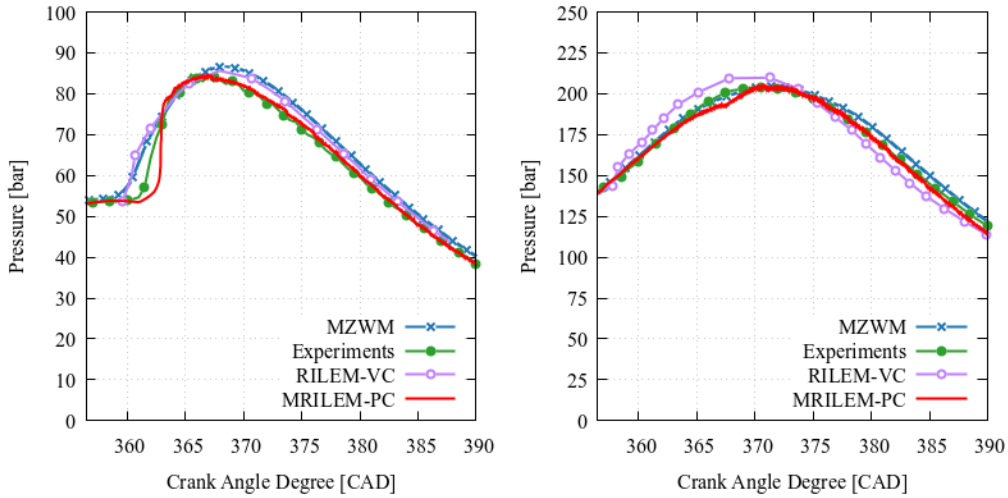

Figure 4.6: *Comparison of pressure trace generated from pressure-coupled MRILEM, MZWM, experiments, and volume-coupled RILEM for Part-Load (left) and Full-load (right).*

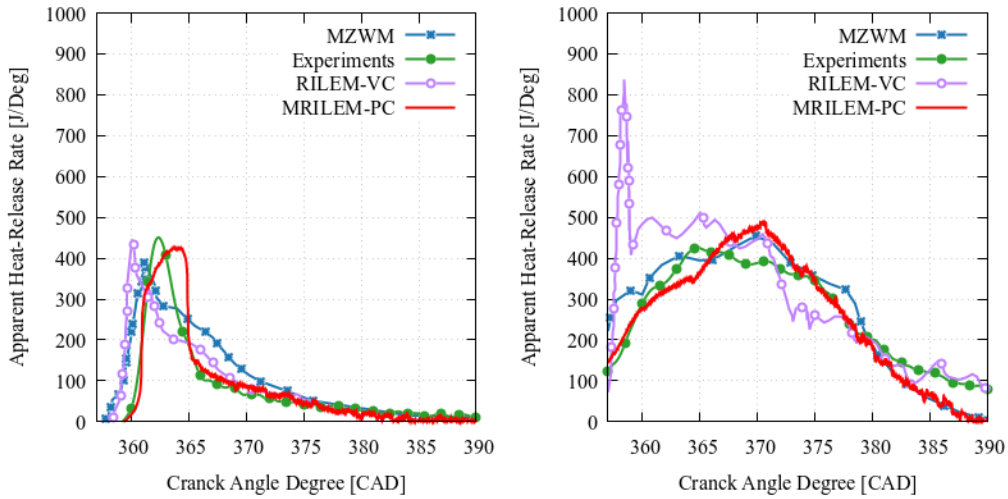

Figure 4.7: *Comparison of the apparent heat release rate generated from pressure-coupled MRILEM, MZWM, experiments, and volume-coupled RILEM for Part-Load (left) and Full-load (right).*

4.3 Paper III: Investigation of Ducted Fuel Injection (DFI) with MRILEM

In this study, RILEM was employed to model the combustion process within a ducted fuel injection (DFI) system across two different ambient temperatures. The DFI strategy enhances combustion efficiency by maintaining a high equivalence ratio, generating a premixed air-fuel mixture, and reducing soot formation. This reduction in soot mitigates the NOx-soot trade-off, enabling Exhaust Gas Recirculation (EGR) to decrease NOx emissions. Additionally, the ejector effect created by DFI improves air entrainment and fuel-air mixing, further enhancing combustion efficiency and reducing emissions.

RILEM was advanced with multiple LEM lines in parallel while decomposing the lines into two turbulence regions, i.e. one for the duct region and one for the remaining. This technique introduces a novel approach to utilizing the LEM line, made possible by the ability of LEM to represent turbulent reactive scalars in physical space. This investigation highlighted how variations in turbulence intensity within the duct region affect the combustion process.

4.3.1 Computational domain and Boundary conditions

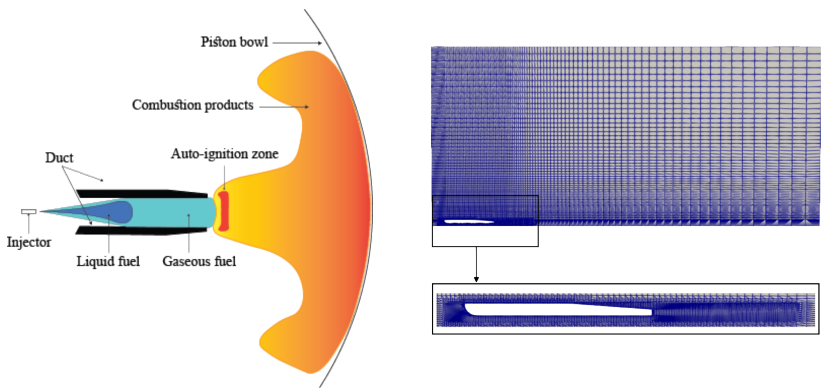

Figure 4.8: *Sketch of Ducted Fuel Injection (left) and representation of the computational domain (right)*

Two ambient temperatures were simulated for the ducted fuel injection using RILEM, i.e., T=900 K and T=1000 K. Figure 4.8 depicts the computational domain, which is a constant volume chamber. In this investigation, the duct was implemented on the LEM line as two adiabatic walls, that are removed when the fuel exits the duct region on the CFD. Due to the fact that the LEM line represents the complete combustion chamber with a 1D line in physical space, modeling ducted fuel injection with LEM and its impact on combustion was rather straight forward. The duct's impact on turbulence is quite substantial, implying the necessity of implementing this process on the LEM line. In

principle, this was realized by separating the LEM line into regions of different turbulence level as described in Figure 4.9. The shear layer region utilized the usual turbulence parameters, i.e., $\tilde{k}$ and $\tilde{\varepsilon}$ as in previous RILEM simulations. On the other hand, the driving turbulent quantities driving the LEM modell in the duct region have been chosen

$$k_D = C_D * \tilde{k}_{max}, \qquad \varepsilon_D = C_D * \tilde{\varepsilon}_{max}, \tag{4.1}$$

where $\tilde{k}_{max}^{\text{CFD}}$ and $\tilde{\varepsilon}_{max}^{\text{CFD}}$ represent the peak values of $\tilde{k}$ and $\tilde{\varepsilon}$ over the complete CFD domain at the corresponding time step, and C_D denotes a turbulence calibration constant. Additionally, eddies that land on the LEM duct walls are not implemented. The results presented were extracted from RILEM simulations realized with $C_D = 10\%$, except where mentioned otherwise.

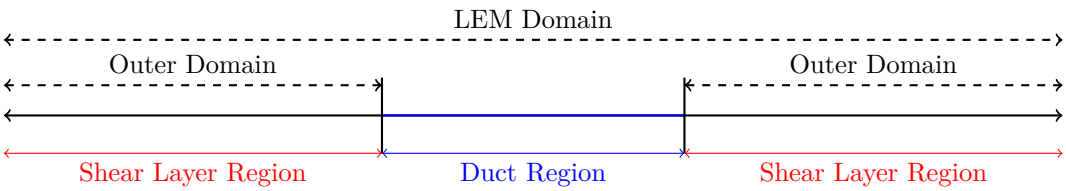

Figure 4.9: *Representation of the duct implementation in the LEM's physical space: Depiction of duct walls and the different turbulence regions.*

4.3.2 Summary of the results

The impact of the duct on the LEM line is illustrated by comparing the solution statistics before and after duct removal, as shown in Figures 4.10 and 4.11. The pre-duct solution statistics correspond to the LEM at t = 0.013ms, just before the duct is removed, while the post-duct solution statistics correspond to the LEM at t=4ms. Figure 4.10 shows that statistics for stoichiometric mixture fractions in their burnt state are unavailable. This absence is due to the duct presence in the LEM, which prevents the mixture from becoming too lean, thereby preventing the formation of stoichiometric values. The duct effectively creates a partially premixed mixture, thereby enhancing combustion efficiency.

The heat release rates were extracted from the RILEM simulations and compared to the MZWM in Figure 4.12. The heat release rates for RILEM features a peak at the initial stages of the simulation compared to MZWM model. This occurs due to the PDF scaling strategy as the discovery of a local hot spot combined with PDF scaling can lead to an overestimation of the ignition process, i.e., the heat generated from the mapped species. The RILEM curves decrease after t = 0.8 ms to values lower than MZWM. The curves reach an alignment in the later stages of the simulation, which might be due to accurate statistics from RILEM on Z, c, where PDF scaling effects are minimized.

The ignition delay time and lift-off lengths were also extracted from RILEM simulations and compared to MZWM and experiments as represented in Figure 4.13. RILEM was

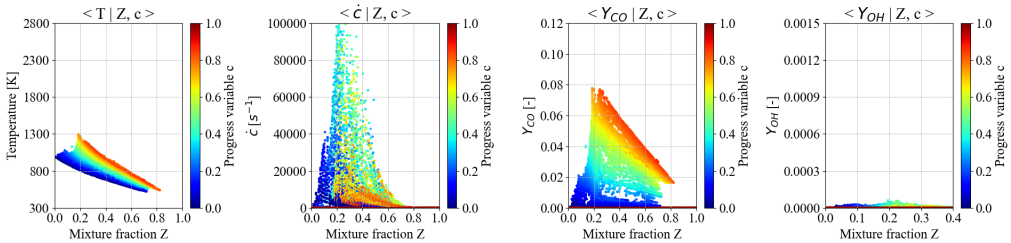

Figure 4.10: *Representation of LEM statistics pre-duct removal at T=1000 K*

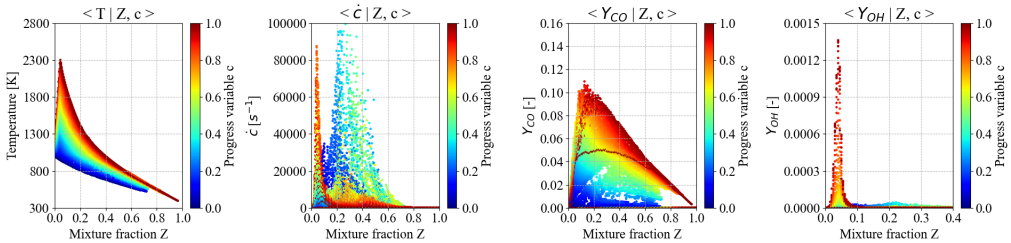

Figure 4.11: *Representation of LEM statistics post-duct removal at T=1000 K*

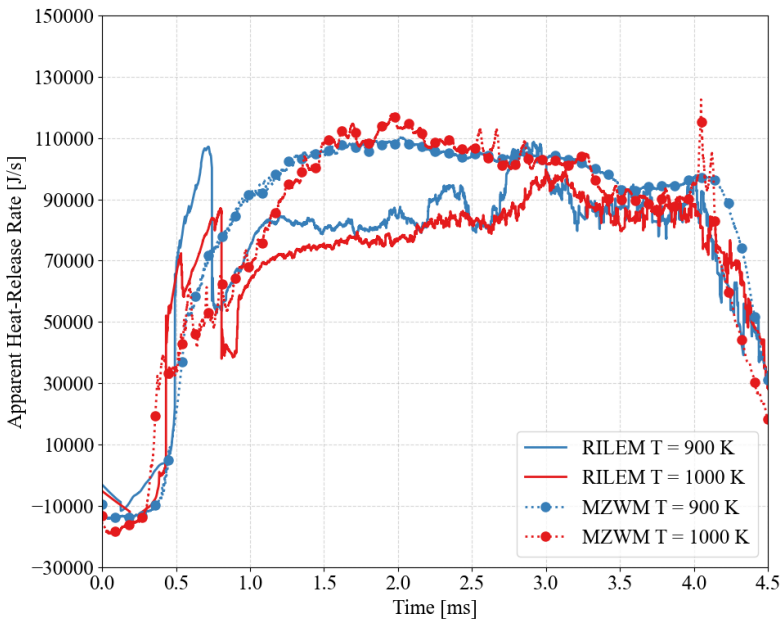

Figure 4.12: *Comparison of Apparent heat release rates extracted from RILEM and MZWM at T= 900 and 1000 K*

advanced with $C_D = 100\%$ and $C_D = 10\%$ describing intense and moderate turbulence levels on the duct, respectively. In case of intense turbulence, the ignition delay time is overestimated compared to experiments and MZWM for $T = 900$ K. This occurs because high turbulence causes the mixing time scale to become lower than the chemical time scale, making it challenging for chemical reactions to progress. This is similar to the effect generated by a high scalar dissipation rate that can cause delayed combustion or even extinction events in intense cases. Decreasing C_D to 10% led to a more realistic RILEM ignition delay time. The effect of high turbulence impacted only the case of $T = 900$ K. For $T = 1000$ K, turbulence did not have a major role, as the ignition delay is similar to that of the moderate turbulence level, implying that the chemistry had a higher impact in this case. The underestimation of lift-off length in simulations compared to experimental data can be attributed to two factors: First, the inaccurate modeling of heat transfer to duct walls, particularly when utilizing adiabatic duct walls on the LEM ignores heat losses. Second, the PDF scaling issue in RILEM models. With limited data, the early stages of simulation can lead to overestimated OH mass fractions, resulting in an underestimated lift-off length in the RILEM model.

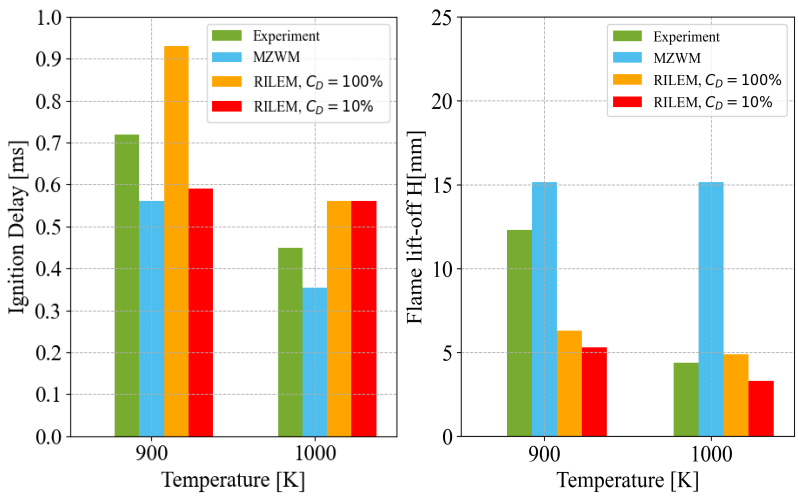

Figure 4.13: *Comparison of ignition delay times (left) and mean lift-off lengths (right) between RILEM, MZWM, and experiment for T =900 and 1000 K*

4.4 Paper IV: Investigation of Turbulence Chemistry Interaction and Evaluation of Progress Variable definition and PDFs using MRILEM

In this investigation, the RILEM was applied to a 2.34 l diesel engine, where two progress variable definitions were tested, i.e., O_2 and h_{298}. In addition, two PDFs for the progress variable were assessed, namely the step- and the β-PDF constructed using a variance defined through a RANS adaptation of the LES Pierce and Moin algebraic definition [96]. In this investigation, RILEM was advanced using two distinct approaches: First, RILEM was advanced with multiple LEM lines on the fly (MRILEM), which were initialized using a solution table derived from the results of homogeneous reactors to minimize the effects of scaling. Second, RILEM was advanced using a pre-tabulated LEM solution table (Tabulated RILEM), generated from a previous MRILEM run, incorporating molecular diffusion, heat conduction, and turbulence advection.

4.4.1 Computational mesh and Boundary conditions

The simulation were realized for the cases described in table 4.2

Table 4.2: Operating conditions of the simulated cases

Parameter	Values
In-cylinder Temperatures (K)	800, 900, 1000
Oxygen Concentration	15%
Density (kg/m^3)	22.8
Injection Pressure (bar)	1500

The computational grid was generated with an automatic mesh generation code in Lib-ICE. The mesh is displayed in Figure 4.14.

4.4.2 Summary of the results

The MRILEM featured 10 LEM lines, which were advanced in parallel, each with a distinct initial random seed number that resulted in different eddy sequences on each line. However, the solution table was not initialized empty as in Paper II [97]. The solution table was initialized based on advancing homogeneous reactors and conditioning the results in Z, c space. Only the $\dot{c}$ solution table was left empty for the LEMs to populate. Utilizing different progress variable definitions yielded apparent differences in the Z, c conditioned reactive scalars as depicted in Figure 4.15.

The advancement of the LEM lines revealed a discrepancy between the solution generated from the advanced LEMs and the initial homogeneous reactor solution. This difference aligns with expectations, given LEM's ability to account for turbulence-chemistry interactions, molecular diffusion and heat conduction. However, this specific outcome has not

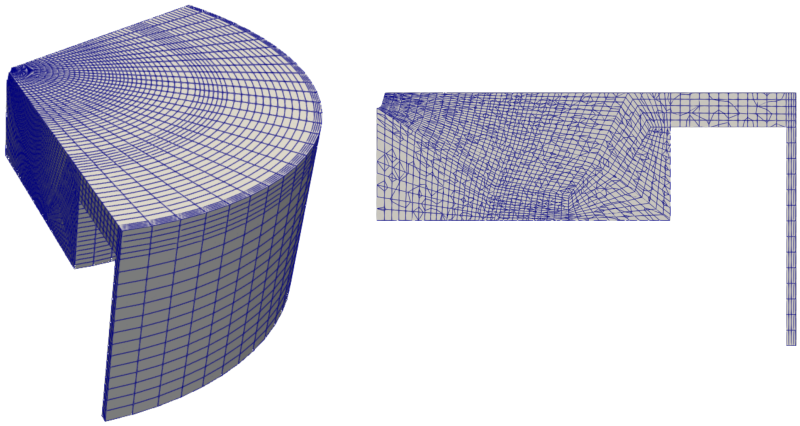

Figure 4.14: *Computational domain. Sector mesh (left) and slice in (y) direction (right)*

been quantitatively demonstrated until now. Figure 4.16 shows the comparison between the LEM solution and the initial 0D solutions for $\psi = O_2$ and $\psi = h_{298}$ in both mixture fraction and progress variable space for temperature, CO and OH mass fractions.

The LEM solution table allows the mapping of turbulent reactive scalars in each computational cell using PDFs for Z and c. Integrating in Z space was always realized using the β-PDF. However, for c space, the choice is not evident. As previously mentioned, the step function presented in 3.10 and a β function for c were compared in this work.

This investigation also uncovered interesting features in the temporal evolution of the $\dot{c}$ solution table. As depicted in Figure 4.17, $\dot{c}$ demonstrates variability over time, which is primarily influenced by the turbulence level along the line. This indicates that $\dot{c}$ solution table is influenced not only by Z and c but also by the turbulence intensity. Moreover, the distribution of $\dot{c}$ within the Z, c space varies significantly depending on the specific PDF used to condition the reactive scalars.

Figure 4.18 illustrates the evolution of the heat release rate for MRILEM and TRILEM, employing both step and β-PDFs for $\psi = O_2$ and $\psi = h_{298}$. The figure shows that there is no significant difference in the results when using $\psi = O_2$ versus $\psi = h_{298}$. However, a notable distinction is observed between MRILEM and TRILEM. For $T = 900$ K, and to a lesser extent for $T = 1000$ K, MRILEM's heat release rate initially depicts a peak, resulting in an overestimation when compared to experimental data. This behavior is similar to what was observed in Figure 4.12, where a pronounced peak was also detected. The peak arises due to PDF scaling when integrating $\dot{c}$, as all species mass fractions for MRILEM are prepopulated with solutions from a homogeneous reactor. The scaling technique leads to a sudden increase in $\tilde{c}$ within the CFD. Consequently, burnt mass fractions are mapped to the CFD cells from the discovered solution table, which triggers a high rate of heat release. This phenomenon is significantly mitigated when using TRILEM,

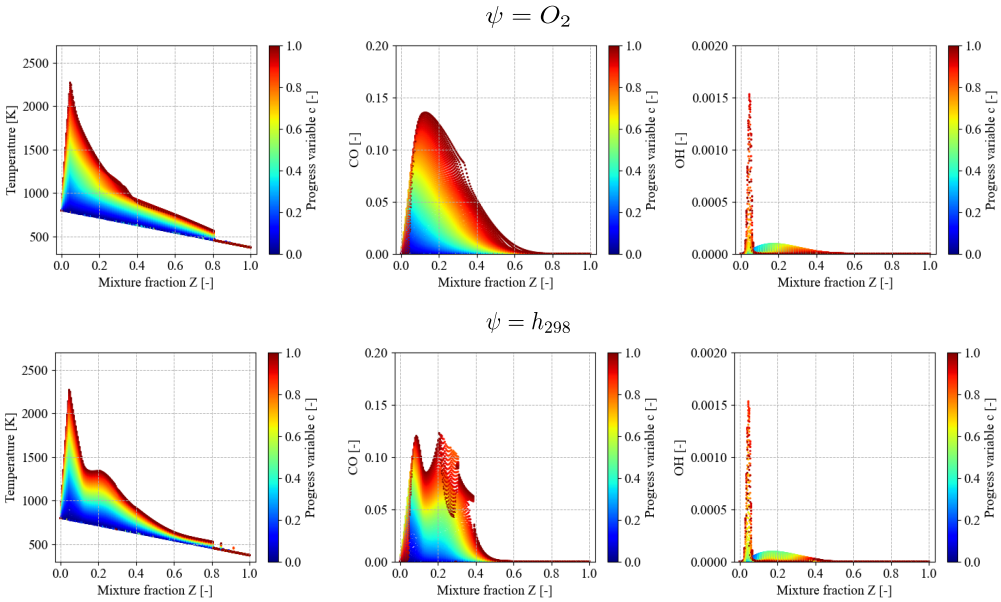

Figure 4.15: *Representation of Z, c conditioned reactive scalar statistics for T=900 K; Temperature,* CO *and* OH *$\psi = O_2$ (above) and $\psi = h_{298}$ (below).*

where $\dot{c}$ is prepopulated in the Z, c space. This results in a reduction of PDF scaling effects on $\dot{c}$, leading to a gradual increase of $\tilde{c}$ in the CFD. This implies a progressive evolution of species mass fractions over time in each computational cell, rather than a rapid jump from unburnt to burnt states for species mass fractions.

Figure 4.19 displays ignition delays and the mean lift-off lengths for MRILEM and TRILEM. A first remark is the difference in ignition delay times between utilizing step PDF with $\psi = h_{298}$ and all the other configurations. The MRILEM simulations are realized with pre-computed statistics except for $\dot{c}$, implying that LEM controls the ignition process on CFD, i.e. the ignition delay time. When analyzing the first column (CAD = 2.00) and the top two rows of Figure 4.17, it is apparent that the $\dot{c}$ statistics for the step function combined with $\psi = h_{298}$ in unburnt regions are low compared to other configurations. This means that the ignition process for this specific configuration will be slower, implying a larger ignition delay time. Similarly for the mean lift-off lengths, utilizing the step function yields the best results. However, in this case, both c definitions provide good results with experiments. The reason is how the step function distribution differs from the β function. The step function takes into consideration the solution in the entire c space, in extreme cases, as $\tilde{c} = 0.5$, the distribution in c space is strictly uniform. However, for a β function, in case of low variance, the distribution peaks around the mean.

In the case of TRILEM, the statistics of all the reactive scalars, including $\dot{c}$, are populated

and are not being updated. The difference between the results is due to the interactions of the PDFs with the $\dot{c}$ distribution in Z, c space. Utilizing the step function will ensure a population of $\dot{c}$ that includes burnt regions of $\dot{c}$ in c space, contrary to the utilization of β function, where in case of low regions of $\tilde{c}$, only lower values of $\dot{c}$ will be considered as the β function gives almost no weight to the tails, whereas the step function does. Here, the mean lift-off lengths are calculated based on OH mass fractions that are prepopulated considering turbulence advection, molecular diffusion, and heat conduction. In addition to this, the pre-calculation of $\dot{c}$, contributes to a more gradual development of $\tilde{c}$ on the CFD, which leads to less sudden combustion and a more comprehensive development of OH mass fraction, leading to a better prediction of mean lift-off lengths.

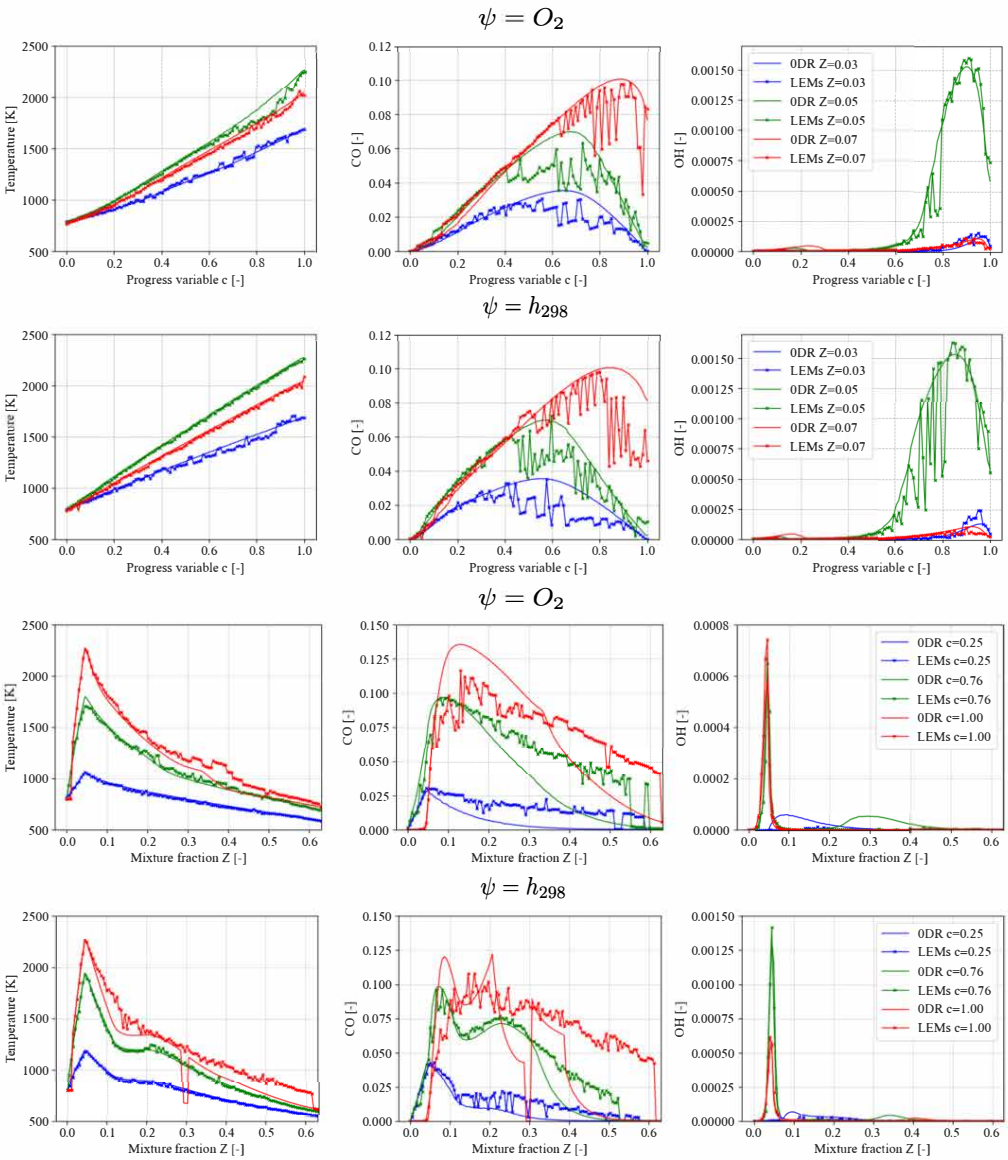

Figure 4.16: *Comparison of Z, c conditioned reactive scalars generated from 0D reactors and LEM lines at $T = 900$ K. Representation in progress variable space (above) and mixture fraction space (below) for $\psi = O_2$ and $\psi = h_{298}$. The conditioned scalars are temperature,* CO*, and* OH *mass fractions.*

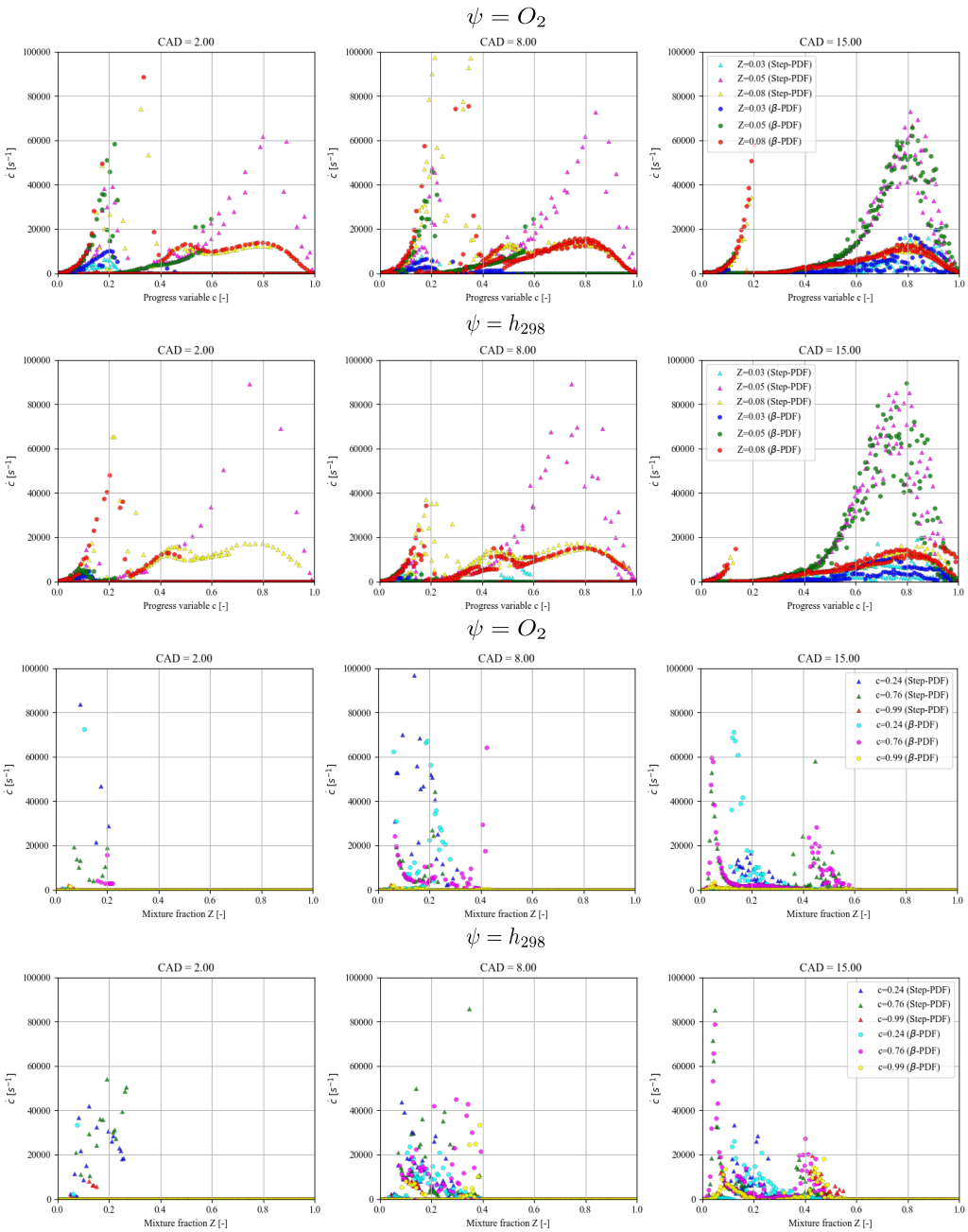

Figure 4.17: *Representation of the statistics of $\dot{c}$ conditioned on Z, c in time for $T = 900$ K. Representation in progress variable space (above) and mixture fraction space (below) for ψ = O_2 and $\psi = h_{298}$.*

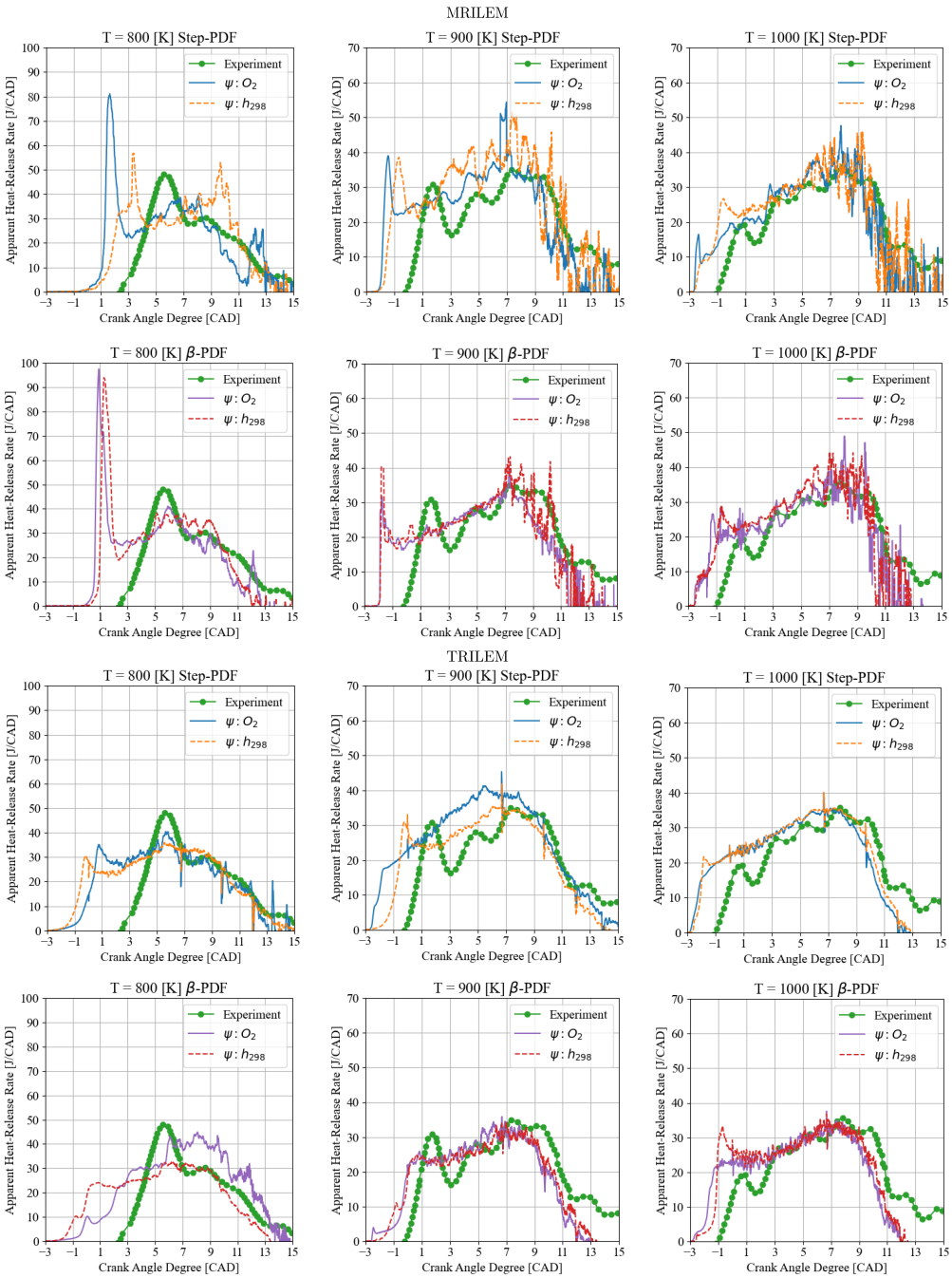

Figure 4.18: *Comparison of Apparent Heat Release Rate between MRILEM and TRILEM for for* $\psi = \mathrm{O}_2$ *and* $\psi = h_{298}$ *when utilizing step- and* β*-PDF for c*

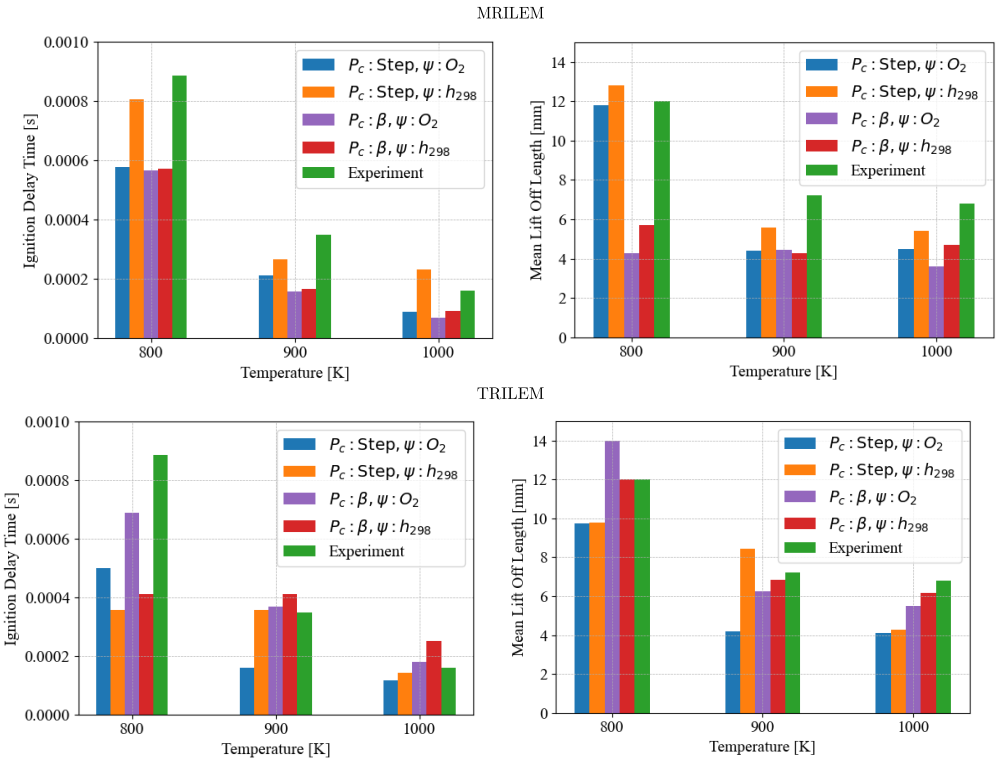

Figure 4.19: *Representation of ignition delay times (left) and mean lift-off lengths (right) for MRILEM (above) and TRILEM (below)*

5 Conclusion and Outlook

This PhD work aimed to further develop and utilize the Linear Eddy Model (LEM) as a versatile mode and regime-independent combustion model for engine simulations. Specifically, this objective was achieved through multiple extensions and applications of the recently presented RILEM approach.

The transport equations for mass, momentum, and energy were advanced on the CFD side in an Eulerian framework and a spray model was advanced in a Lagrangian framework. The driving parameters extracted from the CFD are communicated to the LEM in an interactive representative way. The molecular diffusion and heat conduction processes on LEM are advanced by solving the 1D zero Mach number equations. In addition, LEM features turbulent advection via spherical triplet maps and chemistry advancement in each LEM cell. RILEM utilizes a coupling technique that is similar to RIF via conditioned solutions in mixture fraction and progress variable space with a presumed PDF approach. Both RILEM and RIF advance the transport equation of the mean and variance of the mixture fraction Z on the CFD side, which allows to construct a presumed β-PDF for Z in each computational cell of the CFD domain. Despite these similarities, RILEM and RIF differ significantly in their treatment of other variables and equations. RILEM advances the zero Mach number transport equations of species and heat in physical space, which corresponds here to the configuration of the complete combustion chamber. This method allows to directly simulate how turbulence interacts with chemistry in the combustion chamber. On the other hand, RIF (or flamelet models in general) solve the transport equations in mixture fraction space (or a canonical flame configuration) aiming at a universal or parameterised representation of flame structures. Therefore, RIF is agnostic to the CFD geometry, which allows for a broad application across different types of flames. Another distinct difference is in the use of the scalar dissipation rate χ. RIF employs χ as a conditioning variable, which affects modeling of turbulence and its interaction with chemical reactions. For RILEM, χ is a result of the simulation, i.e. eddies interacting with the turbulent scalars on the line in physical space.

The RILEM formulation was upgraded to a pressure-coupling approach instead of the previously employed volume-coupling. This advancement enabled the consideration of thermal effects, including latent heat of evaporation and wall heat losses on the LEM line without explicit modeling. These effects were previously modeled via an enthalpy defect on the LEM side. This innovation was part of the development phase of a spherical stand-alone LEM, where the (Z, c) conditioning technique was formulated alongside a split operator strategy. This ensured that the new coupling approach was fully compatible with the constant LEM pressure condition within the LEM framework.

To address the issue of empty bins in the LEM solution table, the RILEM model was enhanced to incorporate the advancement of multiple pressure coupled lines called MRILEM. In MRILEM, each line receives the same CFD driving parameters, but with different eddy histories on each line. The pressure coupling combined with the multiple LEM

approach provided a better statistical description of the turbulent reactive scalars in addition leading to a more accurate description of the combustion process within the combustion chamber. A significant advantage of this method is the facilitation of combustion information exchange between the lines, enhancing the combustion process on CFD. This is different from the volume coupling technique, where this interactive exchange is absent.

The pressure-coupled MRILEM was investigated with different cases. First, a heavy-duty engine case for both part- and full-load, where the pressure trace and the heat-release were evaluated against experiments and the results of the MZWM. Here, the effect of utilizing multiple pressure-coupled lines was demonstrated in a heavy-duty engine case. In addition, a novel step-PDF for the progress variable c defined uniquely on its mean value was introduced. This function is defined on the entirety of the progress variable space, allowing scalability in case of insufficient statistics in Z, c space. The pressure-coupled MRILEM was also employed to simulate the combustion process for a Ducted Fuel Injection (DFI) case, where the duct was implemented physically on the line by two adiabatic walls and different turbulent regions on the line, i.e. large turbulence for the duct region and normal turbulence for the rest. Lift-off lengths, ignition delay times, and heat release were compared to experiments and MZWM.

Finally, MRILEM was advanced with a pre-initialized solution for the turbulent reactive scalars, except $\dot{c}$, from unsteady homogeneous reactors, instead of empty LEM solution tables to minimize effects due to PDF scaling. In this investigation, two progress variable definitions, i.e., $\psi = O_2$ and h_{298}, were tested along with two PDFs for c, i.e. step- and β-PDF. Ignition delay times and lift-off lengths of each variation were compared to experiments. A dependence of $\dot{c}$ was identified, which may indicate that another dimension is required for $\dot{c}$ in addition to Z and c. Moreover, a tabulated RILEM approach, i.e. TRILEM, was introduced in this study, where the CFD is advanced with a reactive scalars solution table, in this case including $\dot{c}$, from previous MRILEM realization. TRILEM was also tested for the two progress variable definitions and PDFs. TRILEM showcased improvements in heat release, lift-off lengths, ignition delay, and computational time compared to regular MRILEM.

The main outcome of this work is a version of the recently introduces RILEM approach for simulating engine combustion, which has reached a somewhat mature and usable state and is ready for further investigations. This has been achieved via several substantial extensions improving statistical fidelity, robustness, predictive capabilities and computational efficiency.

5.1 Future work

Spark ignition Premixed H_2 with RILEM

Recently, there has been growing interest in using zero-emission fuels such as hydrogen as alternatives to fossil fuels. As previously mentioned, the LEM is a regime and mode-independent combustion model, able to simulate premixed, partially premixed,

and diffusion flames. Additionally, LEM can easily incorporate differential diffusion effects, which might be relevant for hydrogen combustion simulations. To achieve this, LEM can be employed in a representative interactive manner to simulate a premixed charge injected in the combustion chamber and interacting with tumble and shear eddies. Certain modifications are required to simulate this configuration, specifically incorporating the spark on the LEM line and advancing LEM transport equations that account for multicomponent diffusion, namely the Stephan-Maxwell equations.

Mapping acceleration

The mapping procedure of turbulent scalars from LEM to CFD could be accelerated by constructing a solution table of integrated turbulent scalars in a space discretized based on the mean and variance of Z and c. This method can potentially improve efficiency by eliminating the need for real-time generation of presumed β-PDFs and replacing the integration step with a simple linear interpolation. However, it introduces a limitation that prevents the exploration of the effects of various PDF types on the combustion process.

LES based RILEM

Another potential area of study involves examining the impact of coupling a CFD model that utilizes LES as a turbulence model with LEM in a way that represents the entire combustion chamber, similar to the RANS-RILEM approach investigated in this PhD work. In RANS, the entire inertial subrange is modeled, where the LEM advances eddies with sizes varying between the integral length l_t scale and the Kolmogorov scale η. In contrast, LES resolves turbulence structures from the integral scale l_t to the filter width Δ directly through the mesh, leaving the smaller structures, from the filter width Δ to the Kolmogorov length η, to be modeled. This method could be evaluated against LES-LEM or supergrid LES-LEM approaches [48].

Bibliography

[1] Our World in Data. *Energy consumption by source and country*. https://ourworldindata.org/grapher/energy-consumption-by-source-and-country?stackMode=absolute. [Online; accessed 29 March 2023]. 2021.

[2] J. Perlin. *A forest journey: The story of wood and civilization*. The Countryman Press, 2005.

[3] S. Verhelst and T. Wallner. "Hydrogen-fueled internal combustion engines". In: *Progress in energy and combustion science* 35.6 (2009), pp. 490–527.

[4] R. Lindsey and E. Dlugokencky. "Climate change: atmospheric carbon dioxide. 2020". In: *ClimateWatch Magazine. Disponível em:< https://www. climate. gov/news-features/understandingclimate/climate-change-atmospheric-carbondioxide#:˜: text= The% 20global% 20average% 20atmospheric% 20carbon, least% 20the* 2 (2020).

[5] S. C. Doney et al. "Impact of anthropogenic atmospheric nitrogen and sulfur deposition on ocean acidification and the inorganic carbon system". In: *Proceedings of the National Academy of Sciences* 104.37 (2007), pp. 14580–14585.

[6] L. K. Weaver. "Carbon monoxide poisoning". In: *Critical care clinics* 15.2 (1999), pp. 297–317.

[7] R. O. McClellan, T. W. Hesterberg, and J. C. Wall. "Evaluation of carcinogenic hazard of diesel engine exhaust needs to consider revolutionary changes in diesel technology". In: *Regulatory Toxicology and Pharmacology* 63.2 (2012), pp. 225–258.

[8] T. Bourdrel et al. "Cardiovascular effects of air pollution". In: *Archives of cardiovascular diseases* 110.11 (2017), pp. 634–642.

[9] S. Bouckaert et al. "Net zero by 2050: A roadmap for the global energy sector". In: (2021).

[10] EDGAR/JRC. *Global carbon dioxide emissions from 1970 to 2021, by sector (in million metric tons of carbon dioxide) [Graph]*. Sept. 2022. URL: https://www.statista.com/statistics/276480/world-carbon-dioxide-emissions-by-sector/ (visited on 08/01/2023).

[11] G. Goppelt. "Electrification by 2030-The OEMs' Plans". In: *ATZelectronics worldwide* 17.10 (2022), pp. 36–41.

[12] Aria Developpement Durable. *Explosion d'hydrogène dans une station-service*. 2023. URL: https://www.aria.developpement-durable.gouv.fr/accident/53772/.

[13] IEA. *Global final energy demand for trucks and buses by fuel in the Net Zero Scenario, 2000-2030*. Licence: CC BY 4.0. 2023. URL: https://www.iea.org/data-and-statistics/charts/global-final-energy-demand-for-trucks-and-buses-by-fuel-in-the-net-zero-scenario-2000-2030.

[14] N. Peters. *Turbulent combustion*. 2001.

[15] P. A. Libby, K. N. C. Bray, and J. B. Moss. "Effects of finite reaction rate and molecular transport in premixed turbulent combustion". In: *Combust. Flame* 34 (1979), pp. 285–301.

[16] F.E. Marble and J.E. Broadwell. "The coherent flame model for turbulent chemical reactions". In: (1977).

[17] D.B. Spalding. "Mixing and chemical reaction in steady confined turbulent flames". In: *Symposium (International) on combustion*. Vol. 13. 1. Elsevier. 1971, pp. 649–657.

[18] D.B. Spalding. “Development of the eddy-break-up model of turbulent combustion”. In: *Symposium (International) on Combustion*. Vol. 16. 1. Elsevier, 1977, pp. 1657–1663.
[19] T. Poinsot and D. Veynante. *Theoretical and numerical combustion*. RT Edwards, Inc., 2005.
[20] B.F. Magnussen and B.H. Hjertager. “On mathematical modeling of turbulent combustion with special emphasis on soot formation and combustion”. In: *Symposium (international) on Combustion*. Vol. 16. 1. Elsevier. 1977, pp. 719–729.
[21] A. Kösters et al. “RANS predictions of turbulent diffusion flames: comparison of a reactor and a flamelet combustion model to the well stirred approach”. In: *Combustion Theory and Modelling* 19.1 (2015), pp. 81–106.
[22] J. Chomiak. *Combustion: A Study in Theory, Fact, and Application*. cit. on p. 11. Abacus Press, 1990. ISBN: 9780856264535.
[23] S.B. Pope and Y.L. Chen. “The velocity-dissipation probability density function model for turbulent flows”. In: *Physics of Fluids A: Fluid Dynamics* 2.8 (1990), pp. 1437–1449.
[24] A.R. Kerstein. “Linear-eddy modeling of turbulent transport. II: Application to shear layer mixing”. In: *Combustion and Flame* 75.3-4 (1989), pp. 397–413.
[25] A.R. Kerstein. “Linear-eddy modeling of turbulent transport. Part 4. Structure of diffusion flames”. In: *Combustion Science and Technology* 81.1-3 (1992), pp. 75–96.
[26] H. Lehtiniemi et al. *Efficient 3-D CFD combustion modeling with transient flamelet models*. Tech. rep. SAE technical paper, 2008.
[27] J.A. Van Oijen and L.P.H De Goey. “Modelling of premixed laminar flames using flamelet-generated manifolds”. In: *Combustion Science and Technology* 161.1 (2000), pp. 113–137.
[28] J.A. Sethian. “Theory, algorithms, and applications of level set methods for propagating interfaces”. In: *Acta numerica* 5 (1996), pp. 309–395.
[29] H. Pitsch, H. Barths, and N. Peters. “Three-dimensional modeling of NO x and soot formation in DI-diesel engines using detailed chemistry based on the interactive flamelet approach”. In: *SAE transactions* (1996), pp. 2010–2024.
[30] G. D’Errico et al. “Comparison of well-mixed and multiple representative interactive flamelet approaches for diesel spray combustion modelling”. In: *Combustion Theory and Modelling* 18.1 (2014), pp. 65–88.
[31] A.Y. Klimenko. “Multicomponent diffusion of various admixtures in turbulent flow”. In: *Fluid dynamics* 25.3 (1990), pp. 327–334.
[32] A.R. Kerstein. “A linear-eddy model of turbulent scalar transport and mixing”. In: *Combustion Science and Technology* 60.4-6 (1988), pp. 391–421.
[33] A.R. Kerstein. “Linear-eddy modelling of turbulent transport. Part 3. Mixing and differential molecular diffusion in round jets”. In: *Journal of Fluid Mechanics* 216 (1990), pp. 411–435.
[34] A.R. Kerstein. “Linear-eddy modeling of turbulent transport. Part V: Geometry of scalar interfaces”. In: *Physics of Fluids A: Fluid Dynamics* 3.5 (1991), pp. 1110–1114.
[35] A.R. Kerstein. “Linear-eddy modelling of turbulent transport. Part 6. Microstructure of diffusive scalar mixing fields”. In: *Journal of Fluid Mechanics* 231 (1991), pp. 361–394.
[36] A.R. Kerstein. “Linear-eddy modelling of turbulent transport. Part 7. Finite-rate chemistry and multi-stream mixing”. In: *Journal of Fluid Mechanics* 240 (1992), pp. 289–313.

[37] VK. Chakravarthy and S. Menon. “Linear eddy simulations of Reynolds number and Schmidt number effects on turbulent scalar mixing”. In: *Physics of Fluids* 13.2 (2001), pp. 488–499.
[38] M.A. Cremer, P.A. McMurtry, and A.R. Kerstein. “Effects of turbulence length-scale distribution on scalar mixing in homogeneous turbulent flow”. In: *Physics of Fluids* 6.6 (1994), pp. 2143–2153.
[39] G.M. Goldin and S. Menon. “A comparison of scalar PDF turbulent combustion models”. In: *Combustion and Flame* 113.3 (1998), pp. 442–453.
[40] S.K. Krueger. “Linear eddy modeling of entrainment and mixing in stratus clouds”. In: *Journal of the atmospheric sciences* 50.18 (1993), pp. 3078–3090.
[41] S. Krueger, C. W. Su, and P.A. McMurtry. “Modeling entrainment and finescale mixing in cumulus clouds”. In: *Journal of the atmospheric sciences* 54.23 (1997), pp. 2697–2712.
[42] M. Oevermann, H. Schmidt, and A.R. Kerstein. “Investigation of autoignition under thermal stratification using linear eddy modeling”. In: *Combustion and Flame* 155.3 (2008), pp. 370–379.
[43] P.A. McMurthyand S. Menon and A.R. Kerstein. “A linear eddy sub-grid model for turbulent reacting flows: Application to hydrogen-air combustion”. In: *Symposium (International) on Combustion*. Vol. 24. 1. Elsevier. 1992, pp. 271–278.
[44] M. Koochesfahani and P.E. Dimotakis. “Mixing and chemical reactions in a turbulent liquid mixing layer”. In: *Journal of Fluid Mechanics* 170 (1986), pp. 83–112.
[45] S. Arshad et al. “A strategy for large-scale scalar advection in large eddy simulations that use the linear eddy sub-grid mixing model”. In: *International Journal of Numerical Methods for Heat & Fluid Flow* 28.10 (2018), pp. 2463–2479.
[46] S. Arshad et al. “Subgrid reaction-diffusion closure for large eddy simulations using the linear-eddy model”. In: *Flow, Turbulence and Combustion* 103 (2019), pp. 389–416.
[47] A.M. Menon. *Super-Grid Linear Eddy Model (SG-LEM): Efficient Mode-and Regime-Independent Combustion Closure for Large Eddy Simulation (LES)*. Chalmers Tekniska Hogskola (Sweden), 2022.
[48] A.M. Menon, M. Oevermann, and A.R. Kerstein. “A super-grid approach for LES combustion closure using the Linear Eddy Model”. In: *Combustion Theory and Modelling* (2023), pp. 1–28.
[49] R. Steeper et al. *Simulation of the effect of spatial fuel distribution using a linear-eddy model*. Tech. rep. SAE Technical Paper, 2007.
[50] A. Babajimopoulos et al. “A fully coupled computational fluid dynamics and multi-zone model with detailed chemical kinetics for the simulation of premixed charge compression ignition engines”. In: *International Journal of Engine Research* 6.5 (2005), pp. 497–512.
[51] F. Grøvdal. “A dimensional-decomposition approach for stochastic scale-resolving simulations of turbulent reacting flows”. In: (2018).
[52] F. Grøvdal et al. “Three-dimensional linear eddy modeling of a turbulent lifted hydrogen jet flame in a vitiated co-flow”. In: *Flow, Turbulence and Combustion* 101 (2018), pp. 993–1007.
[53] F. Grøvdal et al. “A parametric study of LEM3D based on comparison with a turbulent lifted hydrogen jet flame in a vitiated co-flow”. In: *Combustion Science and Technology* (2019).
[54] T. Lackmann. *A representative interactive linear-eddy-model (RILEM) for simulating spray combustion*. Department of Combustion, Chalmers University of Technology, 2017.

[55] T. Lackmann, A.R. Kerstein, and M. Oevermann. *A representative interactive linear eddy model (RILEM) for non-premixed combustion.* Tech. rep. SAE Technical Paper, 2015.
[56] T. Lackmann, A.R. Kerstein, and M. Oevermann. *Comparison of a Representative Linear Eddy Model with a Representative Interactive Flamelet Model for Spray Combustion Processes.* Tech. rep. SAE Technical Paper, 2015.
[57] T. Lackmann et al. *Modeling n-dodecane spray combustion with a representative interactive linear eddy model.* Tech. rep. SAE Technical Paper, 2017.
[58] T. Lackmann, A.R. Kerstein, and M. Oevermann. "A representative linear eddy model for simulating spray combustion in engines (RILEM)". In: *Combustion and Flame* 193 (2018), pp. 1–15.
[59] T. Lackmann et al. "Investigation of turbulence–chemistry interactions in a heavy-duty diesel engine with a representative interactive linear eddy model". In: *International Journal of Engine Research* 21.8 (2020), pp. 1469–1479.
[60] O. Reynolds. "XXIX. An experimental investigation of the circumstances which determine whether the motion of water shall be direct or sinuous, and of the law of resistance in parallel channels". In: *Philosophical Transactions of the Royal society of London* 174 (1883), pp. 935–982.
[61] L.F. Richardson. *Weather prediction by numerical process.* University Press, 1922.
[62] A.N. Kolmogorov. "The local structure of turbulence in incompressible viscous fluid for very large Reynolds numbers". In: *Proceedings of the Royal Society of London. Series A: Mathematical and Physical Sciences* 434.1890 (1991), pp. 9–13.
[63] B. Cuenot and T. Poinsot. "Effects of curvature and unsteadiness in diffusion flames. Implications for turbulent diffusion combustion". In: *Symposium (International) on Combustion.* Vol. 25. 1. Elsevier. 1994, pp. 1383–1390.
[64] D. Thevenin et al. "Extinction processes during a non-premixed flame-vortex interaction". In: *Symposium (International) on Combustion.* Vol. 27. 1. Elsevier. 1998, pp. 719–726.
[65] P.H. Renard et al. "Dynamics of flame/vortex interactions". In: *Progress in energy and combustion science* 26.3 (2000), pp. 225–282.
[66] E.R. Van Driest. "Turbulent boundary layer in compressible fluids". In: *Journal of the Aeronautical Sciences* 18.3 (1951), pp. 145–160.
[67] E.A. Spiegel and G. Veronis. "On the Boussinesq approximation for a compressible fluid." In: *The Astrophysical Journal* 131 (1960), p. 442.
[68] L. Prandtl. "7. Bericht über Untersuchungen zur ausgebildeten Turbulenz". In: *ZAMM-Journal of Applied Mathematics and Mechanics/Zeitschrift für Angewandte Mathematik und Mechanik* 5.2 (1925), pp. 136–139.
[69] W.P. Jones and B.E. Launder. "The prediction of laminarization with a two-equation model of turbulence". In: *International journal of heat and mass transfer* 15.2 (1972), pp. 301–314.
[70] B.E. Launder and D.B. Spalding. "The numerical computation of turbulent flows". In: *Numerical prediction of flow, heat transfer, turbulence and combustion.* Elsevier, 1983, pp. 96–116.
[71] S.P. Burke and T.E.W. Schumann. "Diffusion flames". In: *Industrial and Engineering Chemistry* 20 (1928), pp. 998–1005.
[72] G. D'Errico, D. Ettorre, and T. Lucchini. "Comparison of Combustion and Pollutant Emission Models for DI Diesel Engines". In: *8th International Conference on Engines for Automobiles.* cit. on p. 11. Consiglio Nazionale delle Ricerche. 2007. DOI: `https://doi.org/10.4271/2007-24-0045`.
[73] N. Peters. "Laminar diffusion flamelet models in non-premixed turbulent combustion". In: *Progress in energy and combustion science* 10.3 (1984), pp. 319–339.

[74] H. Barths, C. Antoni, and N. Peters. “Three-dimensional simulation of pollutant formation in a DI Diesel engine using multiple interactive flamelets”. In: *SAE transactions* (1998), pp. 987–997.
[75] H. Barths et al. “Simulation of combustion in direct injection diesel engines using a eulerian particle flamelet model”. In: *Proceedings of the Combustion Institute* 28.1 (2000), pp. 1161–1168.
[76] R.W. Bilger. “Conditional moment closure for turbulent reacting flow”. In: *Physics of Fluids A: Fluid Dynamics* 5.2 (1993), pp. 436–444.
[77] J. Villermaux and J.C. Devillon. “Représentation de la coalescence et de la redispersion des domaines de ségrégation dans un fluide par un modèle d’interaction phénoménologique”. In: *Proceedings of the 2nd International symposium on chemical reaction engineering*. Vol. 26. Elsevier New York. 1972, pp. 1–13.
[78] R.L. Curl. “Dispersed phase mixing: I. Theory and effects in simple reactors”. In: *AIChE journal* 9.2 (1963), pp. 175–181.
[79] J. Janicka, W. Kolbe, and W. Kollmann. “Closure of the transport equation for the probability density function of turbulent scalar fields”. In: *Journal of Non-Equilibrium Thermodynamics* (1979).
[80] H. Chen, S. Chen, and R.H. Kraichnan. “Probability distribution of a stochastically advected scalar field”. In: *Physical Review Letters* 63.24 (1989), p. 2657.
[81] D. G. Goodwin et al. *Cantera: An Object-oriented Software Toolkit for Chemical Kinetics, Thermodynamics, and Transport Processes*. `https://www.cantera.org`. Version 1.8.0. 2021. DOI: `10.5281/zenodo.4527812`.
[82] A. C. Hindmarsh et al. “SUNDIALS: Suite of nonlinear and differential/algebraic equation solvers”. In: *ACM Transactions on Mathematical Software (TOMS)* 31.3 (2005), pp. 363–396.
[83] T.M. Smith and S. Menon. “One-dimensional simulations of freely propagating turbulent premixed flames”. In: *Combustion Science and Technology* 128.1-6 (1997), pp. 99–130.
[84] R.D. Reitz and F.V. Bracco. “Mechanism of atomization of a liquid jet”. In: *Physics of Fluids* 25.10 (1982), pp. 1730–1742.
[85] Carsten Baumgarten. *Mixture formation in internal combustion engines*. Springer Science & Business Media, 2006.
[86] R.D. Reitz and R. Diwakar. “Structure of high-pressure fuel sprays”. In: *SAE Transactions* (1987), pp. 492–509.
[87] S. von Kuensberg et al. “Modeling the effects of injector nozzle geometry on diesel sprays”. In: *SAE Transactions* (1999), pp. 1375–1388.
[88] A. Wierzba. “Deformation and breakup of liquid drops in a gas stream at nearly critical Weber numbers”. In: *Experiments in fluids* 9.1 (1990), pp. 59–64.
[89] Helmholtz. “XLIII. On discontinuous movements of fluids”. In: *The London, Edinburgh, and Dublin Philosophical Magazine and Journal of Science* 36.244 (1868), pp. 337–346.
[90] W. Thomson. “XLVI. Hydrokinetic solutions and observations”. In: *The London, Edinburgh, and Dublin Philosophical Magazine and Journal of Science* 42.281 (1871), pp. 362–377.
[91] G. I. Taylor. “The instability of liquid surfaces when accelerated in a direction perpendicular to their planes. I”. In: *Proceedings of the Royal Society of London. Series A. Mathematical and Physical Sciences* 201.1065 (1950), pp. 192–196.
[92] S.S. Hwang, Z. Liu, and R.D. Reitz. “Breakup mechanisms and drag coefficients of high-speed vaporizing liquid drops”. In: *Atomization and Sprays* 6.3 (1996).
[93] Suresh Menon. “Multi-scale modeling for LES of engineering designs of large-scale combustors”. In: *42nd AIAA aerospace sciences meeting and exhibit*. 2004, p. 157.

[94] Charles David Pierce. *Progress-variable approach for large-eddy simulation of turbulent combustion*. stanford university, 2001.
[95] R.W. Bilger. "The structure of diffusion flames". In: *Combustion Science and Technology* 13.1-6 (1976), pp. 155–170.
[96] C. D. Pierce and P. Moin. "Progress-variable approach for large-eddy simulation of non-premixed turbulent combustion". In: *Journal of Fluid Mechanics* 504 (2004), pp. 73–97.
[97] N. Doubiani, A. R. Kerstein, and M. Oevermann. "A pressure-coupled Representative Interactive Linear Eddy Model (RILEM) for engine simulations". In: *Fuel* 355 (2024), p. 129423.